Physical Layer Aspects of Uncrewed Aerial Vehicle (UAV)-to-Ground Communications

by

Remon Polus, B.Sc., M.Sc.

A thesis submitted to the University of Ottawa in partial fulfillment of the requirements
for the degree of
Doctorate in Philosophy
in
Electrical and Computer Engineering

School of Electrical Engineering and Computer Science
Faculty of Engineering
University of Ottawa

Examining Committee Membership

The following served on the Examining Committee for this thesis. The decision of the Examining Committee is by majority vote.

External Member: Jean-Yves Chouinard
Professor, Department of Electrical and Computer Engineering
Université Laval

Carleton Member: Halim Yanikomeroglu
Chancellor's Professor, Department of Systems and Computer Engineering
Carleton Univeristy

Internal Members: Melike Erol-Kantarci
Professor, School of Electrical Engineering & Computer Science
University of Ottawa

François Chan
Adjunct Professor, School of Electrical Engineering & Computer Science
University of Ottawa

Supervisor: Claude Denis D'Amours
Professor, School of Electrical Engineering & Computer Science
University of Ottawa

Declaration of Authorship

I hereby certify that this thesis is entirely my own original work except where otherwise indicated. I am aware of the University of Ottawa regulations concerning plagiarism, including those regarding consequent disciplinary actions. Any use of the works of any other author, in any form, is properly acknowledged at their point of use.

Abstract

With the projected capabilities of 6G networks aiming to deliver a peak data rate of 1 Tbps and extend connectivity to millions of devices within square kilometers by 2030, the inclusion of aerial connectivity emerges as a pivotal trend and enabling technology within 6G networking. This integration of non-terrestrial networks (NTN) brings forth new airborne vehicles complementing existing ground networks. Among these vehicles, uncrewed aerial vehicles (UAVs) have garnered considerable attention from both academia and industry due to their affordability and versatility across diverse scenarios and applications.

Given the critical need for precise characterization of the UAV-to-ground channels, this thesis focuses on investigating the physical layer aspects of the UAV-to-ground channels. These novel fading channel models take into account multipath as well as shadowing. This dissertation studies the various capacities of UAV-to-ground channels. Specifically, it evaluates the effective capacity and ergodic capacity under various power adaptation techniques. These capacity metrics serve as fundamental measures, allowing an assessment of the transmission's achievable rates. Moreover, this dissertation analyzes the physical layer security metrics of these novel channel models, which offers insights into the security robustness of the UAV-to-ground communication system.

Furthermore, this dissertation examines system reliability by deriving the error probability in the presence of phase noise. Introducing phase noise into the assessment of receiver performance makes the analysis more practical and enhances the potential for designing an improved system. Moreover, the dissertation extends its evaluation by considering multiple antenna receivers, specifically selection combining (SC) and maximal ratio combining (MRC). These techniques aim to alleviate channel fading effects and enhance diversity for improved system performance. The analysis encompasses key metrics such as outage probability, average channel capacity, outage capacity, average bit error rate (ABER), and average symbol error rate (ASER). By assessing these metrics for different receiver configurations, this study comprehensively examines the efficacy of SC and MRC in mitigating channel fading effects, thus enhancing system reliability and achieving superior performance under various channel conditions.

Additionally, this thesis offers a thorough examination of the characteristics and performance metrics of interference-limited wireless communication systems functioning across UAV-to-ground fading channels. Moreover, it introduces cascaded shadowed UAV-to-

ground fading channels and conducts a rigorous statistical analysis to unveil their intricate dynamics. Furthermore, it presents an analytical framework for assessing energy detection-based spectrum sensing receivers operating in these challenging environments. Through mathematical derivations and simulations, this work provides valuable insights and methodologies for enhancing the reliability and performance of wireless communication systems in UAV-to-ground scenarios. The expressions derived in this thesis are then verified by comparing them against the results obtained through Monte Carlo simulations.

Acknowledgements

This thesis represents the culmination of years of dedication and effort. I would like to express my heartfelt gratitude to those who have played a pivotal role in the completion of this work.

First and foremost, I am profoundly grateful to my advisor, Prof. Claude D'Amours, for granting me the remarkable opportunity to transition from my cherished hometown of Alexandria, known as the intellectual capital of the Ancient World, to Ottawa, the heart of Canada's capital and aptly named "Silicon Valley North." His unwavering support, mentorship, and belief in my abilities have been instrumental in advancing both my research and career. Our collaboration has resulted in the co-authorship of numerous papers published in prestigious IEEE journals, as well as several conference contributions. I am also deeply honored to have received the 2024 IEEE Vehicular Technology Society Student Scholarship Award, an achievement made possible through our scientific partnership.

I would also like to extend my sincere appreciation to Profs. Jean-Yves Chouinard, Halim Yanikomeroglu, François Chan, and Melike Erol-Kantarci for their invaluable time and effort in serving on my defense committee. Their insightful feedback, thoughtful reviews, and encouraging words have significantly enhanced the quality of this thesis.

Finally, my deepest thanks go to my father, sister, brother-in law, and nephews, whose unwavering support and encouragement have been my foundation throughout this journey. Without their love and belief in me, none of this would have been possible.

Table of Contents

List of Tables

List of Figures

Abbreviations

1G	First-generation
2G	Second-generation
3G	Third-generation
3GPP	3Rd Generation Partnership Project
5G	Fifth-generation
6G	Sixth-generation
AA	Air–to–air
ABER	Average Bit Error Rate
AG	Air–to–ground
AI	Artificial Intelligence
ASC	Average Secrecy Capacity
ASER	Average Symbol Error Rate
AWGN	Additive White Gaussian Noise
BFSK	Binary Frequency Shift Keying
BPF	Band-pass Filter
BPSK	Binary Phase Shift Keying
CDF	Cumulative Distribution Function
CDMA	Code-Division Multiple Access
CIFR	Channel Inversion With Fixed Rate
CNPC	Command And Non-Payload Communication
CR	Cognitive Radio
DS	Double-shadowing
ED	Energy Detection
EGC	Equal-gain Combining
eMBB	Enhanced Mobile Broadband

FAA	Federal Aviation Administration
GEO	Geostationary Earth Orbit
GSM	Global Systems For Mobile Communications
HAP	High-altitude Platform
HRLLC	Hyper Reliable Low Latency Communication
IMT	International Mobile Telecommunications
IoT	Internet Of Things
ITU	International Telecommunication Union
LAP	Low-altitude Platform
LEO	Low Earth Orbit
LoS	Line-of-sight
LTE	Long-Term Evolution
MEO	Medium Earth Orbit
MGF	Moment-generating Function
MIMO	Multiple-input Multiple-output
ML	Machine Learning
mMTC	Massive Machine-type Communications
MPSK	M-Ary Phase Shift Keying
MRC	Maximal-ratio Combining
NOMA	Non-orthogonal Multiple Access
NR	New Radio
NTN	Non-terrestrial Networks
OFDM	Orthogonal Frequency Division Multiplexing
OPRA	Optimal Power And Rate Adaptation
ORA	Optimal Rate Adaptation With Fixed Power
PDF	Probability Density Function
QAM	Quadrature Amplitude Modulation
QoS	Quality Of Service
QPSK	Quadrature Phase Shift Keying
RIS	Reconfigurable Intelligent Surfaces
ROC	Receiver Operating Characteristic
Rx	Receiver
SC	Selection Combining
SIR	Signal-to-interference Ratio

SISO	Single-input Single-output
SN	Sensing Node
SNR	Signal-to-noise Ratio
SOP	Secrecy Outage Probability
SPSC	Strictly Positive Secrecy Capacity
SS	Single-shadowing
SWIPT	Simultaneous Wireless Information And Power Transfer
TIFR	Truncated Channel Inversion With Fixed Rate
Tx	Transmitter
UAV	Uncrewed Aerial Vehicle
UMTS	Universal Mobile Telecommunications Service
URLLC	Ultra-reliable Low-latency Communications
VLC	Visible Light Communication

List of Symbols

R	Average SIR value
ω	Average signal power
P_{be}	Average bit error rate
P_{se}	Average symbol error rate
$\mathcal{AF}$	Amount of Fading
$\mathbb{B}$	Bandwidth
erfc(.)	Complementary error function
$\mathcal{CN}(\mathbf{0}, N_o)$	Complex Gaussian distribution of a random variable, having independent Gaussian distributed real and imaginary parts
i	Complex number = $\sqrt{-1}$
${}_1F_1(.;.;.)$	Confluent hypergeometric function of the first kind
$F_X(.)$	Cumulative distribution function of a random variable X
Λ	Energy detection threshold
E_b	Energy per bit
C_{E}	Effective capacity
C_{ER}	Ergodic capacity
Ei(.)	Exponential integral function
$\mathbb{E}\{.\}$	Expectation
$H_{p,q}^{m,n}\left(.\middle\vert.\right)$	Fox H-function
$\Gamma(.)$	Gamma function
$Q_u(.,.)$	Generalized Marcum Q-function
L	Number of sensing nodes

$\gamma(.,.)$	Lower incomplete Gamma function
$\mathcal{M}_X(.)$	Moment-generating function of a random variable X
$G_{p,q}^{m,n}(.\|.)$	Meijer G-function
$I_\nu(.)$	Modified Bessel function of first kind with order ν
M	Modulation Order
C_{out}	Outage capacity
P_{out}	Outage probability
P_{sec}	Secrecy outage probability
$f_X(.)$	Probability density function of a random variable X
P_{SPSC}	Probability of strictly positive secrecy capacity (SPSC)
$\mathcal{P}_d$	Probability of detection
$\mathcal{P}_f$	Probability of false alarm
$\mathcal{P}_m$	Probability of missed detection
$\mathbb{P}(.)$	Probability
$Q(.)$	Q-Function
C_{S}	Secrecy capacity
$\mathbb{T}$	Time interval
$\Gamma(.,.)$	Upper incomplete gamma function
$\overline{P}$	Average power
$\overline{\gamma}$	Average received SNR
n	AWGN variable
T	Block length
θ	Buffer occupancy decay rate
Φ	Capacity threshold
h	Channel fading coefficient
P_D	Desired signal power
d	Distance
P_F	Interfering signal power
ρ	Loop SNR of the phase locked loop
N_r	Number of receive antennas
σ_N^2	AWGN variance
η	Path loss exponent
σ_p^2	Phase noise variance
ϕ	Phase error variable

P_t	Transmit power
y	Received signal
R_s	Threshold secrecy rate
α	Shadowing parameter
m	Multipath parameter
λ	SIR threshold
γ_c	SNR cutoff value
γ_m	Maximum SNR value
γ_o	Optimal SNR value
γ	Signal-to-noise ratio
γ_{th}	SNR threshold value
x	Transmitted signal

Chapter 1

Introduction

Over the past fifty years, cellular communication systems have undergone significant evolution, progressing from the initial first-generation (1G) analog system to the upcoming sixth-generation (6G) technology. The 1G system, which emerged in the 1980s, primarily facilitated voice services through analog transmission. Following this, in 1992, the advent of the Global Systems for Mobile Communications (GSM) marked the transition to the more advanced second-generation (2G) system. Notably, 2G not only facilitated voice signals but also introduced digital data communication capabilities, including short message services, operating at a maximum rate of 64 kbps [1]. In the 2000s, the emergence of third-generation (3G) networks aimed to meet the burgeoning demands for internet browsing and multifaceted data services, like video calls and multimedia messaging. Several 3G standards, such as Code-Division Multiple Access (CDMA)-200 and Universal Mobile Telecommunications Service (UMTS), notably improved transmission rates, offering speeds of up to 2 Mbps [2].

In 2009, the Long-Term Evolution (LTE) technology made its debut as the 4G system, revolutionizing mobile communication with a peak rate of 150 Mbps. This marked a significant milestone in supporting mobile broadband applications, enabling services like voice-over-internet protocol and immersive video gaming experiences [3]. Notably, LTE brought forth groundbreaking technologies at the physical layer, including multiple-input multiple-output (MIMO) and orthogonal frequency division multiplexing (OFDM). These advancements played a pivotal role in achieving higher data rates and enhancing system performance. Additionally, LTE continued to utilize the traditional microwave band below 6 GHz for its operations.

During the early 2010s, both academia and industry embarked on defining the potential of fifth-generation (5G) technology. According to the International Telecommunication Union (ITU), 5G is designed to support three generic categories of services: massive machine-type communications (mMTC), ultra-reliable low-latency communications (URLLC), and enhanced mobile broadband (eMBB) [4]. These categories lay the groundwork for transformative services such as machine-to-machine, device-to-device, and device-to-everything communications, fostering the development of the Internet of Things (IoT) and the Internet of Vehicles [5]. This evolution brought about an unprecedented scale, adding millions of new devices to wireless networks and expanding mobile communication services beyond human interaction to include interactions between various devices and objects. Table 1.1 summarizes the requirements for 5G systems. To meet the demands of these diverse service categories, numerous key enabling technologies have been proposed for the physical layer. These include massive MIMO, full-duplex communication, and non-orthogonal multiple access (NOMA) [6]. Furthermore, the millimeter-wave band (30-300 GHz) has emerged as a candidate band for 5G systems, envisioned to achieve significantly higher data rates.

	4G	5G	6G
Peak Data Rate	150 Mbps	20 Gbps	>= 1 Tbps
Experienced Data Rate	10 Mbps	0.1 Gbps	1 Gbps
Latency	10 ms	1 ms	$10 - 100$ μs
Area Traffic Capacity (Mb/s/m^2)	0.1	10	10^3
Mobility (Km/h)	350	500	>=1000
Number of Connected Devices (Devices/km^2)	10^3	10^6	10^7

Table 1.1: Requirements of 4G vs. 5G vs. 6G.

In 2019, the 3rd Generation Partnership Project (3GPP), a consortium responsible for standardizing cellular networks in collaboration with telecommunication standards organizations and industry companies, completed the standardization of 5G-New Radio (NR) in its Release-15 [7]. Following this milestone, commercial deployment of 5G-NR commenced in numerous countries worldwide, marking a pivotal leap in global connectivity. To enhance 5G's performance and accommodate evolving use cases, 3GPP launched subsequent releases. In 2020, Release-16 was introduced, followed by Release-17 in 2022, aiming

to introduce additional features to the 5G framework and expand its user scenarios [8]. Presently, 3GPP is actively engaged in ongoing studies for 5G-Advanced as part of its Release-18 and subsequent developments [9].

1.1 6G Networks

While 3GPP continues its work on 5G and 5G-Advanced, both academia and industry have already started to investigate the fundamental characteristics of 6G networks. Projections suggest that by 2030, society will undergo extensive digitization, characterized by intelligence-driven operations and a globally data-centric environment enabled by instantaneous and limitless wireless connectivity [10]. The advent of 6G is poised to transform communication paradigms, transitioning from "*connected things*" to "*connected intelligence*." International Mobile Telecommunications (IMT) has already outlined recommendations for its 2030 vision, commonly referred to as IMT-2030, that entail the expansion of three key 5G pillars [11]:

1. URLLC in 5G evolves into Hyper Reliable Low Latency Communication (HRLLC) in 6G.
2. eMBB in 5G transforms into immersive communication in 6G.
3. mMTC in 5G advances into massive communication in 6G.

This next-generation network is anticipated to open the door to a wide array of unprecedented applications, encompassing realms like self-driving vehicles, the Internet of Intelligent Things, virtual reality, human-body interfaces, and holographic communications [12]. The requirements for 6G systems are highlighted in Table 1.1 [13,14]. To fulfill these requirements, numerous innovative physical layer technologies have been proposed for 6G. These include THz communications (0.1–10-THz band), non-terrestrial networks (NTN), reconfigurable intelligent surfaces (RIS), visible light communication (VLC), machine learning (ML), and artificial intelligence (AI)-enabled wireless networks [15].

1.1.1 Aerial Communications

In order to extend wireless coverage to remote and underprivileged areas like rural regions, where the cost of establishing terrestrial networks proves financially unfavorable,

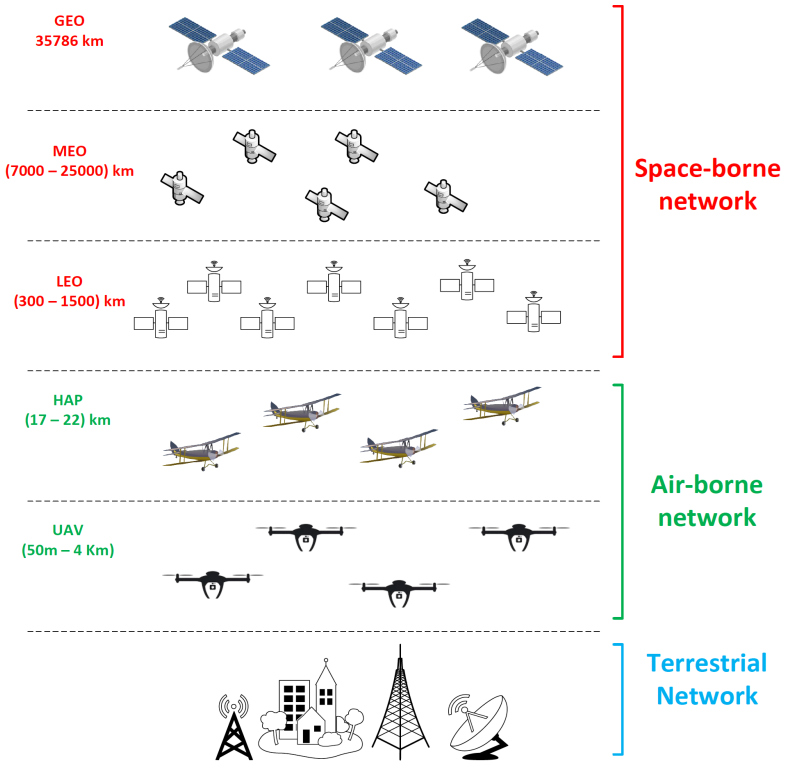

Figure 1.1: An illustration of non-terrestrial networks.

NTN emerges as a promising solution. NTN offers reliable and boundless aerial connectivity, making it an essential component projected for integration within 6G networks and expected to play a pivotal role in providing global coverage for advanced 5G and 6G networks. As per the definition provided by 3GPP, NTN encompasses "*networks or segments of networks utilizing airborne or space-borne vehicles to host transmission equipment relay nodes or base stations*" [16]. As illustrated in Figure 1.1, NTN platforms can be classified into two main categories:

1. **Space-borne vehicles**

   Space-borne vehicles are satellite stations that are categorized based on their altitudes as:

   (a) *Geostationary Earth orbit (GEO)* satellites orbit at an altitude of 35786 km in a circular and equatorial path around Earth.

   (b) *Medium Earth orbit (MEO)* satellites operate within altitudes ranging from 7000 to 25000 km, following a circular orbit around Earth.

(c) *Low Earth orbit (LEO)* satellites, positioned at altitudes between 300 and 1500 km, also follow a circular path around Earth.

Recent deployed commercial systems like Kuiper, Starlink, and OneWeb capitalize on the advantages of the LEO constellation for providing wireless connectivity to subscribers due to its lower orbit location, resulting in shorter round-trip times and relatively lower deployment costs [17]. However, while space-borne vehicles, particularly those in higher orbits, boast a much larger coverage area compared to airborne systems, they also incur higher deployment costs and exhibit larger propagation delays.

2. **Airborne vehicles**

Airborne vehicles, which are located between terrestrial networks and satellite stations, have the benefit of being affordable, flexible, and easy to deploy. They can be classified into two main categories:

(a) *High-altitude platform (HAP)*: Operating at an altitude of approximately 17-22 km in the stratosphere layer, HAP vehicles are quasi-stationary.

(b) *Low-altitude platform (LAP)*: Ranging from 50 meters up to 4 kilometers in altitude, LAP includes aerial vehicles like a UAV, commonly known as a drone. UAVs are further categorized based on their design structure [18].

i. Fixed-wing UAVs: They are high-speed and have a heavy payload but need to move forward to remain aloft.

ii. Rotary-wing UAVs, such as quadcopters, can hover or stay stationary in the air, but they are low-speed and have a lower payload.

Historically, UAVs were utilized for military applications, predominantly for surveillance purposes. However, their scope has expanded significantly into various civilian sectors such as package delivery, sensing operations, and cellular communication due to their cost-effectiveness, high maneuverability, and adaptability [19,20]. Recent advancements in UAV technology have spurred innovative projects in the market. For instance, Facebook initiated its 'Aquila' project in 2016, aiming to provide internet access to remote areas using solar-powered drones. Additionally, projects like Amazon Prime Air and Google's Wing focus on packet delivery via UAVs [21]. By 2030, the annual expenditure on UAVs is projected to reach approximately USD 102.4 billion, reflecting a compound annual growth

rate of 19.6%. This significant increase is set to surpass the USD 19.78 billion spent in 2020 [22].

From the perspective of telecommunications, UAVs can be integrated into the cellular network in three main ways [20]:

1. Cellular-connected UAV: In this technology, a UAV acts as new aerial user equipment in parallel with terrestrial user terminals on the ground.

2. UAV-assisted wireless communications: In this technology, a UAV acts as a small flying aerial base station, access point, or relay node to assist wireless terrestrial networks.

3. Integrated sensing and communications: In this technology, wireless infrastructure and spectrum resources are utilized in a shared manner to offer both sensing and communication services [23].

To ensure both public safety and privacy protection, various countries worldwide have initiated regulations governing UAV systems. For instance, Transport Canada mandates the registration of drones weighing between 250 g and 25 kg [24]. Similarly, in the United States, the Federal Aviation Administration (FAA) serves as the regulatory authority overseeing UAV operations within American airspace, setting guidelines for drone speed, altitude, and operational range [25].

Since Release-15, UAV communication has been one of the active areas of the 3GPP standardization body. Several UAV-enabled applications and use cases are included in 3GPP TR 22.829, issued in 2019, along with a description of the requisite communications and networking performance enhancements. The work items for UAV communications in Rel-17 in 2020 concentrated on two key areas: the application architecture to allow effective UAV operations (TR 23.755) and the network infrastructure and protocols to provide connection, identification, and tracking of UAVs (TR 23.754). [26]. Table 1.2 provides a summary of 3GPP standardization efforts dedicated to UAV communications for both 5G and beyond systems.

Table 1.2: 3GPP standardization efforts for UAV communications.

Release	Study Item	Title and Discription
Rel-15	36.777 [27]	**Enhanced LTE support for aerial vehicles** Specified performance criteria for communication between several UAVs in 5G networks.
Rel-16	22.125 [28]	**Unmanned Aerial System (UAS) support in 3GPP** Defined the requirements for delivering UAV services via 3GPP networks.
Rel-16	22.825 [29]	**Remote Identification of Unmanned Aerial Systems** Discussed the mechanisms for remote identification of UAVs.
Rel-16	22.829 [30]	**Enhancement for Unmaned Aerial Vehicles (UAVs)** Discussed a range of applications and scenarios empowered by UAVs. Additionally, it highlights the essential enhancements required for communication and networking performance.
Rel-17	23.754 [31]	**Supporting Unmanned Aerial Systems (UAS) connectivity, Identification and tracking** Focused on the network infrastructure and procedures to support the connectivity, identification, and tracking of UAVs.
Rel-17	23.755 [32]	**Application layer support for Unmanned Aerial Systems** Studied application architecture to support efficient UAV operations.

1.2 Motivation of the Thesis

The study and standardization of UAV communications are still in their early phases. To support the numerous use cases in practical systems, it is vital to research the performance specifications for UAVs and analyze the technology and protocol solutions. As a result, this has brought about several new research challenges and opportunities related to the physical layer, like channel modeling.

Traditionally, the wireless communication link between the UAV in the sky and user equipment on the ground is described as a line-of-sight (LoS) channel, using the well-known Rician distribution to model the received signal-to-noise ratio (SNR) fading [33]. However, large obstacles are not avoidable, especially in urban areas and cities, which results in shadowing the transmitted signal. Thus, the LoS case is not always guaranteed. The shadowing can be established at both the transmitter and receiver regions, referred to as the double-shadowing (DS) case, or it can be allocated at one of them, referred to as the single-shadowing (SS) case. The shadowing effect can be mathematically modeled using the inverse gamma distribution, whereas the multipath fading of this channel follows the Nakagami-m distribution. In [34, 35], the authors proposed new statistical fading models for the wireless medium between a UAV in the sky and equipment on the ground. The new models were supported by empirical data gathered during a UAV-to-ground measurement experiment.

Until the start of our research, few research papers considered these empirically fit fading models. In [34, 35], the authors analyzed the system performance for the UAV-to-ground channels with a single receive antenna using the PDF and cumulative distribution function (CDF) of the received SNR. Moreover, the authors in [36] limited their focus to the average symbol error rate (ASER) only. However, these studies are not adequate for different scenarios related to the beyond 5G and 6G systems. For instance, the authors in [37] suggested that practical UAV channel modeling should be considered when exploiting the physical layer properties of the channel. Multiple antennas and RIS are some of the open directions proposed in [38]. Studying UAV-to-ground communications in practical, up-to-date systems can be useful to communication system designers working on these new fading channels.

1.3 Contribution of the Thesis

This thesis aims to bridge existing research gaps concerning innovative UAV-to-ground channel models. The research presented endeavors to contribute novel insights to the current literature by focusing on the following key areas:

1. Derivation of closed-form expressions for the average bit error rate (ABER) for binary phase shift keying (BPSK) and quadrature phase shift keying (QPSK) under imperfect phase recovery, modeled by Tikhonov or Gaussian distributions.

2. Closed-form expressions for the ASER of M-ary phase shift keying (MPSK) under the Tikhonov-distributed phase error.

3. Exact closed-form expressions for the channel capacity of UAV-to-ground fading channels under different power adaptation strategies, including optimal rate adaptation with fixed power (ORA), optimal power and rate adaptation (OPRA), channel inversion with fixed rate (CIFR), and truncated channel inversion with fixed rate (TIFR).

4. Analytical expressions for the effective capacity of UAV-to-ground fading channels.

5. Examining physical layer security metrics, such as the average secrecy capacity, the secrecy outage probability, and the probability of strictly positive secrecy capacity, in UAV-to-ground communications with shadowing.

6. Deriving theoretical expressions for the ABER, ASER, ergodic capacity, and outage probability of a receiver using maximal-ratio combining (MRC) operating in independent UAV-to-ground channels based on the moment-generating function (MGF).

7. Evaluation of the performance metrics, including ABER, outage capacity, outage probability, and average channel capacity for a selection combining (SC) receiver operating in UAV-to-ground channels.

8. Deriving closed-form expressions of the outage probability for an interference-limited system operating over UAV-to-ground channels.

9. Examining the performance of cascaded shadowed UAV-to-ground fading channels by deriving key metrics such as outage probability, average channel capacity, and ABER.

10. Deriving closed-form expressions of average probability of detection of energy-detection based spectrum sensing operating over UAV-to-ground channels.

1.4 Organization of the Thesis

Beyond this chapter, the organization of this thesis is as follows:

- **Chapter 2**: Some preliminary background knowledge is presented in this chapter. In particular, a detailed review of the UAV-to-ground channel models is provided.

- **Chapter 3**: In this chapter, we provide the mathematical framework for UAV-to-ground communications with imperfect phase recovery over these novel channel models.

- **Chapter 4**: This chapter presents an in-depth analysis of the UAV-to-ground channel's capacity under diverse power adaptation schemes. The study extends to evaluating the channel's effective capacity and delves into assessing the physical layer security of UAV-to-ground communication.

- **Chapter 5**: This chapter focuses on receiver diversity to mitigate multipath fading. Performance analysis of MRC and SC receivers over shadowed UAV-to-ground channels is presented.

- **Chapter 6**: In this chapter, novel mathematical expressions are derived to describe the PDF, CDF, and MGF of the signal-to-interference ratio (SIR) for an interference-limited system operating over UAV-to-ground channels.

- **Chapter 7**: In this chapter, cascaded shadowed UAV-to-ground fading channels are mathematically characterized in order to analyze the reliability of wireless communication systems operating over such channels.

- **Chapter 8**: This chapter analyzes the performance of energy-detection based spectrum sensing operating over UAV-to-ground channels.

- **Chapter 9**: Finally, conclusions and future research directions are presented in this chapter.

- **Appendix A**: A mathematical review of the Meijer G-function is presented in this appendix, which can be considered a tutorial for those readers who are not familiar with the Meijer G-function.

- Mathematical derivations of some equations can be found in **Appendices B** and **C**.

- **Appendix D** provides a comprehensive list of publications that are pertinent to this thesis.

Chapter 2

Background and Literature Review

This chapter aims to provide an overview of several topics related to the operation of a UAV from a telecommunications perspective. Firstly, we start to explain the different types of UAV signals in Section 2.1. Then, UAV-to-ground channel models are presented in Section 2.2.

2.1 UAV Signals

Generally, communications signals related to the operation of the UAV can be categorized as [39]

1. Command and Non-Payload Communication (CNPC): CNPC stands for the bidirectional communication between unmanned aircraft and ground control station (or remote pilot) in order to ensure secure, dependable, and efficient flight operations. Examples of typical CNPC messages encompass:

    - Transmitting telemetry data (such as flight altitude and speed) from the UAV to the ground.
    - Providing real-time remote command and control for UAVs that lack full autonomy, and regular updates on flight commands.
    - Sharing navigation assistance and information linked to collision avoidance.
    - Relaying details pertinent to air traffic control.

2. Payload signals: Payload communication pertains to the transmission of all mission-related information between a UAV and ground users. This includes real-time video, imagery, and data transmission.

Commonly, two popular frequency bands, specifically 2.4 GHz and 5.8 GHz, are employed by commercial UAVs for their CNPC operations while in flight. However, the aviation authorities generally do not favour these frequency bands due to concerns about congestion and susceptibility to jamming [40, 41]. In the United States, there is a potential plan to allocate portions of the L-band (0.9 GHz - 1.2 GHz) and C-band (5.03 GHz - 5.091 GHz) for CNPC purposes. For data signals, the unlicensed band is in use for this purpose. However, as is typical in spectrum allocation, the utilization of these frequency bands is still undergoing negotiation and discussion [42].

2.2 UAV-to-Ground Channels

One of the significant challenges lies in developing accurate propagation models that accurately represent different environments and situations in which UAVs operate. This is crucial to meet the growing need for high-speed data transmission in evolving UAV applications. Usually, mathematical models of wireless channels can be categorized into two categories:

1. Large-scale fading, also known as path loss or attenuation, is a fundamental phenomenon in wireless communication and signal propagation. It refers to the attenuation or weakening of an electromagnetic signal as it travels over a long distance or through various obstacles in a wireless communication environment. This attenuation is primarily due to the geometric spreading and absorption of the signal's energy by the surrounding environment.

   Large-scale fading models are useful for system engineers when calculating essential factors in a communication system's budget, such as the necessary transmitter power, attainable communication range, and receiver sensitivity. A summary of several path-loss models that characterize the channel between a UAV and receiver on the ground can be found in [43].

2. Small-scale fading, also known as multipath fading, is a phenomenon in wireless communication where the received signal experiences rapid variations in amplitude and phase due to the constructive and destructive interference of multiple signal paths that take different routes between the transmitter and the receiver. Small-scale fading is caused by the reflections, diffractions, and scattering of the transmitted signal by objects and obstacles in the propagation environment.

   These small-scale fading models aid engineers in devising strategies to mitigate fading, including techniques like diversity transmission/reception, forward error correction coding, interleaving, and equalization.

Additionally, UAV channel propagation can be classified into two main categories:

1. Air–to–air (AA) Channel: The propagation channel between aerial vehicles is a crucial factor in inter-UAV communications and can be utilized in various applications like aerial wireless sensor networks, networks involving multiple UAVs, or UAV swarms [44].

2. Air–to–ground (AG) Channel: The propagation channel between aerial vehicles in the sky and a ground node can find application in diverse scenarios such as communication relay, remote surveillance, transport of goods, and providing wireless connectivity in the case of a disaster [40].

The AG channel has unique features that set it apart from other extensively researched land-based communication channels, such as the urban channel. One key advantage is its high probability of LoS signal propagation, offering benefits like decreased power needs for transmission. However, this LoS may not occur in all scenarios. Moreover, shadowing might arise from various sources, including obstacles on the surface like buildings, terrain, or trees, and even from the aircraft itself during its flight maneuvers [44]. For UAVs, airframe shadowing, which occurs when the airframe obstructs the signal path, can significantly affect communication performance. Additionally, the UAV's constant maneuverability and mobility can introduce multipath effects, further impacting the signal quality [45]. This has motivated the authors of [34, 35] to develop two new statistical models that encounter both small-scale fading and shadowing. These novel distributions closely align with the actual data collected from the AG measurement campaign, which results in validating these models. Details of the empirical measurements can be found in [46].

This thesis mainly focuses on the composite models of the AG channel, which take into account multipath as well as shadowing. Until the start of this thesis project, these novel channel models were investigated under a single-input single-output (SISO) channel using BPSK and quadrature amplitude modulation (QAM) only. Table 2.1 reveals an oversight in previous works on the UAV-to-ground fading channels, where none accounted for the impact of imperfect phase recovery at the receiver (Rx). Additionally, prior research has not examined the capacities of these novel models, like effective capacity, ergodic capacity under various power adaptation schemes, and physical layer security. The analysis of diversity receivers in terms of ASER was solely addressed in [47]. This thesis attempts to address and bridge these specific gaps in current knowledge.

Table 2.1: Comparing our contributions to the previous literature work.

Parameters	**Previous work**	**This Work**
Additive white Gaussian noise (AWGN)	[34]	✓
Phase Noise		✓
Non-Coherent Modulations	[36]	
ASER (M-QAM modulations)	[36]	
Power Adaptation		✓
Effective Capacity		✓
Physical Layer Security		✓
MRC Diversity	[47] ASER only	✓
SC Diversity	[47] ASER only	✓
Equal-gain combining (EGC) Diversity	[47] ASER only	
Energy-detection based Spectrum Sensing		✓

In subsection 2.2.1, we present a mathematical overview of the statistical fading models of UAV-to-ground communications, which were recently proposed in [34,35]. Subsequently, a performance analysis of a communication system operating in these novel channels and numerical results are presented in subsections 2.2.2 and 2.2.3, respectively.

2.2.1 Channel Models

We begin by explaining the symbols that will be utilized throughout this subsection. The notations $f_X(.)$, $F_X(.)$, and $\mathcal{M}_X(.)$ denote the PDF, CDF, and MGF of a random variable X, respectively.

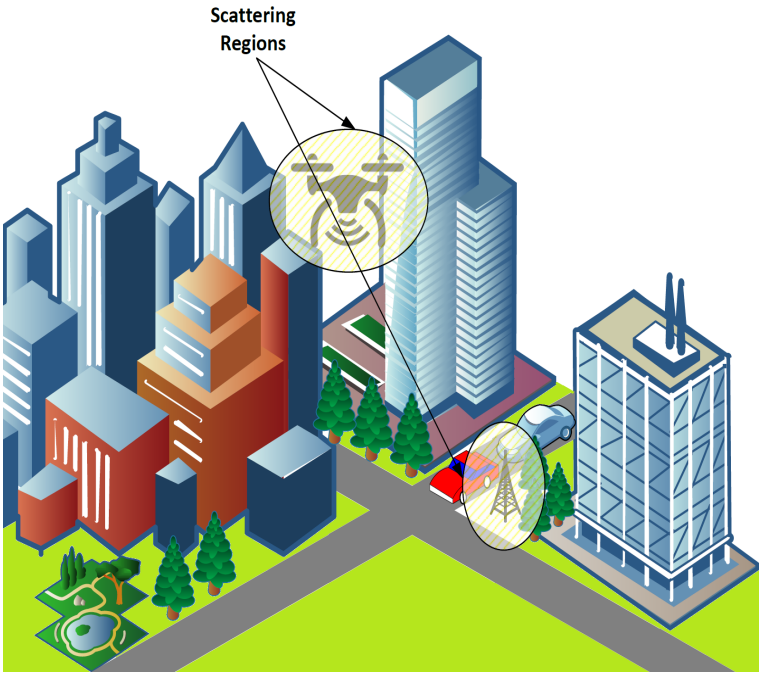

Figure 2.1: UAV-to-ground communication DS scenario.

2.2.1.1 Double-Shadowing (DS) Communication Scenario

The transmitter (Tx) is located in a UAV, and the Rx is located on the ground. Both the Tx and the Rx are separated by a large distance d, as illustrated in Figure 2.1. The received signal, y, at the Rx, can be written as

$$y = hx + n, \tag{2.1}$$

where x is the transmitted signal, h is the fading channel coefficient, and n represents the AWGN with $\mathcal{CN}(\mathbf{0}, N_o)$ distribution. The instantaneous output SNR, γ, at the Rx node is given by [36]

$$\gamma = \frac{P_t d^{-\eta} |h|^2}{\sigma_N^2}, \tag{2.2}$$

where P_t denotes the transmit power, η is the path loss exponent, and σ_N^2 is noise variance. In the DS scenario, there are double scattering regions both at the UAV and the ground node. The received SNR can be modeled as [34]

$$\gamma = N_1^2 I_1 N_2^2 I_2, \tag{2.3}$$

where

- $N_j - j \in \{1,2\}-$ represents the multipath fading coefficient, which follows the Nakagami-m distribution, whose PDF can be written as [48]

$$f_{N_j^2}(x) = \frac{{m_j}^{m_j} x^{m_j-1}}{{\Omega_j}^{m_j}\Gamma(m_j)} e^{-\frac{m_j x}{\Omega_j}}, \tag{2.4}$$

  where the distribution's shaping parameter m_j is the fading severity parameter, Ω_j is the scale parameter, and $\Gamma(.)$ is the gamma function. Nakagami-m distribution is more general than the Rician distribution to model LoS propagation. The m parameter can be converted to the Rician K parameter, as shown in [49].

- I_j represents the shadowing effect of the channel, modeled by the inverse-gamma distribution, whose PDF can be written as [50]

$$f_{I_j}(x) = \frac{{\overline{\gamma}_j}^{\alpha_j}}{x^{\alpha_j+1}\Gamma(\alpha_j)} e^{-\frac{\overline{\gamma}_j}{x}}, \tag{2.5}$$

  where the shaping parameter of the distribution $\alpha_j > 1$ represents the severity of the shadowing and $\overline{\gamma}_j$ denotes the scaling parameter. The reason behind selecting this statistical model is that there is an agreement between the inverse-gamma and lognormal distributions remains strong, even when considering larger standard deviations. The lognormal model is able to mathematically model the effect of shadowing, but it has limitations while forming a closed-form expression for a composite PDF that encompasses both multipath and shadowing [51].

1. **Probability Density Function (PDF):**

   The PDF of the received SNR, γ, can be expressed as [34]

$$f_\gamma(\gamma) = \gamma^{-1}\mathbb{S}_{DS} G_{2,2}^{2,2}\left(\frac{m_1 m_2}{\overline{\gamma}}\gamma \middle| \begin{matrix} 1-\alpha_2, 1-\alpha_1 \\ m_1, m_2 \end{matrix}\right), \tag{2.6}$$

   where

$$\mathbb{S}_{DS} = \frac{1}{\Gamma(m_1)\Gamma(m_2)\Gamma(\alpha_1)\Gamma(\alpha_2)}, \tag{2.7}$$

   and $G_{p,q}^{m,n}(.|.)$ is the Meijer G-function [52, eq. (9.301)], which is a built-in function in MATLAB. The detailed proof of (2.6) can be found in Appendix B. Using (A.7),

the representation in (2.6) can be converted to an expression employing the Fox H-function as

$$f_{\gamma}\left(\gamma\right)=\frac{m_1 m_2}{\overline{\gamma}}\mathbb{S}_{DS}H_{2,2}^{2,2}\left(\frac{m_1 m_2}{\overline{\gamma}}\gamma\middle|\begin{matrix}(-\alpha_2,1),(-\alpha_1,1)\\(m_1-1,1),(m_2-1,1)\end{matrix}\right). \tag{2.8}$$

2. **Cumulative Distribution Function (CDF):**

The CDF of γ can be expressed as

$$F_{\gamma}(\gamma)=\int_0^{\gamma}f_{\gamma}(\gamma)d\gamma. \tag{2.9}$$

With the help of (A.13), (2.9) can be computed as [34]

$$F_{\gamma}\left(\gamma\right)=\mathbb{S}_{DS}G_{3,3}^{2,3}\left(\frac{m_1 m_2}{\overline{\gamma}}\gamma\middle|\begin{matrix}1-\alpha_2,1-\alpha_1,1\\m_1,m_2,0\end{matrix}\right). \tag{2.10}$$

3. **Moment-Generating Function (MGF):**

The MGF of γ can be evaluated as [53]

$$\mathcal{M}_{\gamma}(s)=\int_0^{\infty}e^{s\gamma}f_{\gamma}(\gamma)d\gamma. \tag{2.11}$$

With the help of (A.11), the integration in (2.11) can be expressed as

$$\mathcal{M}_{\gamma}(s)=\mathbb{S}_{DS}G_{3,2}^{2,3}\left(\frac{-m_1 m_2}{\overline{\gamma}s}\middle|\begin{matrix}1,1-\alpha_2,1-\alpha_1\\m_1,m_2\end{matrix}\right). \tag{2.12}$$

4. **Amount of fading:**

The amount of fading, $\mathcal{AF}$, is a measure of the severity of the channel by itself, which can be calculated as [53]

$$\mathcal{AF}=\frac{\mathbb{E}(\gamma^2)}{\left(\mathbb{E}(\gamma)\right)^2}-1, \tag{2.13}$$

where

$$\mathbb{E}(\gamma^n)=\int_0^{\infty}\gamma^n f_{\gamma}(\gamma)d\gamma, \tag{2.14}$$

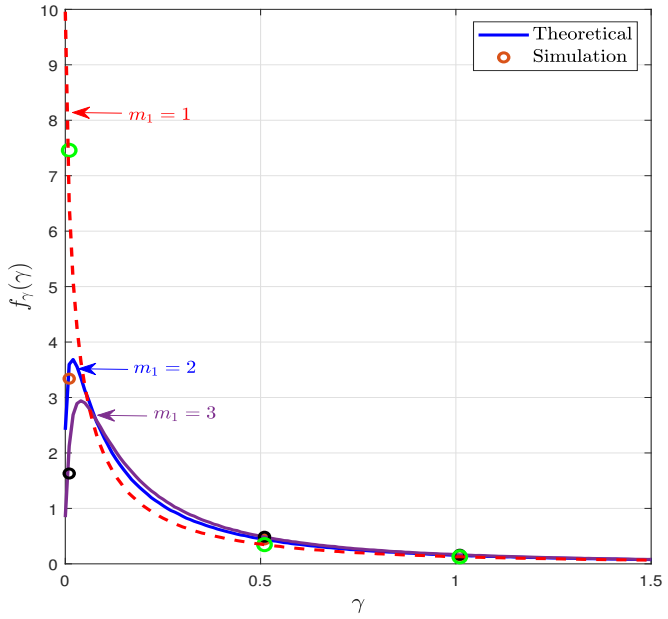

(a) Varying m_1 ($\alpha_1 = 2$).

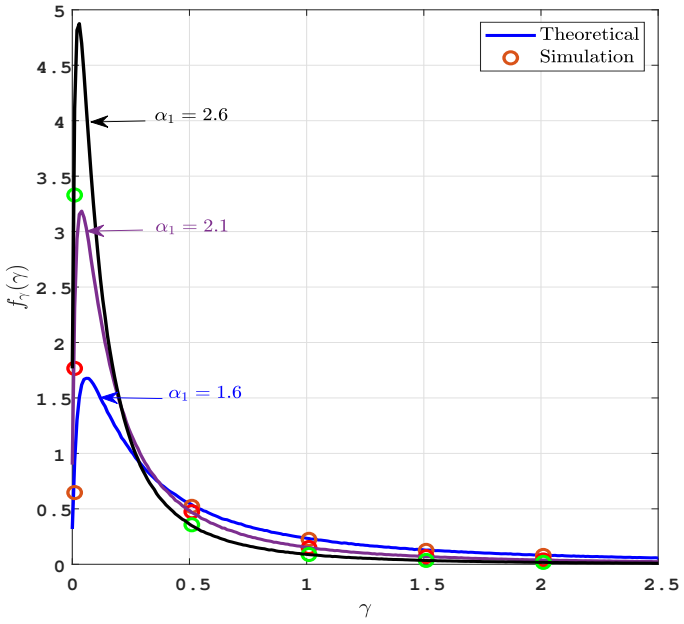

(b) Varying α_1 ($m_1 = 3.1$).

Figure 2.2: PDF of received SNR (DS case) under the effect of varying α_1 and m_1.

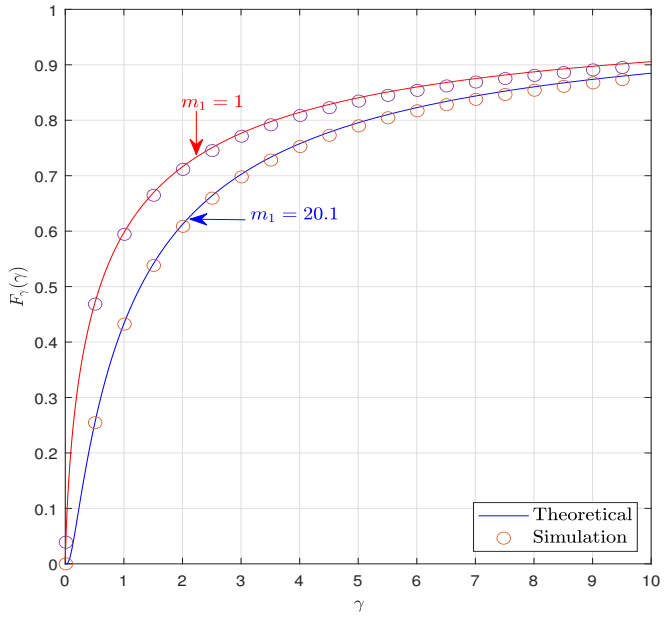

(a) Varying m_1 ($\alpha_1 = 1.1$).

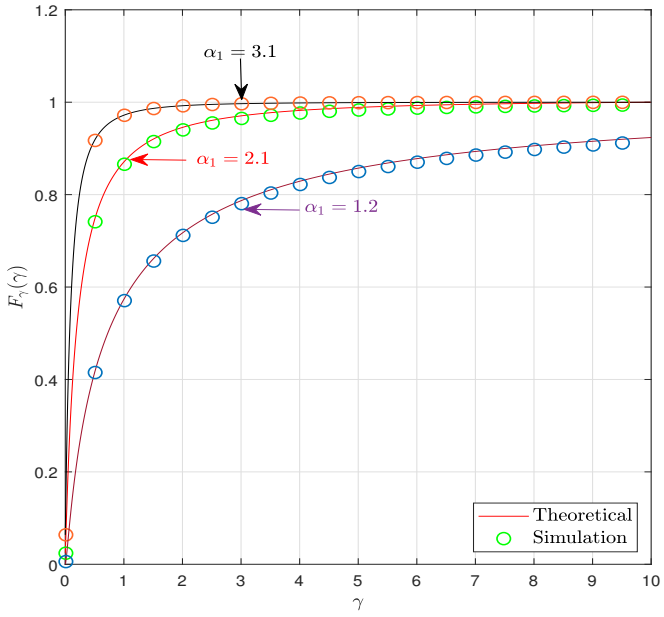

(b) Varying α_1 ($m_1 = 2.1$).

Figure 2.3: CDF of received SNR (DS case) under the effect of varying α_1 and m_1.

where $\mathbb{E}\{.\}$ denotes expectation. With the help of (A.14), $\mathbb{E}(\gamma^2)$ and $\mathbb{E}(\gamma)$ can be evaluated for the DS case, as shown in (2.15) and (2.16), respectively.

$$\mathbb{E}(\gamma^2) = \mathbb{S}_{DS}(\frac{m_1 m_2}{\overline{\gamma}})^{-2}\Gamma(m_1+2)\Gamma(m_2+2)\Gamma(\alpha_1-2)\Gamma(\alpha_2-2). \tag{2.15}$$

$$\mathbb{E}(\gamma) = \mathbb{S}_{DS}(\frac{m_1 m_2}{\overline{\gamma}})^{-1}\Gamma(m_1+1)\Gamma(m_2+1)\Gamma(\alpha_1-1)\Gamma(\alpha_2-1). \tag{2.16}$$

By substituting (2.15) and (2.16) into (2.13), we can obtain the amount of fading final expression as

$$\mathcal{AF} = \frac{\Gamma(m_1+2)\Gamma(m_2+2)\Gamma(\alpha_1-2)\Gamma(\alpha_2-2)}{\mathbb{S}_{DS}[\Gamma(m_1+1)\Gamma(m_2+1)\Gamma(\alpha_1-1)\Gamma(\alpha_2-1)]^2} - 1. \tag{2.17}$$

5. **Statistics of the received signal envelope:**

   The PDF and CDF of the received signal envelope can be derived through (2.6) and (2.10) through a change of variable as follows [54]

$$f_r(r) = 2r f_\gamma\left(r^2\right). \tag{2.18}$$

$$F_r(r) = F_\gamma\left(r^2\right). \tag{2.19}$$

$\overline{\gamma}$ will be replaced by $\mathbb{E}(r^2)$.

Figures 2.2 and 2.3 illustrate the PDF and CDF of the received SNR, respectively. Both the PDF and CDF plots demonstrate the effect of varying α_1 and m_1 ($m_2 = m_1 + 0.3$, $\alpha_2 = \alpha_1 + 0.3$, and $\overline{\gamma} = 1$) using the analytical expression of the PDF and Monte Carlo simulation. As α values increase, the PDF curves get sharper and deviate from the average SNR value ($\overline{\gamma} = 1$), which indicates severe shadowing cases. As m values increase, the curves shift towards higher SNR values.

2.2.1.2 Single-Shadowing (SS) Communication Scenario

In the SS case, there is a single scattering region either around the UAV or the ground node as shown in Figure 2.4. In that case, the received SNR can be modeled as [34]

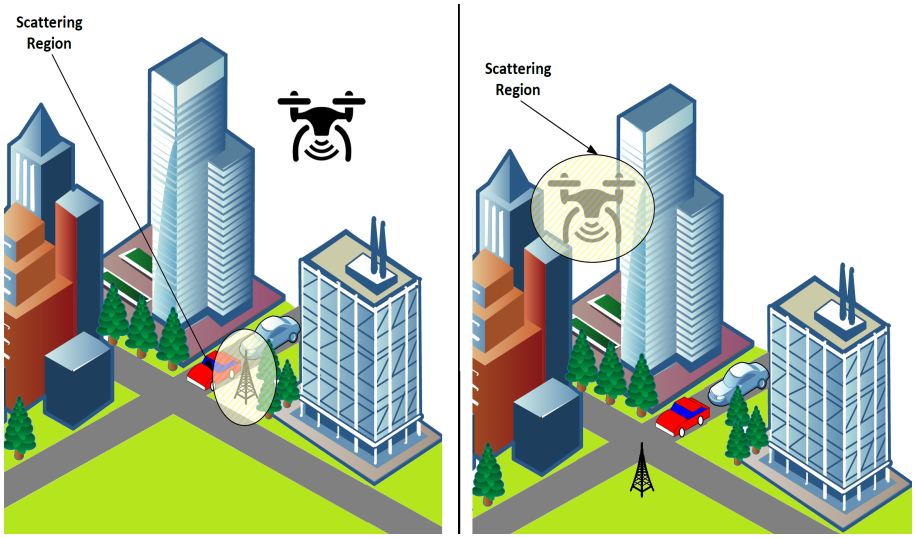

Figure 2.4: UAV-to-ground communication SS scenario.

$$\gamma = N_1^2 N_2^2 I. \tag{2.20}$$

1. **Probability Density Function (PDF):**

The PDF of the received SNR γ can be expressed as [34]

$$f_\gamma(\gamma) = \gamma^{-1} \mathbb{S}_{SS} G_{1,2}^{2,1}\left(\frac{m_1 m_2}{\overline{\gamma}}\gamma \middle| \begin{matrix} 1-\alpha \\ m_1, m_2 \end{matrix}\right), \tag{2.21}$$

where

$$\mathbb{S}_{SS} = \frac{1}{\Gamma(m_1)\Gamma(m_2)\Gamma(\alpha)}. \tag{2.22}$$

Using (A.7), the expression in (2.21) can be converted to an expression employing the Fox H-function as

$$f_\gamma(\gamma) = \frac{m_1 m_2}{\overline{\gamma}} \mathbb{S}_{SS} H_{1,2}^{2,1}\left(\frac{m_1 m_2}{\overline{\gamma}}\gamma \middle| \begin{matrix} (-\alpha, 1) \\ (m_1 - 1, 1), (m_2 - 1, 1) \end{matrix}\right). \tag{2.23}$$

2. **Cumulative Distribution Function (CDF):**

With the help of (A.13), the CDF of γ can be formulated as [34]

$$F_{\gamma}(\gamma) = \mathbb{S}_{SS} G_{2,3}^{2,2}\left(\frac{m_1 m_2}{\overline{\gamma}}\gamma \middle| \begin{matrix} 1-\alpha, 1 \\ m_1, m_2, 0 \end{matrix}\right). \tag{2.24}$$

3. **Moment-Generating Function (MGF):**

   The MGF of γ can be expressed as

$$\mathcal{M}_{\gamma}(s) = \mathbb{S}_{SS} G_{2,2}^{2,2}\left(\frac{-m_1 m_2}{\overline{\gamma} s} \middle| \begin{matrix} 1, 1-\alpha \\ m_1, m_2 \end{matrix}\right). \tag{2.25}$$

4. **Amount of Fading:**

   For the SS case, $\mathbb{E}(\gamma^2)$ and $\mathbb{E}(\gamma)$ can be evaluated as shown in (2.26) and (2.27), respectively.

$$\mathbb{E}(\gamma^2) = \mathbb{S}_{SS}\left(\frac{m_1 m_2}{\overline{\gamma}}\right)^{-2} \Gamma(m_1+2)\Gamma(m_2+2)\Gamma(\alpha-2). \tag{2.26}$$

$$\mathbb{E}(\gamma) = \mathbb{S}_{SS}\left(\frac{m_1 m_2}{\overline{\gamma}}\right)^{-1} \Gamma(m_1+1)\Gamma(m_2+1)\Gamma(\alpha-1). \tag{2.27}$$

   By substituting (2.26) and (2.27) into (2.13), we can obtain the amount of fading final expression as

$$\mathcal{AF} = \frac{\Gamma(m_1+2)\Gamma(m_2+2)\Gamma(\alpha-2)}{\mathbb{S}_{SS}[\Gamma(m_1+1)\Gamma(m_2+1)\Gamma(\alpha-1)]^2} - 1. \tag{2.28}$$

Figures 2.5 and 2.6 illustrate the PDF and CDF of the received SNR, respectively. Both the PDF and CDF plots demonstrate the effect of varying α_1 and m_1 ($m_2 = m_1 + 0.3$, $\alpha_2 = \alpha_1 + 0.3$, and $\overline{\gamma} = 1$) using the analytical expression of the PDF and Monte Carlo simulation.

2.2.2 Performance Analysis

In this subsection, we evaluate the performance of the UAV-to-ground channels for the SISO case in terms of outage probability, channel capacity, and ABER.

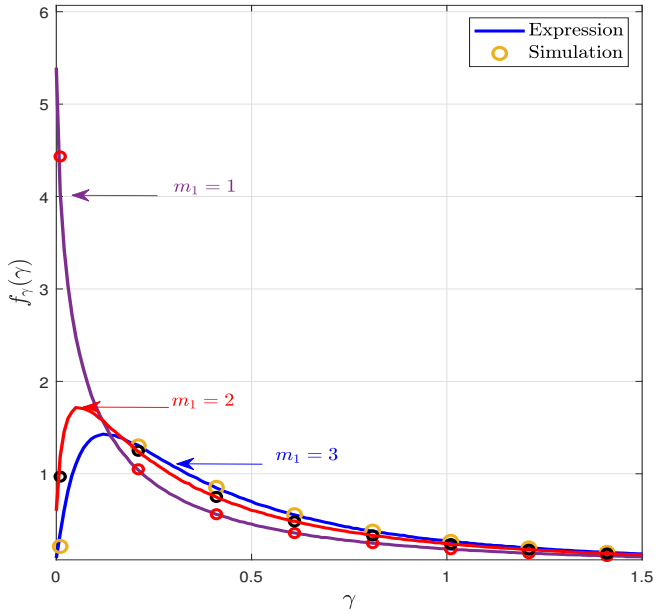

(a) Varying m_1 ($\alpha_1 = 2$).

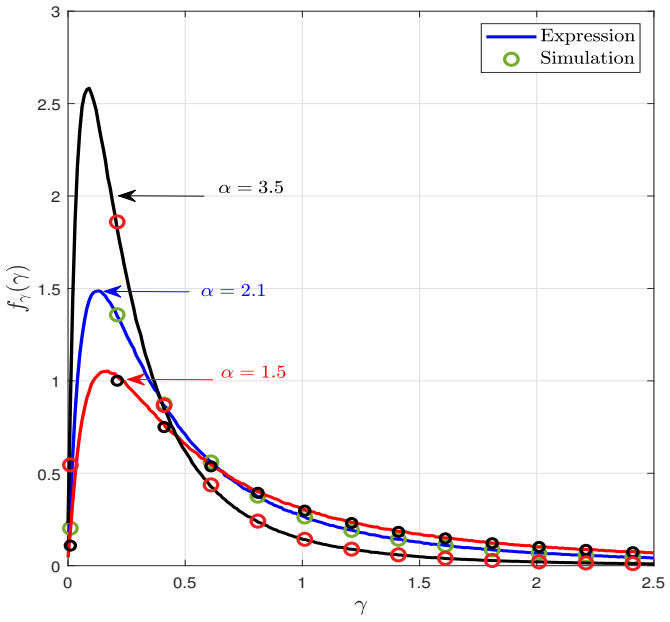

(b) Varying α ($m_1 = 3$).

Figure 2.5: PDF of received SNR (SS case) under the effect of varying α and m_1.

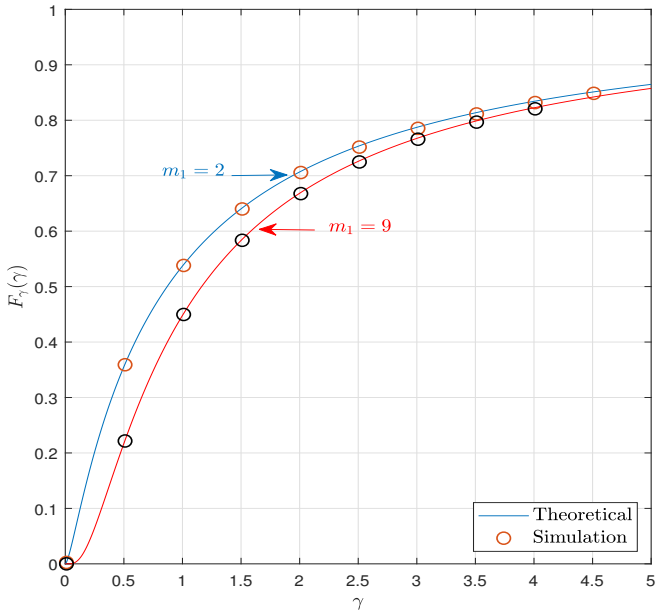

(a) Varying m_1 ($\alpha_1 = 2$).

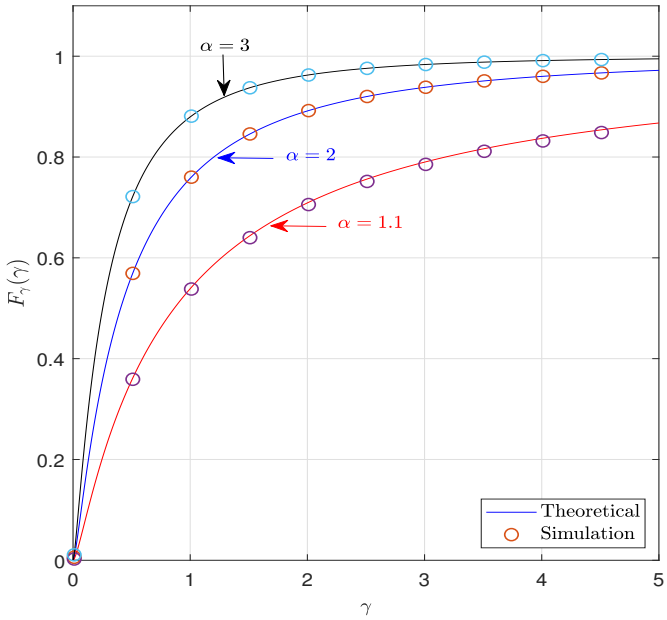

(b) Varying α ($m_1 = 3$).

Figure 2.6: CDF of received SNR (SS case) under the effect of varying α and m_1.

2.2.2.1 Outage Probability

Outage probability, denoted as P_{out}, is defined as the likelihood that the received SNR will fall below a certain level, γ_{th}, which can be calculated through the CDF expressions as follows.

1. **DS case:**

   For the case of DS, the outage probability can be expressed as [34]

$$\begin{aligned} P_{\text{out}}(\gamma_{th}), &= \mathbb{P}(\gamma \leq \gamma_{th}), \\ &= F_{\gamma}(\gamma_{th}), \\ &= \mathbb{S}_{DS} G_{3,3}^{2,3}\left(\frac{m_1 m_2}{\overline{\gamma}}\gamma_{th}\middle| \begin{matrix} 1-\alpha_2, 1-\alpha_1, 1 \\ m_1, m_2, 0 \end{matrix}\right), \end{aligned} \tag{2.29}$$

   where $\mathbb{P}(.)$ denotes the probability.

2. **SS case:**

   Similarly, for the SS case, the outage probability can be written as [34]

$$P_{\text{out}}(\gamma_{th}) = \mathbb{S}_{SS} G_{2,3}^{2,2}\left(\frac{m_1 m_2}{\overline{\gamma}}\gamma_{th}\middle| \begin{matrix} 1-\alpha, 1 \\ m_1, m_2, 0 \end{matrix}\right). \tag{2.30}$$

2.2.2.2 Ergodic Capacity

Shannon defined channel capacity, C_{ER}, as the maximum data rate that can be sent over any medium with negligible probability of error [55], which can be calculated for the AWGN channel as

$$C_{\text{ER}}(\gamma) = \mathbb{B}\log_2(1+\gamma), \tag{2.31}$$

where $\mathbb{B}$ is the channel bandwidth. In the case of a fading channel, the channel capacity needs to be averaged over the distribution of the fading channel as [53]

$$C_{\text{ER}} = \frac{\mathbb{B}}{\ln(2)}\int_0^{\infty} \ln(1+\gamma) f_{\gamma}(\gamma)\, d\gamma. \tag{2.32}$$

1. **DS case:**

   If we express $\ln(1+\gamma)$ in terms of the Meijer G-function as shown in (A.4), two Meijer G-functions are involved in the integration in (2.32), which can be formed into a closed-form expression with the help of (A.12), as

$$C_{\mathrm{ER}} = \frac{\mathbb{BS}_{DS}}{\ln(2)} G_{4,4}^{4,3}\left(\frac{m_1 m_2}{\overline{\gamma}}\middle| \begin{matrix} 1-\alpha_2, 1-\alpha_1, 0, 1 \\ m_1, m_2, 0, 0 \end{matrix}\right). \tag{2.33}$$

2. **SS case:**

   Similarly, for the SS case, C_{ER} can be evaluated as

$$C_{\mathrm{ER}} = \frac{\mathbb{BS}_{SS}}{\ln(2)} G_{3,4}^{4,2}\left(\frac{m_1 m_2}{\overline{\gamma}}\middle| \begin{matrix} 1-\alpha, 0, 1 \\ m_1, m_2, 0, 0 \end{matrix}\right). \tag{2.34}$$

2.2.2.3 Average Bit Error Rate

Using the CDF-based approach [56], the ABER, P_{be}, can be expressed as

$$P_{\mathrm{be}} = \frac{\kappa^{\beta}}{2\Gamma(\beta)} \int_0^{\infty} \gamma^{\beta-1} e^{-\kappa\gamma} F_{\gamma}(\gamma)\, d\gamma, \tag{2.35}$$

where $(\kappa, \beta) = (1, 0.5)$ for BPSK and $(\kappa, \beta) = (0.5, 0.5)$ for binary frequency shift keying (BFSK). The proof of this equation can be found in Appendix C.

- BPSK case

  1. **DS case:**

     By converting the exponential function into a Meijer G-function expression as shown in (A.3), the integration in (2.35) involves two Meijer G-functions, which can be evaluated as

$$P_{\mathrm{be}} = \frac{\mathbb{S}_{DS}}{2\Gamma(0.5)} G_{4,3}^{2,4}\left(\frac{m_1 m_2}{\overline{\gamma}}\middle| \begin{matrix} 1-\alpha_2, 1-\alpha_1, 1, 0.5 \\ m_1, m_2, 0 \end{matrix}\right). \tag{2.36}$$

  2. **SS case:**

Similarly, the ABER for the SS case can be expressed as:

$$P_{\text{be}} = \frac{\mathbb{S}_{SS}}{2\Gamma(0.5)} G_{3,3}^{2,3}\left(\frac{m_1 m_2}{\overline{\gamma}}\middle|\begin{matrix}1-\alpha, 1, 0.5\\ m_1, m_2, 0\end{matrix}\right). \tag{2.37}$$

- BFSK case

1. **DS case:**

   Using a similar approach, the ABER for the BFSK under the DS case can be evaluated as

$$P_{\text{be}} = \frac{\mathbb{S}_{DS}}{2\Gamma(0.5)} G_{4,3}^{2,4}\left(\frac{2m_1 m_2}{\overline{\gamma}}\middle|\begin{matrix}1-\alpha_2, 1-\alpha_1, 1, 0.5\\ m_1, m_2, 0\end{matrix}\right). \tag{2.38}$$

2. **SS case:**

   Similarly, the ABER for the SS case can be expressed as

$$P_{\text{be}} = \frac{\mathbb{S}_{SS}}{2\Gamma(0.5)} G_{3,3}^{2,3}\left(\frac{2m_1 m_2}{\overline{\gamma}}\middle|\begin{matrix}1-\alpha, 1, 0.5\\ m_1, m_2, 0\end{matrix}\right). \tag{2.39}$$

2.2.3 Numerical Results

In this subsection, we reproduce the numerical results published in [34] in order to verify the accuracy of the MATLAB codes, which is considered the basis for the accuracy of the upcoming chapters. For the Monte Carlo simulation, 10^6 realizations of fading channels are generated to validate the analytical expressions in the previous subsection.

In Figure 2.7, the normalized average channel capacity, $C_{\text{ER}}/\mathbb{B}$, is plotted as a function of the average received SNR, $\overline{\gamma}$. The channel parameters are selected to be $m_1 = 1.5, m_2 = 1.8$, and $\alpha_2 = \alpha_1 + 0.1$. It is clear that the SS case achieves a higher average channel capacity than the DS one since one of the shadowing regions is missing. As the channel experiences severe shadowing, indicated by an increase in the value of α_1, the capacity decreases.

In Figure 2.8, the ABER is plotted vs. the average received SNR, $\overline{\gamma}$, employing BPSK as the modulation scheme. The channel parameters are selected to be $m_2 = m_1 + 0.3$ and $\alpha_2 = \alpha_1 + 0.3$. It is clear that the SS case achieves a lower probability of error than the

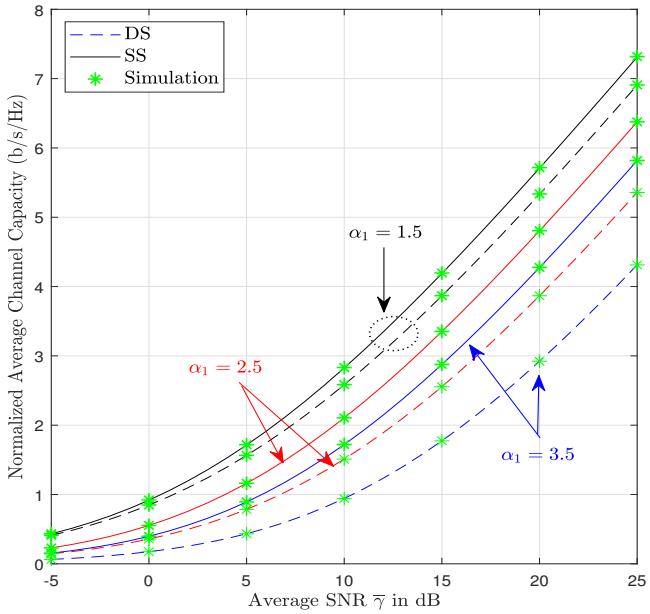

Figure 2.7: Normalized average channel capacity vs. average SNR $\overline{\gamma}$.

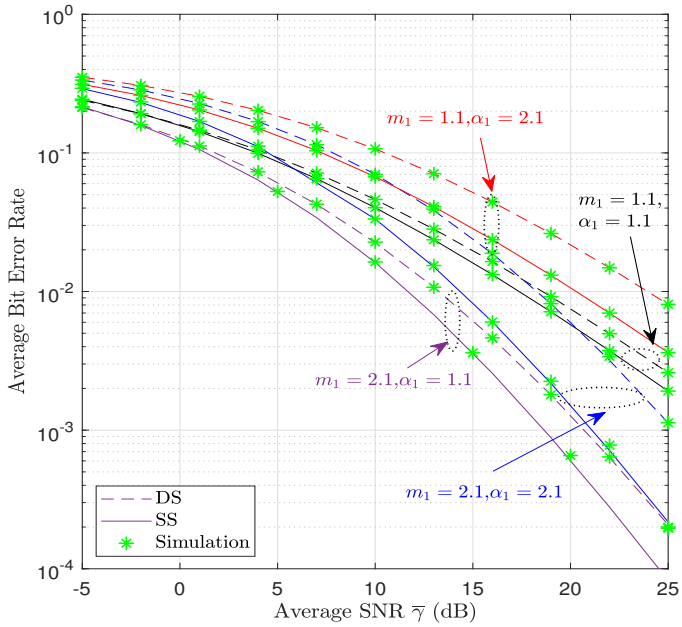

Figure 2.8: ABER vs. average SNR $\overline{\gamma}$ using BPSK.

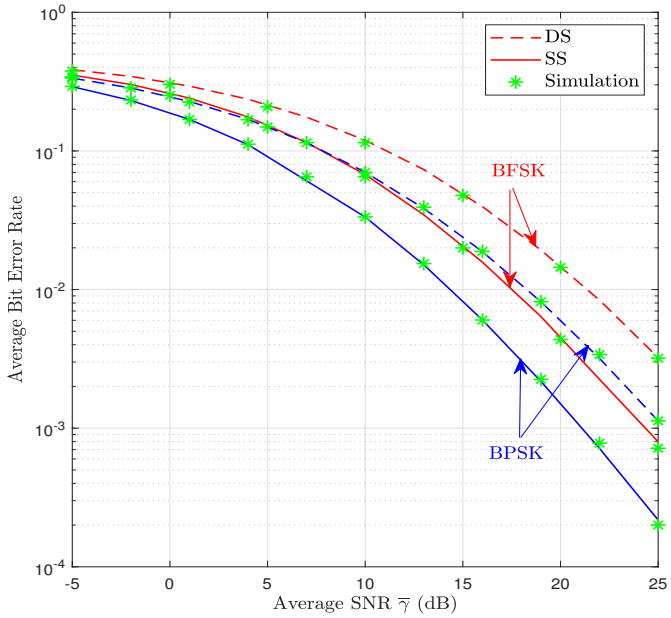

Figure 2.9: ABER vs. average SNR $\overline{\gamma}$ under different modulation schemes.

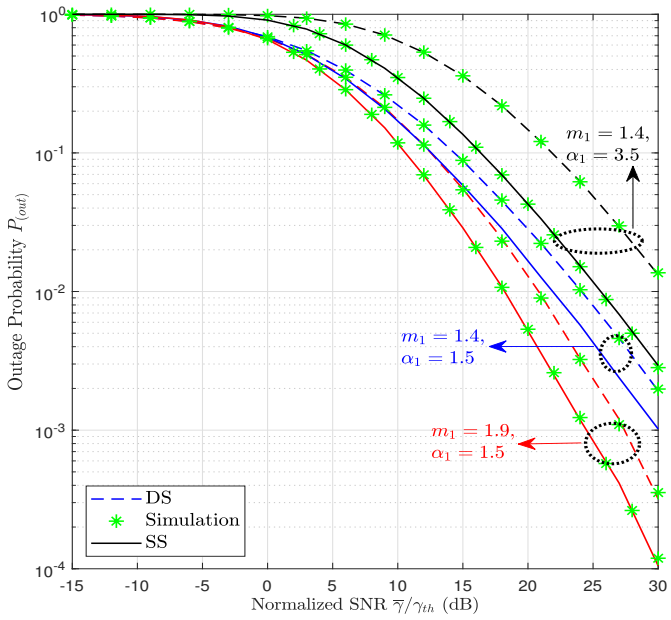

Figure 2.10: Outage probability versus normalized SNR $\overline{\gamma}/\gamma_{th}$ in dB.

DS one due to the absence of one of the shadowing areas. As m_1 increases, which indicates lighter fluctuations in the received signal, the ABER decreases.

In Figure 2.9, the ABER is plotted vs. the average received SNR, $\overline{\gamma}$, employing BPSK and BFSK. The channel parameters are selected to be $m_1 = \alpha_1 = 2.1$, $m_2 = 2.4$, and $m_2 = \alpha_2 = 2.4$. It is clear that there is a 3 dB gap between the BPSK and BFSK curves.

In Figure 2.10, the outage probability is plotted as a function of the normalized SNR, $\overline{\gamma}/\gamma_{th}$, value in dB under different channel conditions. The channel parameters were selected to be $m_2 = m_1 + 0.2$ and $\alpha_2 = \alpha_1 + 0.1$. The outage probability declines as the channel conditions improve by increasing m_1 or decreasing α_1.

2.3 Summary

In this chapter, we have presented an overview of current UAV signals and UAV-to-ground channel models. Throughout this discussion, a perfect phase recovery at the Rx was assumed. However, considering the mobility of UAVs, the likelihood of imperfect phase recovery increases significantly. In the next chapter, we will provide a mathematical analysis of the error probability under scenarios involving phase mismatch, addressing the implications of imperfect phase recovery on the system.

Chapter 3

Error Probability under Phase Noise

In the previous chapter, we assumed a perfect phase reference between the Tx and Rx. In practice, an imperfect phase recovery occurs, especially in UAV-to-ground communications, due to the mobility of the UAV, which can be mathematically modeled by Gaussian or Tikhonov (von Mises) distributions [57]. Sources of phase errors stem from quantization errors. Even though receivers can employ analog-to-digital converters with numerous quantization levels, minimizing errors, heavily quantized phase feedback results in substantial communication overhead [58]. The degradation in phase recovery significantly impacts the ABER performance of coherent digital modulations, particularly those reliant on encoding data via phase variations on a carrier wave, such as BPSK, QPSK, and MPSK. Incorporating phase noise into receiver performance assessment not only enhances practical analysis but also augments the potential for designing improved systems. The error probability due to imperfect phase recovery has been the focus of several papers investigating their effect on communications systems operating in different fading environments, such as Rayleigh [59], Nakagami-m [60], and α-μ fading [61].

The contributions of this chapter are as follows.

- Closed-form expressions for the ABER of BPSK and QPSK in the presence of phase noise that follows Tikhonov or Gaussian distributions.
- Closed-form expressions for the ASER of MPSK under the Tikhonov-distributed phase error.

- The expressions derived in this chapter are then verified by comparing them against the results obtained through Monte Carlo simulations.

This chapter is organized as follows. Section 3.1 describes the statistics of phase noise. In Section 3.2, the ABER of BPSK and QPSK analyses is derived under Tikhonov and Gaussian distributions. In section 3.3, the ASER of MPSK analysis is derived under Tikhonov distribution. Section 3.4 discusses the simulation results. Finally, section 3.5 concludes the chapter.

3.1 Statistics of The Phase Error

3.1.1 Tikhonov Distribution

One of the statistical models to represent the phase error, denoted as ϕ, is the Tikhonov distribution, whose PDF can be expressed as [57]

$$f_{\Phi}(\phi) = \frac{\exp(\rho\cos(\phi))}{2\pi I_0(\rho)}, \qquad -\pi < \phi \leq \pi, \tag{3.1}$$

where $I_\nu(.)$ is the modified Bessel function of the first kind with order ν. Additionally, ρ $(0 \leq \rho \leq \infty)$ represents the loop SNR, which is the amount of SNR within the bandwidth of the phase-locked loop. When $\rho = 0$, the PDF becomes a uniform distribution, which happens if there is no signal synchronization between the Tx and Rx. As $\rho \to \infty$, the Rx becomes perfectly matched to the Tx, and ideal coherent detection occurs. A plot of its PDF can be found in Figure 3.1. As ρ increases, less variance occurs around the mean value $= 0$.

3.1.2 Gaussian Distribution

The Gaussian distribution is also used to model phase error, and its PDF can be expressed as [62]

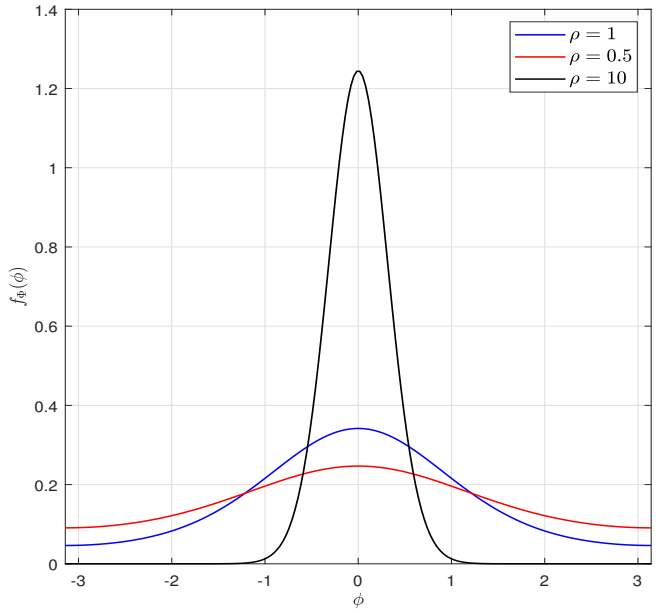

Figure 3.1: PDF of Tikhonov distribution.

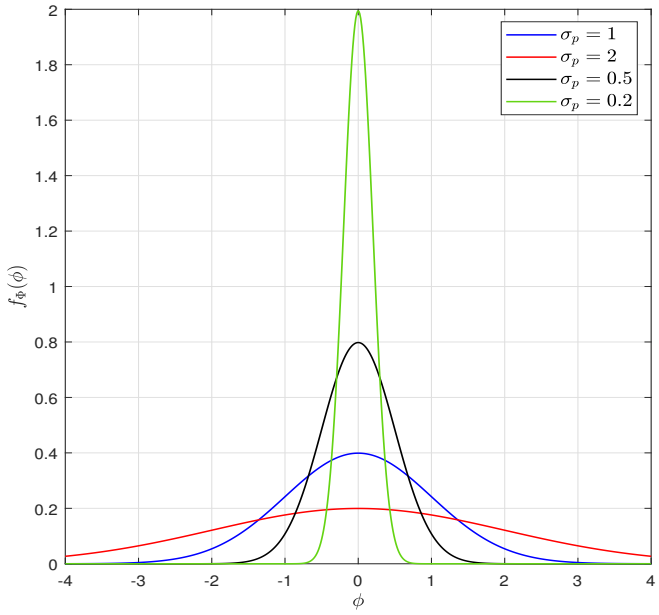

Figure 3.2: PDF of Gaussian distribution.

$$f_{\Phi}(\phi) = \frac{1}{\sqrt{2\pi\sigma_p^2}} \exp\left\{\frac{-\phi^2}{2\sigma_p^2}\right\}, \qquad -\infty < \phi < \infty, \tag{3.2}$$

where σ_p^2 represents the phase noise variance. A plot of its PDF can be found in Figure 3.2. When σ_p decreases, there is less tolerance for variance around the mean value, which is equal to 0.

3.2 BPSK and QPSK Error Analysis

In the AWGN channel, the conditional error probability under carrier phase recovery, assuming BPSK or QPSK modulations, can be expressed as [63]

$$P_e\left(e|\gamma,\phi\right) = \frac{1}{2}\text{erfc}\left(\sqrt{\omega\gamma}\cos\left(\phi+\zeta\right)\right), \tag{3.3}$$

where $(\omega,\zeta) = (1,0)$ for BPSK and $(2,\pi/4)$ for QPSK, respectively, and erfc(.) is the complementary error function. The term $\cos\left(\phi+\zeta\right)$ represents the loss factor due to the imperfect phase recovery.

In order to evaluate the ABER, denoted as P_{be},(3.3) needs to be averaged over all possible values of γ and ϕ, that is

$$P_{\text{be}} = \int_0^{\infty}\int_{-\pi}^{\pi} \frac{1}{2}\text{erfc}\left(\sqrt{\omega\gamma}\cos\left(\phi+\zeta\right)\right) f_{\gamma}(\gamma) f_{\phi}(\phi) d\phi d\gamma. \tag{3.4}$$

With the help of [64], the complementary error function can be represented as an infinite series as

$$\begin{aligned}\text{erfc}\left(\sqrt{\omega\gamma}\cos\left(\phi+\zeta\right)\right) = 1 - \frac{2}{\pi}\sum_{n=0}^{\infty} &\frac{\Gamma\left(n+0.5\right)\left(\omega\gamma\right)^{n+0.5}}{\left(-1\right)^{-n}\left(2n+1\right)!} \\ &\times {}_1F_1\left(n+0.5; 2n+2; -\omega\gamma\right) \\ &\times \cos[\left(2n+1\right)\left(\phi+\zeta\right)],\end{aligned} \tag{3.5}$$

where ${}_1F_1(.;.;.)$ is the confluent hypergeometric function of the first kind [52]. By substituting (3.5) into (3.4), the ABER can be expressed as

$$P_{\text{be}} = \frac{1}{2} - \frac{1}{\pi} \sum_{n=0}^{\infty} \frac{\Gamma\left(n+0.5\right)\left(\omega\right)^{n+0.5}}{\left(-1\right)^{-n}\left(2n+1\right)!} \tag{3.6a}$$

$$\times \int_{-\pi}^{\pi} \cos[\left(2n+1\right)\left(\phi+\zeta\right)] f_{\Phi}(\phi) d\phi \tag{3.6b}$$

$$\times \int_{0}^{\infty} \gamma^{n+0.5} {}_1F_1\left(n+0.5; 2n+2; -\omega\gamma\right) f_{\gamma}(\gamma) d\gamma. \tag{3.6c}$$

By substituting (3.1) for the Tikhonov distribution, the integration in (3.6b) can be evaluated as [61]

$$\begin{aligned} \mathbb{I}_1 &= \frac{1}{2\pi I_0(\rho)} \int_{-\pi}^{\pi} \cos[\left(2n+1\right)\left(\phi+\zeta\right)] \exp(\rho\cos\phi) d\phi \\ &= \cos[\left(2n+1\right)\zeta] \frac{I_{2n+1}(\rho)}{I_0(\rho)}. \end{aligned} \tag{3.7}$$

If the phase noise follows the Gaussian distribution, the integral in (3.6b) can be evaluated as [61]

$$\begin{aligned} \mathbb{I}_2 &= \frac{1}{\sqrt{2\pi\sigma_p^2}} \int_{-\pi}^{\pi} \cos[\left(2n+1\right)\left(\phi+\zeta\right)] \exp\left\{\frac{-\phi^2}{2\sigma_p^2}\right\} d\phi \\ &= \cos[\left(2n+1\right)\zeta] \exp\left(-0.5\sigma_p^2\left(2n+1\right)^2\right). \end{aligned} \tag{3.8}$$

Next, the confluent hypergeometric function in (3.6c) can be expressed in terms of the Meijer G-function, as shown in (A.6) in Appendix A, as [52]

$${}_1F_1\left(n+0.5; 2n+2; -\omega\gamma\right) = \mathbb{C} G_{1,2}^{1,1}\left(\omega\gamma \middle| \begin{matrix} -n+0.5 \\ 0, -2n-1 \end{matrix}\right), \tag{3.9}$$

where $\mathbb{C} = \frac{\Gamma(2n+2)}{\Gamma(n+0.5)}$.

3.2.1 DS Case

For the DS case, if we substitute (2.6) into (3.6c), (3.6c) involves the multiplication of two Meijer G-functions, which can be evaluated, as shown in (A.12) in Appendix A, as

$$\begin{aligned}\mathbb{I}_3 =&\omega^{-(n+0.5)}\mathbb{S}_{DS}\mathbb{C}\\ &\times G_{3,4}^{3,3}\left(\frac{m_1m_2}{\omega\overline{\gamma}}\middle|\begin{matrix}1-\alpha_2, 1-\alpha_1, 0.5-n, 1.5+n\\ m_1, m_2, 0\end{matrix}\right).\end{aligned} \tag{3.10}$$

Hence, the final expression of the ABER for the DS case can be written as

$$\begin{aligned}P_{\text{be}} = \frac{1}{2}-\frac{1}{\pi}\sum_{n=0}^{\infty}\frac{\Gamma\left(n+0.5\right)}{\left(-1\right)^{-n}\left(2n+1\right)!}\mathbb{I}_f\mathbb{S}_{DS}\mathbb{C}\\ \times G_{3,4}^{3,3}\left(\frac{m_1m_2}{\omega\overline{\gamma}}\middle|\begin{matrix}1-\alpha_2, 1-\alpha_1, 0.5-n, 1.5+n\\ m_1, m_2, 0\end{matrix}\right),\end{aligned} \tag{3.11}$$

where $\mathbb{I}_f$ is the expression computed in (3.7) for the Tikhonov distribution or in (3.8) for the Gaussian one respectively.

3.2.2 SS Case

Similarly for the SS case, if (2.17) is substituted into (3.6c), (3.6c) involves the multiplication of two Meijer G-functions, which can be expressed, as shown in (A.12) in Appendix A, as

$$\begin{aligned}\mathbb{I}_4 =&\omega^{-(n+0.5)}\mathbb{S}_{SS}\mathbb{C}\\ &\times G_{3,3}^{2,3}\left(\frac{m_1m_2}{\omega\overline{\gamma}}\middle|\begin{matrix}1-\alpha, 0.5-n, 1.5+n\\ m_1, m_2, 0\end{matrix}\right).\end{aligned} \tag{3.12}$$

Hence, the final expression of the ABER for the SS case can be written as

$$\begin{aligned}P_{\text{be}} = \frac{1}{2}-\frac{1}{\pi}\sum_{n=0}^{\infty}\frac{\Gamma\left(n+0.5\right)}{\left(-1\right)^{-n}\left(2n+1\right)!}\mathbb{I}_f\mathbb{S}_{SS}\mathbb{C}\\ \times G_{3,3}^{2,3}\left(\frac{m_1m_2}{\omega\overline{\gamma}}\middle|\begin{matrix}1-\alpha, 0.5-n, 1.5+n\\ m_1, m_2, 0\end{matrix}\right).\end{aligned} \tag{3.13}$$

3.3 M-PSK Error Analysis

The exact symbol error probability, P_{se}, of MPSK modulation schemes, with M modulation order, in the presence of AWGN and imperfect error phase recovery, that follows Tikhonov distribution, can be calculated as [65]

$$P_{\text{se}}(\gamma) = \frac{M-1}{M} - \frac{2}{\sqrt{\pi} I_o(\rho)} \sum_{n=1}^{\infty} \frac{I_n(\rho) \sin\left(n\pi/M\right)}{n\Gamma\left(\frac{n}{2}+0.5\right) 2^n} \left(\log_2\left(M\right)\right)^{\frac{n}{2}} \times \gamma^{\frac{n}{2}} {}_1F_1\left(\frac{n}{2}; n+1; -\log_2\left(M\right)\gamma\right). \tag{3.14}$$

In order to evaluate the ASER, (3.14) needs to be averaged over all possible values of γ, that is

$$P_{\text{se}} = \frac{M-1}{M} - \frac{2}{\sqrt{\pi} I_o(\rho)} \sum_{n=1}^{\infty} \frac{I_n(\rho) \sin\left(n\pi/M\right)}{n\Gamma\left(\frac{n}{2}+0.5\right) 2^n} \left(\log_2\left(M\right)\right)^{\frac{n}{2}} \tag{3.15a}$$

$$\times \int_0^{\infty} \gamma^{\frac{n}{2}} {}_1F_1\left(\frac{n}{2}; n+1; -\log_2\left(M\right)\gamma\right) f_{\gamma}(\gamma) d\gamma. \tag{3.15b}$$

3.3.1 DS Case

The confluent hypergeometric function in (3.15b) is expressed in terms of the Meijer G-function, as shown in (A.6) in Appendix A. if we substitute (2.6) into (3.15b), the integration in (3.15b) involves two Meijer G-functions, which can be evaluated in a closed-form expression. The final expression of the ASER under the DS case can be expressed as

$$P_{\text{se}} = \frac{M-1}{M} - \frac{2}{\sqrt{\pi} I_o(\rho)} \sum_{n=1}^{\infty} \frac{I_n(\rho) \sin\left(n\pi/M\right)}{n\Gamma\left(\frac{n}{2}+0.5\right) 2^n} \frac{\Gamma(n+1)}{\Gamma(0.5n)} \mathbb{S}_{DS} \times G_{3,4}^{3,3}\left(\frac{m_1 m_2}{\log_2\left(M\right)\overline{\gamma}} \middle| \begin{matrix} 1-\alpha_2, 1-\alpha_1, 1-\frac{n}{2}, 1+\frac{n}{2} \\ m_1, m_2, 0 \end{matrix}\right). \tag{3.16}$$

3.3.2 SS Case

Similarly, the final expression of the ASER under the SS case can be expressed as

$$P_{\text{se}} = \frac{M-1}{M} - \frac{2}{\sqrt{\pi} I_o(\rho)} \sum_{n=1}^{\infty} \frac{I_n(\rho) \sin(n\pi/M)}{n\Gamma\left(\frac{n}{2}+0.5\right) 2^n} \frac{\Gamma(n+1)}{\Gamma(0.5n)} \mathbb{S}_{SS} \times G_{3,3}^{2,3}\left(\frac{m_1 m_2}{\log_2(M)\,\overline{\gamma}} \middle| \begin{matrix} 1-\alpha, 1-\frac{n}{2}, 1+\frac{n}{2} \\ m_1, m_2, 0 \end{matrix} \right). \tag{3.17}$$

3.4 Simulation Results

This section presents numerical results to demonstrate the performance of UAV-to-ground communication with imperfect phase recovery. For the Monte Carlo simulation, 10^6 realizations of fading channels are generated to validate the analytical expressions from the preceding sections.

The channel parameters were selected to be $m_1 = 2.1$, $m_2 = 2.4$, $\alpha_1 = 2.1$, and $\alpha_2 = \alpha_1 + 0.3$. These parameters align with those presented in [34]. For ideal phase recovery, our analytically obtained ABER curves precisely match those from [34], serving as benchmarks for subsequent simulations. In Figures 3.3 and 3.4, the ABER of BPSK vs. the average received SNR in dB is plotted for varying ρ under Tikhonov and σ_p under Gaussian-distributed phases, respectively. The exact alignment between analytical curves and simulation results validates our analysis. Notably, for the Tikhonov distribution, ABER significantly increases as loop SNR, ρ, declines, while decreasing σ_p leads to lower ABER for the Gaussian case. At higher $\overline{\gamma}$, a flooring of the error rate occurs, representing an irreducible ABER dependent on loop SNR values. Our findings indicate that the DS case performs worse than the SS case, attributed to shadowing around both Tx and Rx in the former, while only one shadowing area exists in the latter. Hence, in the SS scenario, the irreducible ABER occurs at a higher SNR value compared to the DS one.

In Figure 3.5, the ASER of MPSK modulation schemes is plotted vs. the average received SNR in dB under the Tikhonov distribution ($\rho = 13$ dB) under the same channel parameters utilized in the previous figures. The simulation results precisely match the analytical curves, highlighting the increased deterioration in system performance for the 8-PSK system compared to QPSK. Therefore, for the 8-PSK, the irreducible ABER occurs at a lower SNR value compared to its QPSK counterpart.

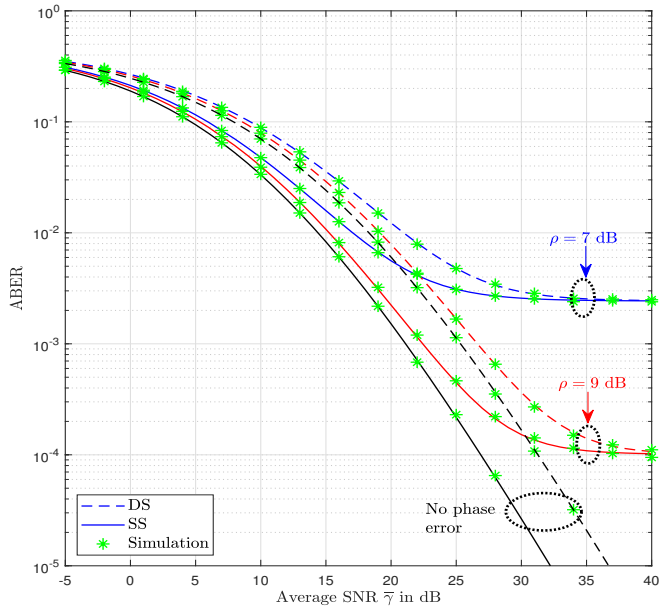

Figure 3.3: ABER of BPSK vs. average received SNR in dB under Tikhonov distribution.

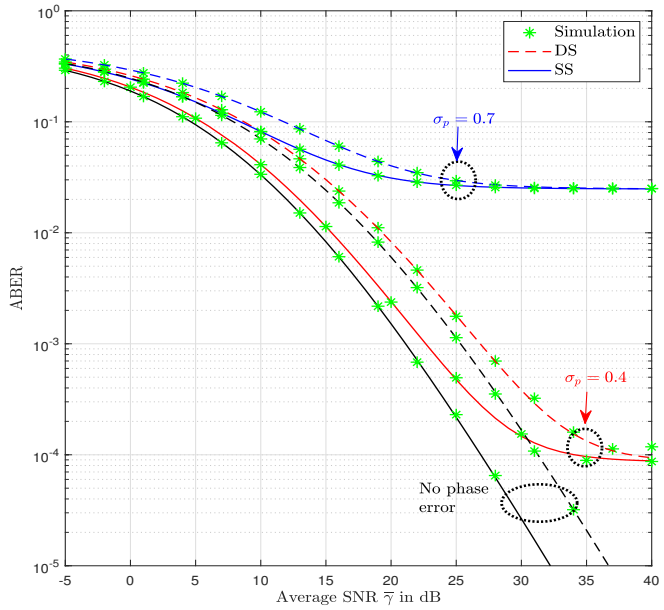

Figure 3.4: ABER of BPSK vs. average received SNR in dB under Gaussian distribution.

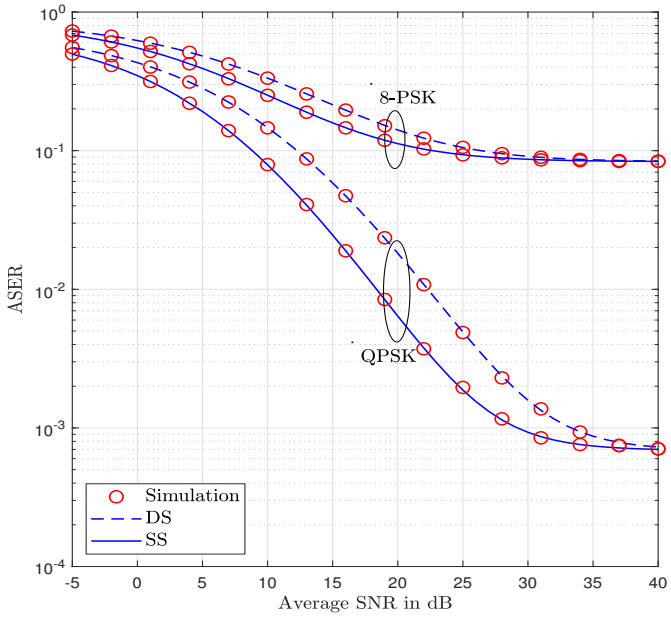

Figure 3.5: ASER against average SNR under UAV-to-ground fading channels and Tikhonov-distributed phase error ($\rho = 13$ dB).

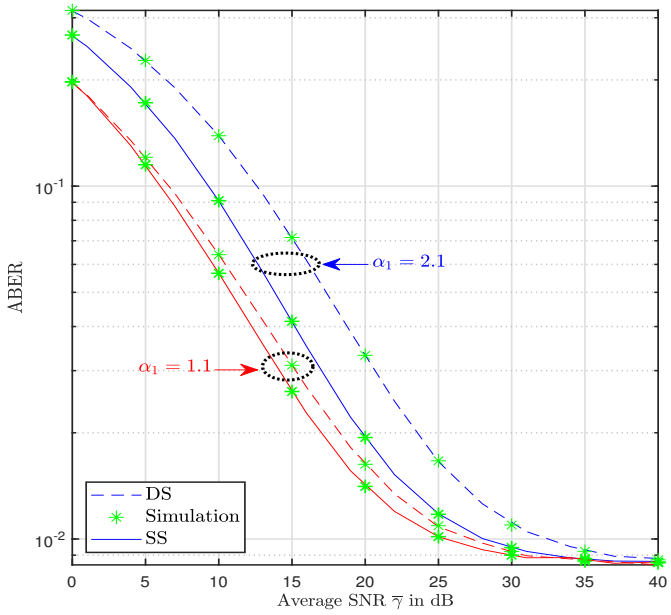

Figure 3.6: ABER of QPSK vs. average received SNR in dB under Tikhonov distribution.

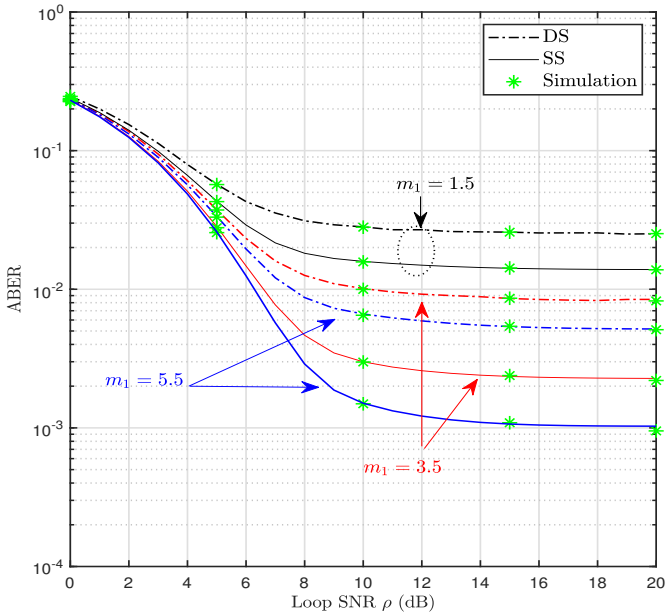

Figure 3.7: ABER of BPSK vs. loop SNR in dB under Tikhonov distribution.

Figure 3.6 shows the ABER of QPSK against the average received SNR in dB under the Tikhonov distribution following the same channel parameters in the previous figure while varying α and selecting $\rho = 10$ dB. The simulation and analytical curves match perfectly, confirming our analysis. Increasing α intensifies shadowing, resulting in a higher error probability. At high average SNR levels, the irreducible error probability, as depicted in Figures 3.5 and 3.6, is due to imperfect carrier phase recovery. Notably, this occurrence remains independent of the fading channel's parameter or its type, be it DS or SS.

Figure 3.7 plots ABER against loop SNR in dB, utilizing channel parameters set as ($m_2 = m_1$+0.3, $\alpha_1 = 1.8$, $\alpha_2 = 1.9$, and $\overline{\gamma} = 15$ dB). As loop SNR decreases, a higher ABER indicates severe phase mismatching between Tx and Rx. At an intermediate SNR value of 15 dB, increasing m_1 decreases the multipath effect, reducing the error probability. The ABER curves reach a floor due to the combined influences of channel fading and thermal noise at the Rx antenna, particularly at higher loop SNR values, and depend on fading channel characteristics.

3.5 Summary

In this chapter, closed-form expressions of the ABER of BPSK and QPSK as well as ASER of MPSK modulations are derived for the shadowed UAV-to-ground channels with imperfect phase recovery. The derived expressions are in terms of the Meijer G-function, which is a built-in MATLAB function. The theoretical expressions were verified through Monte-Carlo simulations. The results highlighted the impact of channel parameters on error probability when subjected to phase noise, particularly at intermediate SNR values. Conversely, at high SNR values, the presence of irreducible error probabilities predominantly stems from imperfect carrier phase recovery. Future work could explore and implement various phase error mitigation techniques aimed at minimizing errors in UAV-to-ground communication systems. Having analyzed a communication system operating in UAV-to-ground channels under practical conditions like phase noise, we evaluate various capacities of UAV-to-ground channels in the next chapter.

Chapter 4

Power Adaptation and Physical Layer Security of Shadowed UAV-to-Ground Channels

4.1 Introduction

In the 1940s, an information-theoretic approach to evaluating the ergodic channel capacity was pioneered by Claude Shannon [55]. In his work, he defined channel capacity as the channel's mutual information maximized over all possible input distributions. The channel capacity determines the maximum reliable data rates that can be transmitted over wireless channels with an asymptotically small error probability. Then, in 1975, Wyner proposed his wiretap model to ensure secure communication against an existing eavesdropper. This wiretap model results in a decrease in the achievable rate [66].

Prior research has overlooked the evaluation of the UAV-to-ground channel's ergodic capacity concerning diverse power adaptation schemes as well as their effective capacity. Furthermore, resolving the impact of shadowing on the physical layer security performance in UAV-to-ground communication remains unaddressed. Addressing these crucial gaps not only advances our understanding of UAV-ground communication but also holds promise for enhancing the reliability and security of such channels in practical applications.

The contributions of this chapter are as follows:

1. Firstly, we examine the UAV-to-ground channel capacity under different power adaptation schemes:
   (a) Optimal rate adaptation with fixed power (ORA)
   (b) Optimal power and rate adaptation (OPRA)
   (c) Channel inversion with fixed rate (CIFR)
   (d) Truncated channel inversion with fixed rate (TIFR)
2. Then, closed-form expressions of the effective capacity are evaluated under UAV-to-ground channels. Effective capacity is important in order to guarantee quality of service (QoS) requirements for real-time applications.
3. Lastly, we analyze the physical layer security of these novel channel models, assuming the wiretap system model, in terms of average secrecy capacity (ASC), secrecy outage probability (SOP), and strictly positive secrecy capacity (SPSC). The reason behind focusing on physical layer security is that cryptography algorithms tend to require complex operations, which do not align with the UAV node due to its limited energy reserves on board [67]. Physical layer security exploits the randomness of the wireless channel in order to provide secure data transmission in the presence of an eavesdropper.

The rest of this chapter is organized as follows: In Section 4.2, the capacity analysis for different power adaptation methods is derived, which is followed by its simulation results in order to verify the derived analysis. In Section 4.3, the effective capacity is analyzed, followed by the presentation of simulation results aimed at validating the analysis we have derived. The physical layer security parameters are analyzed in section 4.4, which is accompanied by their simulation results. Finally, a summary of this chapter is presented in Section 4.5.

4.2 Power Adaptation Methods

In sub-section 4.2.1, we present the derivation of closed-form exact expressions for the channel capacity of the recently developed UAV-to-ground fading channels under different power adaptation strategies. In OPRA, the channel fade level is tracked by both the Tx and

Rx. Whereas in ORA, it is tracked by the Rx alone. Thus, the OPRA requires feedback between the Rx and Tx, which results in a higher level of complexity compared to the ORA scheme. Another two suboptimal adaptive techniques are considered, which are CIFR and TIFR. In each of them, the Tx adapts its transmit power while keeping the transmission rate constant. Thus, they require simpler encoder and decoder designs, but they exhibit a capacity penalty that can be large in severe fading [68]. These different power adaptation capacity expressions are compared by numerical results in sub-section 4.2.2, developed by Monte Carlo simulations, which verify all the derived closed-form expressions.

4.2.1 Capacity Analysis

4.2.1.1 Optimal Rate Adaptation (ORA)

In this scheme, the Tx does not adjust its transmit power and just employs a constant power to transmit a signal to the destination. The ergodic capacity can be evaluated as [55]

$$C_{\text{ORA}} = \frac{\mathbb{B}}{\ln(2)} \int_0^\infty \ln(1+\gamma) f_\gamma(\gamma)\, d\gamma. \tag{4.1}$$

1. **DS case:**

   first, we express $\ln(1+\gamma)$ into the Meijer G-function as shown in (A.4). By substituting (2.6) in (4.1), the integration in (4.1) involves the multiplication of two Meijer G-functions, which can be expressed, with the help of (A.12), in a closed-form expression as

$$C_{\text{ORA}} = \frac{\mathbb{B}\mathbb{S}_{DS}}{\ln(2)} G_{4,4}^{4,3}\left(\frac{m_1 m_2}{\overline{\gamma}}\middle| \begin{matrix} 1-\alpha_2, 1-\alpha_1, 0, 1 \\ m_1, m_2, 0, 0 \end{matrix}\right). \tag{4.2}$$

2. **SS case:**

   Similarly, if (2.23) is substituted in (4.1) for the SS case, C_{ORA} can be evaluated as

$$C_{\text{ORA}} = \frac{\mathbb{B}\mathbb{S}_{SS}}{\ln(2)} G_{3,4}^{4,2}\left(\frac{m_1 m_2}{\overline{\gamma}}\middle| \begin{matrix} 1-\alpha, 0, 1 \\ m_1, m_2, 0, 0 \end{matrix}\right). \tag{4.3}$$

4.2.1.2 Optimal Power and Rate Adaptation (OPRA)

In this power adaptation technique, the Tx adapts its transmit power, $P_t(\gamma)$, according to the instantaneous SNR value, given by [69]

$$P_t(\gamma) = \overline{P} \max\left(\left(\frac{1}{\gamma_o} - \frac{1}{\gamma}\right), 0\right), \tag{4.4}$$

where $\overline{P}$ is the average power and γ_o is the optimal threshold SNR level below which no signal is transmitted, whose value is determined by [69]

$$\int_{\gamma_o}^{\infty} \left(\frac{1}{\gamma_o} - \frac{1}{\gamma}\right) f_\gamma(\gamma)\, d\gamma = 1. \tag{4.5}$$

The channel capacity under this scheme can be evaluated as [69]

$$C_{\text{OPRA}} = \frac{\mathbb{B}}{\ln(2)} \int_{\gamma_o}^{\infty} \ln\left(\frac{\gamma}{\gamma_o}\right) f_\gamma(\gamma)\, d\gamma, \tag{4.6}$$

1. **DS case:**

   Using the Fox H-function representation in (2.8) and [70], C_{OPRA} can be evaluated, after some mathematical manipulations, for the DS case as

   $$C_{\text{OPRA}} = \frac{\mathbb{B}\mathbb{S}_{DS}}{\ln(2)} G_{4,4}^{4,2}\left(\frac{m_1 m_2}{\overline{\gamma}}\gamma_o \middle| \begin{matrix} 1-\alpha_1, 1-\alpha_2, 1, 1 \\ 0, 0, m_1, m_2 \end{matrix}\right), \tag{4.7}$$

   where the condition for γ_o is

   $$\frac{m_1 m_2}{\overline{\gamma}} \mathbb{S}_{DS} G_{3,3}^{3,2}\left(\frac{m_1 m_2}{\overline{\gamma}}\gamma_o \middle| \begin{matrix} -\alpha_1, -\alpha_2, 1 \\ -1, m_1 - 1, m_2 - 1 \end{matrix}\right) = 1, \tag{4.8}$$

   which can be evaluated numerically.

2. **SS case:**

   Utilizing the Fox H-function representation in (2.23) and [70], C_{OPRA} for the SS case can be evaluated as

   $$C_{\text{OPRA}} = \frac{\mathbb{B}\mathbb{S}_{SS}}{\ln(2)} G_{3,4}^{4,1}\left(\frac{m_1 m_2}{\overline{\gamma}}\gamma_o \middle| \begin{matrix} 1-\alpha, 1, 1 \\ 0, 0, m_1, m_2 \end{matrix}\right), \tag{4.9}$$

where the condition for γ_o is

$$\frac{m_1 m_2}{\overline{\gamma}} \mathbb{S}_{SS} G_{2,3}^{3,1}\left(\frac{m_1 m_2}{\overline{\gamma}} \gamma_o \middle| \begin{matrix} -\alpha, 1 \\ -1, m_1 - 1, m_2 - 1 \end{matrix}\right) = 1. \tag{4.10}$$

4.2.1.3 Channel Inversion with Fixed Rate (CIFR)

In this case, the Tx adjusts its transmit power in order to maintain a constant SNR at the Rx receiver. This can be achieved by inverting the instantaneous channel state. The average channel capacity under this scheme can be evaluated as [69]

$$C_{\text{CIFR}} = \mathbb{B} \log_2 \left(1 + \frac{1}{\int_0^\infty \gamma^{-1} f_\gamma(\gamma)\, d\gamma}\right). \tag{4.11}$$

1. **DS case:**

   By substituting (2.8) in (4.11) and using (A.11), the integration in (4.11) can be evaluated for the DS case as

$$\int_0^\infty \gamma^{-1} f_\gamma(\gamma)\, d\gamma = \mathbb{S}_{DS} \frac{m_1 m_2}{\overline{\gamma}} \Gamma(m_1 - 1)\Gamma(m_2 - 1)\Gamma(\alpha_1 + 1)\Gamma(\alpha_2 + 1). \tag{4.12}$$

2. **SS case:**

   Likewise, in the case of SS, the integration in equation (4.11) can be assessed as follows:

$$\int_0^\infty \gamma^{-1} f_\gamma(\gamma)\, d\gamma = \mathbb{S}_{SS} \frac{m_1 m_2}{\bar{\gamma}} \Gamma(m_1 - 1)\Gamma(m_2 - 1)\Gamma(\alpha + 1). \tag{4.13}$$

4.2.1.4 Truncated Channel Inversion with Fixed Rate (TIFR)

If the channel experiences deep fading, this requires a large amount of power to invert its instantaneous case. To avoid that, the channel inversion is only achieved above a fixed cut-off value, γ_c. If $\gamma < \gamma_c$, the channel is not used. The average channel capacity under this truncated channel inversion can be evaluated as [69]

$$C_{\text{TIFR}} = \mathbb{B}\log_2\left(1+\frac{1}{\int_{\gamma_c}^{\infty}\gamma^{-1}f_\gamma(\gamma)\,d\gamma}\right)\mathbb{P}(\gamma>\gamma_c), \tag{4.14}$$

where γ_c is selected either to maximize C_{TIFR} or to achieve a specified outage probability.

1. **DS case:**

   With the help of [70], the integration in (4.14) for the DS case can be evaluated as

$$\int_{\gamma_c}^{\infty}\frac{f_\gamma(\gamma)}{\gamma}d\gamma = \mathbb{S}_{DS}\frac{m_1m_2}{\overline{\gamma}}G_{3,3}^{2,3}\left(\frac{m_1m_2}{\overline{\gamma}}\gamma_c\middle|\begin{matrix}-\alpha_2,-\alpha_1,1\\0,m_1-1,m_2-1\end{matrix}\right). \tag{4.15}$$

   $\mathbb{P}(\gamma>\gamma_c)$ can be computed as

$$\mathbb{P}(\gamma>\gamma_c) = 1-\mathbb{S}_{DS}G_{3,3}^{2,3}\left(\frac{m_1m_2}{\overline{\gamma}}\gamma_c\middle|\begin{matrix}1-\alpha_2,1-\alpha_1,1\\m_1,m_2,0\end{matrix}\right). \tag{4.16}$$

2. **SS case:**

   In a similar manner, the integration in equation (4.14) can be computed as

$$\int_{\gamma_c}^{\infty}\frac{f_\gamma(\gamma)}{\gamma}d\gamma = \mathbb{S}_{SS}\frac{m_1m_2}{\overline{\gamma}}G_{2,3}^{3,1}\left(\frac{m_1m_2}{\overline{\gamma}}\gamma_c\middle|\begin{matrix}-\alpha,1\\0,m_1-1,m_2-1\end{matrix}\right). \tag{4.17}$$

   The calculation of $\mathbb{P}(\gamma>\gamma_c)$ is achievable as

$$\mathbb{P}(\gamma>\gamma_c) = 1-\mathbb{S}_{SS}G_{2,3}^{2,2}\left(\frac{m_1m_2}{\overline{\gamma}}\gamma_c\middle|\begin{matrix}1-\alpha,1\\m_1,m_2,0\end{matrix}\right). \tag{4.18}$$

4.2.2 Numerical Results

In Figure 4.1, the normalized average channel capacity, $C/\mathbb{B}$, is plotted as a function of the average received SNR, $\overline{\gamma}$, in dB. For TIFR case, γ_c is 0.1. The fading channel parameters were chosen to become as ($m_1 = 1.5, m_2 = 1.8, \alpha_1 = 3.5$, and $\alpha_2 = 3.6$). The reason behind this choice is to match those produced in [34]. The normalized average channel capacity curves for the ORA scheme precisely match those curves produced in [34], which provides a benchmark for the rest of our analysis. As expected, the SS case achieves better

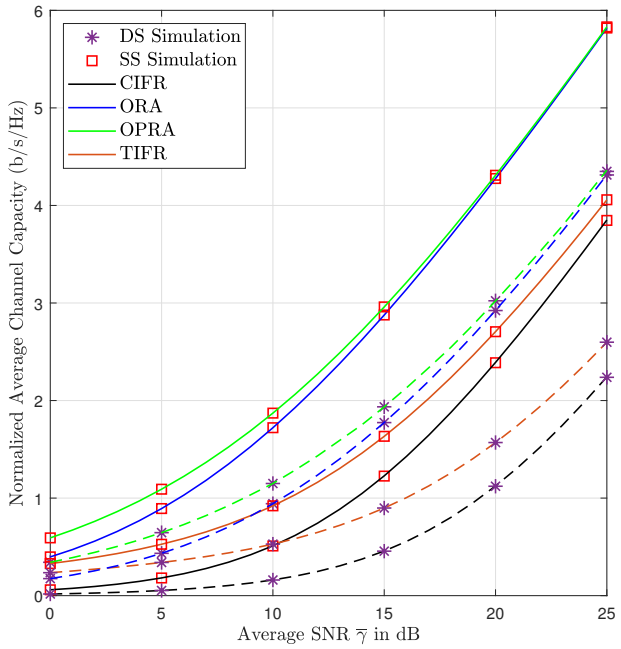

Figure 4.1: Normalized average channel capacity under different power adaptation schemes.

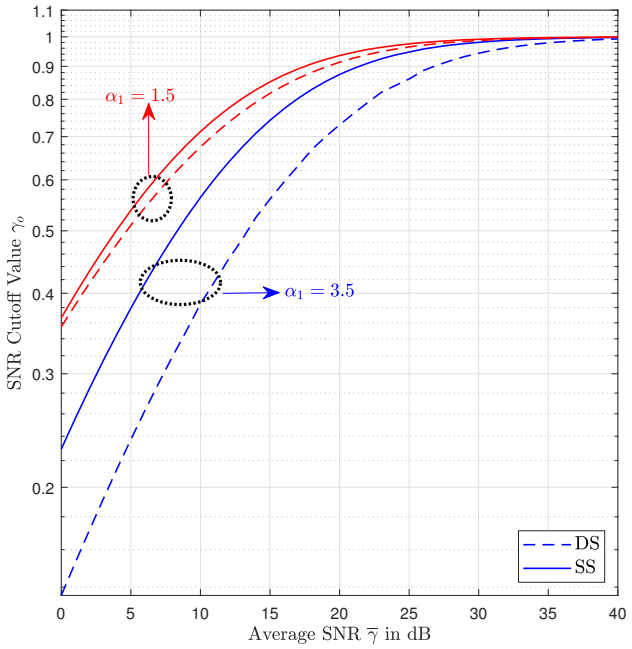

Figure 4.2: Optimal cutoff SNR, γ_o, versus the average SNR $\overline{\gamma}$ in dB.

performance than the DS one. This is because shadowing exists in two scattering regions around the Tx and Rx in the DS scenario. Whereas in the SS one, shadowing is present in only one of the two regions.

In addition, the OPRA method achieves optimal channel capacity in comparison to other methods. As opposed to using the fixed average power to send a signal in ORA, the Tx in the OPRA case modifies its transmit power in accordance with the instantaneous channel status. In the high SNR region, the average channel capacity of ORA and OPRA strategies converges. This is because $\gamma_o \to 1$ as $\overline{\gamma} \to \infty$, which indicates that the transmit power under the OPRA case becomes almost equal to the average power.

Figure 4.2 shows the optimal cut-off SNR values, γ_o, under OPRA versus the average SNR, $\overline{\gamma}$, in dB. The channel parameters are $m_1 = 1.5$, $m = 1.8$, and $\alpha_2 = \alpha_1 + 0.1$. In order to produce this figure, (4.8) and (4.10) were evaluated numerically for the DS case and SS cases, respectively. It is clear that γ_o increases as the average SNR increases, with a maximum value of 1. For the same value of average SNR, the cutoff value decreases as the channel goes through severe shadowing, which is indicated by increasing the value of α_1.

4.3 Effective Capacity

Shannon's ergodic capacity has been widely used, but it is not able to measure system performance under QoS constraints such as system delay and data rate. Effective capacity has been proposed as an alternative performance metric owing to its ability to take into account the system's delay constraint [71]. Additionally, computation of the effective capacity offers an efficient and convenient way to evaluate the statistical QoS performance of wireless systems from a networking perspective. This includes the analysis of resource allocation management, spectral efficiency, user scheduling schemes, and cognitive radio networks [72].

In subsection 4.3.1, we provide the derivation of closed-form expressions for the effective capacity of the UAV-to-ground communication link. These analytical formulas are subsequently compared to the numerical results in subsection 4.3.2, which are obtained through Monte Carlo simulations. These simulations validate all the closed-form expressions derived in our analysis.

4.3.1 Analysis

The effective capacity, denoted as C_{E}, can be computed as [72]

$$C_{\mathrm{E}} = \frac{-\mathbb{B}}{A} \log_2 \left(\mathbb{E}[(1+\gamma)^{-A}] \right), \tag{4.19}$$

where

$$\mathbb{E}[(1+\gamma)^{-A}] = \int_0^{\infty} (1+\gamma)^{-A} f_{\gamma}(\gamma) d\gamma. \tag{4.20}$$

The term $(1+\gamma)^{-A}$ can be expressed in terms of the Meijer G-function, as shown in (A.5). The parameter A is evaluated as [72]

$$A = \frac{\theta T \mathbb{B}}{\ln(2)}, \tag{4.21}$$

where θ is the buffer occupancy decay rate and T is the block length. It can be noted that the effective capacity aligns with Shannon's classic ergodic capacity when there is no delay constraint as θ approaches zero.

1. **DS case:**

   By substituting (2.8) in (4.20), the integration in (4.20) involves the multiplication of two Meijer G-functions, which can be expressed, with the help of (A.12), in a closed-form expression as

   $$\int_0^{\infty} (1+\gamma)^{-A} f_{\gamma}(\gamma) d\gamma = \frac{\mathbb{S}_{DS}}{\Gamma(A)} G_{3,3}^{3,3} \left(\frac{m_1 m_2}{\overline{\gamma}} \middle| \begin{matrix} 1-\alpha_2, 1-\alpha_1, 1 \\ m_1, m_2, A \end{matrix} \right). \tag{4.22}$$

   Thus, the final expression of the effective capacity for the DS case can be written as

   $$C_{\mathrm{E}} = \frac{-\mathbb{B}}{A} \log_2 \left(\frac{\mathbb{S}_{DS}}{\Gamma(A)} G_{3,3}^{3,3} \left(\frac{m_1 m_2}{\overline{\gamma}} \middle| \begin{matrix} 1-\alpha_2, 1-\alpha_1, 1 \\ m_1, m_2, A \end{matrix} \right) \right). \tag{4.23}$$

2. **SS case:**

   Similarly, for the SS case, the integration in (4.20) can be evaluated as

   $$\int_0^{\infty} (1+\gamma)^{-A} f_{\gamma}(\gamma) d\gamma = \frac{\mathbb{S}_{SS}}{\Gamma(A)} G_{2,3}^{3,2} \left(\frac{m_1 m_2}{\overline{\gamma}} \middle| \begin{matrix} 1-\alpha, 1 \\ m_1, m_2, A \end{matrix} \right). \tag{4.24}$$

Thus, the closed-form expression of the effective capacity for the SS case can be formulated as

$$C_{\mathrm{E}} = \frac{-\mathbb{B}}{A} \log_2 \left(\frac{\mathbb{S}_{SS}}{\Gamma(A)} G_{2,3}^{3,2} \left(\frac{m_1 m_2}{\overline{\gamma}} \middle| \begin{matrix} 1-\alpha, 1 \\ m_1, m_2, A \end{matrix} \right) \right). \tag{4.25}$$

4.3.2 Numerical Results

In Figure 4.3, the normalized effective capacity, $C_{\mathrm{E}}/\mathbb{B}$, is plotted as a function of the average received SNR, $\overline{\gamma}$, in dB. The fading channel parameters were chosen to be ($m_2 = m_1 + 0.2, \alpha_1 = 3.1$, and $\alpha_2 = 3.3$) and $A = 3$. The curves produced through our analysis precisely match those produced via Monte Carlo simulation, which in turn validates our analysis. As the value of m_1 increases, it becomes evident that capacity improves because the multipath effect of the channel diminishes. As anticipated, the SS scenario outperforms the DS scenario in terms of performance.

In Figure 4.4, the normalized effective capacity is plotted versus the parameter A. The parameters characterizing the fading channel were deliberately set as follows: $m_1 = 1.5$, $m_2 = 1.8$, $\alpha_2 = \alpha_1 + 0.2$, and $\overline{\gamma} = 10$ dB. As the value of A increases, the effective capacity decreases. The normalized effective capacity decreases as the channel experiences significant shadowing. This is evident when the parameter α_1 increases.

4.4 Physical Layer Security

With the vast range of communications infrastructure related to beyond 5G networks, securing data transmission from malicious threats like jamming, spoofing, and eavesdropping is crucial [73–76]. Physical layer security can provide immunity against these threats during communication processes. Despite the UAV's energy limitations, physical layer security stands as a suitable candidate for protection against eavesdropping without relying on complex cryptographic algorithms [77]. The wireless channel openness between a UAV and a ground-based Rx poses a significant vulnerability, enabling eavesdroppers to intercept sensitive information without signal transmission. To address this challenge, exploring the physical layer security of UAV-to-ground communications based on realistic channel models has been proposed as a crucial research direction [37].

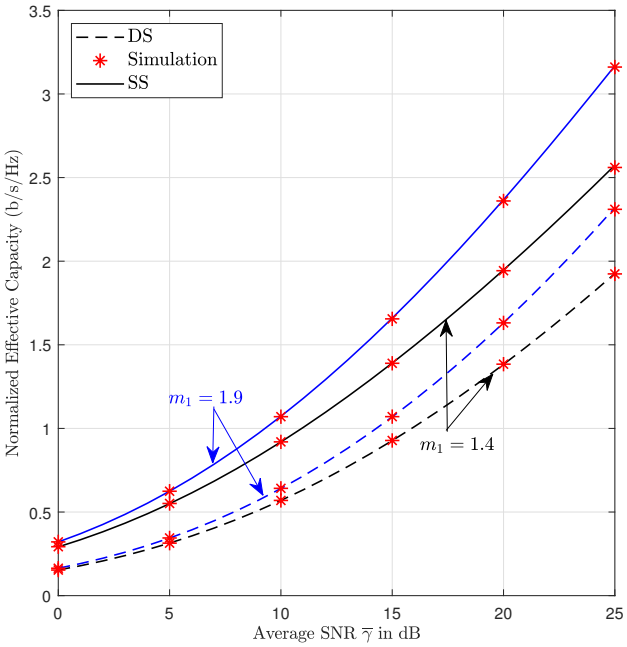

Figure 4.3: Normalized effective capacity versus average SNR in dB.

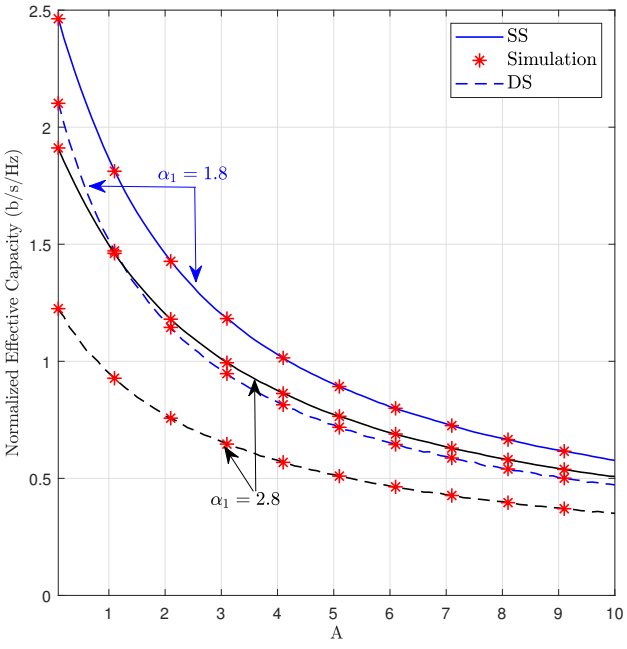

Figure 4.4: Normalized effective capacity versus A.

While prior studies, such as [78], have examined the physical layer security of UAV communications assuming LoS conditions, practical scenarios often involve impediments such as large obstacles [43], challenging the reliability of this assumption. A precoder design for millimeter-wave UAV communications based on physical layer security was proposed in [79, 80]. Recent research efforts have studied the physical layer security of UAV communications combined with other physical layer technologies such as intelligent reflective surfaces [67], multi-beam satellites [81], or millimeter simultaneous wireless information and power transfer (SWIPT) relay networks [82].

In light of the identified gaps in the state of the art, it can be stated that the physical layer security performance of shadowed UAV-to-ground channels, which have been validated by empirical measurements, is still a major issue that has to be resolved. The main contributions of our work are as follows:

- We analyze the physical layer security performance of the UAV-to-ground channel with shadowing [34] in terms of ASC, SOP, and SPSC.
- The proposed analysis is presented and verified by Monte-Carlo simulation results, which indicate the effect of channel parameters on the secrecy metrics.

4.4.1 The Wiretap Model

One of the extensively applied threat models in physical layer security research is the wiretap model [66], as shown in Figure 4.5. In this threat model, a message is sent by the Tx, located at the UAV, to the legitimate Rx (D) over the main channel. Meanwhile, over the eavesdropper channel, an eavesdropper (E) tries to decode the message from the signal it has received. Assuming they are sufficiently spaced, both Rxs experience independent UAV-to-ground fading channels. The received SNR at the desired Rx is denoted by γ_D, while the eavesdropper's received SNR is denoted by γ_E.

4.4.2 Security Analysis

4.4.2.1 Average Secrecy Capacity (ASC)

Secrecy capacity, denoted as C_{S}, is described as the difference in channel capacity between the main and wiretap channels. Specifically, it specifies the maximum secrecy rate at which

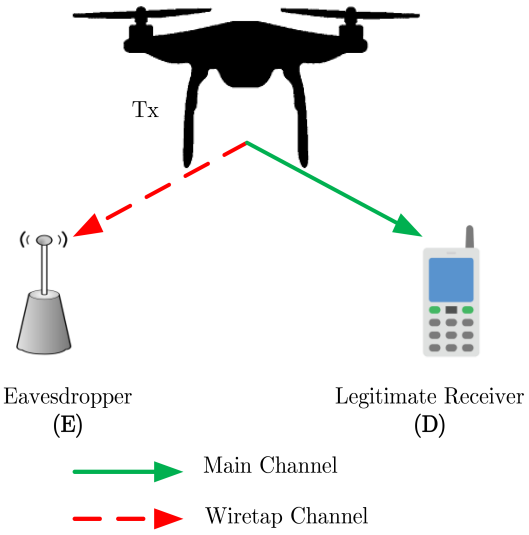

Figure 4.5: The wiretap channel model.

the secret information may be recovered at the Tx with confidence and yet be unrecoverable to the eavesdropper. The instantaneous secrecy capability can be evaluated as [83, 84]

$$C_{\mathrm{S}} = \max\left\{\log_2(1+\gamma_D) - \log_2(1+\gamma_E), 0\right\}, \tag{4.26}$$

where $\log_2(1+\gamma_D)$ and $\log_2(1+\gamma_E)$ are the capacity of the main and eavesdropper channels, respectively. The ASC can be computed as [83, 84]

$$\begin{aligned}
\overline{C_{\mathrm{S}}} &= \int_0^\infty \int_0^\infty C_s(\gamma_D, \gamma_E) f(\gamma_D, \gamma_E) d\gamma_D d\gamma_E \\
&= \underbrace{\int_0^\infty \log_2(1+\gamma_D) f_D(\gamma_D) F_E(\gamma_D) d\gamma_D}_{\mathbb{I}_1} \\
&+ \underbrace{\int_0^\infty \log_2(1+\gamma_E) f_E(\gamma_E) F_D(\gamma_E) d\gamma_E}_{\mathbb{I}_2} \\
&- \underbrace{\int_0^\infty \log_2(1+\gamma_E) f_E(\gamma_E) d\gamma_E}_{\mathbb{I}_3},
\end{aligned} \tag{4.27}$$

where $f(\gamma_D, \gamma_E) = f_D(\gamma_D) f_E(\gamma_E)$ is the joint PDF of γ_D and γ_E.

1. **DS case**

By rewriting $\log_2(1+\gamma) = \frac{1}{\ln(2)} G_{2,2}^{1,2}\left(\gamma \middle| \begin{matrix}1,1\\1,0\end{matrix}\right)$ as shown in (A.4) and using (2.6) and (2.10) for the DS case, the integrations $\mathbb{I}_1$ and $\mathbb{I}_2$ involve three Meijer G-functions, which can be expressed in terms of the bivariate Meijer G-function with the help of (A.15). The integration $\mathbb{I}_3$ involves two Meijer G-functions, which can be evaluated, with the help of (A.12), in terms of the Meijer G-function as expressed in (4.28).

$$\begin{aligned}\overline{C_{\mathrm{S}}} &= \mathbb{C}_{DS} G_{2,2:3,3:2,2}^{2,1:2,3:2,2}\left(\frac{m_{1E}m_{2E}}{\overline{\gamma_E}}, \frac{m_{1D}m_{2D}}{\overline{\gamma_D}} \middle| \begin{matrix}0,1\\0,0\end{matrix} \middle| \begin{matrix}1-\alpha_{2E}, 1-\alpha_{1E}, 1\\ m_{1E}, m_{2E}, 0\end{matrix} \middle| \begin{matrix}1-\alpha_{2D}, 1-\alpha_{1D}\\ m_{1D}, m_{2D}\end{matrix}\right)\\ &+ \mathbb{C}_{DS} G_{2,2:3,3:2,2}^{2,1:2,3:2,2}\left(\frac{m_{1D}m_{2D}}{\overline{\gamma_D}}, \frac{m_{1E}m_{2E}}{\overline{\gamma_E}} \middle| \begin{matrix}0,1\\0,0\end{matrix} \middle| \begin{matrix}1-\alpha_{2D}, 1-\alpha_{1D}, 1\\ m_{1D}, m_{2D}, 0\end{matrix} \middle| \begin{matrix}1-\alpha_{2E}, 1-\alpha_{1E}\\ m_{1E}, m_{2E}\end{matrix}\right)\\ &- \frac{1}{\ln(2)\,\Gamma(m_{1_E})\,\Gamma(m_{2_E})\,\Gamma(\alpha_{1_E})\,\Gamma(\alpha_{2_E})} G_{4,4}^{4,3}\left(\frac{m_{1_E}m_{2_E}}{\overline{\gamma_E}}\gamma_E \middle| \begin{matrix}1-\alpha_{2_E}, 1-\alpha_{1_E}, 0, 1\\ m_{1_E}, m_{2_E}, 0, 0\end{matrix}\right),\end{aligned} \tag{4.28}$$

where $\mathbb{C}_{DS}$ is given as

$$\mathbb{C}_{DS} = \frac{1}{\ln(2)} \times \frac{1}{\Gamma(m_{1_E})\,\Gamma(m_{2_E})\,\Gamma(\alpha_{1_E})\,\Gamma(\alpha_{2_E})} \times \frac{1}{\Gamma(m_{1_D})\,\Gamma(m_{2_D})\,\Gamma(\alpha_{1_D})\,\Gamma(\alpha_{2_D})}. \tag{4.29}$$

2. **SS case:**

Similarly, for the SS case, the ASC can be evaluated as

$$\begin{aligned}\overline{C_{\mathrm{S}}} &= \mathbb{C}_{SS} G_{2,2:2,3:1,2}^{2,1:2,2:2,1}\left(\frac{m_{1E}m_{2E}}{\overline{\gamma_E}}, \frac{m_{1D}m_{2D}}{\overline{\gamma_D}} \middle| \begin{matrix}0,1\\0,0\end{matrix} \middle| \begin{matrix}1-\alpha_E, 1\\ m_{1E}, m_{2E}, 0\end{matrix} \middle| \begin{matrix}1-\alpha_D\\ m_{1D}, m_{2D}\end{matrix}\right)\\ &+ \mathbb{C}_{SS} G_{2,2:2,3:1,2}^{2,1:2,3:2,1}\left(\frac{m_{1D}m_{2D}}{\overline{\gamma_D}}, \frac{m_{1E}m_{2E}}{\overline{\gamma_E}} \middle| \begin{matrix}0,1\\0,0\end{matrix} \middle| \begin{matrix}1-\alpha_D, 1\\ m_{1D}, m_{2D}, 0\end{matrix} \middle| \begin{matrix}1-\alpha_E\\ m_{1E}, m_{2E}\end{matrix}\right)\\ &- \frac{1}{\ln(2)\,\Gamma(m_{1_E})\,\Gamma(m_{2_E})\,\Gamma(\alpha_E)} G_{3,4}^{4,2}\left(\frac{m_{1_E}m_{2_E}}{\overline{\gamma_E}}\gamma_E \middle| \begin{matrix}1-\alpha_E, 0, 1\\ m_{1_E}, m_{2_E}, 0, 0\end{matrix}\right).\end{aligned} \tag{4.30}$$

where $\mathbb{C}_{SS}$ is given as

$$\mathbb{C}_{SS} = \frac{1}{\ln(2)} \times \frac{1}{\Gamma(m_{1_E})\Gamma(m_{2_E})\Gamma(\alpha_E)} \times \frac{1}{\Gamma(m_{1_D})\Gamma(m_{2_D})\Gamma(\alpha_D)}. \tag{4.31}$$

4.4.2.2 Secrecy Outage Probability (SOP)

SOP, denoted as P_{sec}, is defined as the probability that the secrecy capacity will go below the threshold secrecy rate, denoted as R_s. The SOP can be computed as [83]

$$\begin{aligned} P_{\text{sec}} &= \mathbb{P}\{C_s(\gamma_D, \gamma_E) < R_s\} \\ &= \int_0^\infty F_D(e^{R_s}\gamma_E + e^{R_s} - 1) f_E(\gamma_E) d\gamma_E. \end{aligned} \tag{4.32}$$

1. **DS case**

   Thus, by using (2.6) and (2.10), the SOP for the DS can be expressed as

$$\begin{aligned} P_{\text{sec}} = \int_0^\infty \frac{\mathbb{C}_{DS}}{\gamma_E} G_{3,3}^{2,3}\left(\frac{m_{1_D} m_{2_D}}{\overline{\gamma_D}}(e^{R_s}\gamma_E + e^{R_s} - 1)\middle| \begin{matrix} 1-\alpha_{2_D}, 1-\alpha_{1_D}, 1 \\ m_{1_D}, m_{2_D}, 0 \end{matrix}\right) \\ \times G_{2,2}^{2,2}\left(\frac{m_{1_E} m_{2_E}}{\overline{\gamma_E}}\gamma_E \middle| \begin{matrix} 1-\alpha_{2_E}, 1-\alpha_{1_E} \\ m_{1_E}, m_{2_E} \end{matrix}\right) d\gamma_E. \end{aligned} \tag{4.33}$$

2. **SS case** Similarly, for the SS case, the SOP can be evaluated as shown in (4.34) by employing (2.21) and (2.24).

$$\begin{aligned} P_{\text{sec}} = \int_0^\infty \frac{\mathbb{C}_{SS}}{\gamma_E} G_{2,3}^{2,2}\left(\frac{m_{1_D} m_{2_D}}{\overline{\gamma_D}}(e^{R_s}\gamma_E + e^{R_s} - 1)\middle| \begin{matrix} , 1-\alpha_D, 1 \\ m_{1_D}, m_{2_D}, 0 \end{matrix}\right) \\ \times G_{1,2}^{2,1}\left(\frac{m_{1_E} m_{2_E}}{\overline{\gamma_E}}\gamma_E \middle| \begin{matrix} 1-\alpha_E \\ m_{1_E}, m_{2_E} \end{matrix}\right) d\gamma_E. \end{aligned} \tag{4.34}$$

4.4.2.3 Probability of Strictly Positive Secrecy Capacity (SPSC)

The probability of SPSC, denoted as P_{SPSC},is the probability that secrecy capacity remains positive, which can be calculated as [83]

$$
\begin{aligned}
P_{\text{SPSC}} &= \mathbb{P}\{C_s(\gamma_D, \gamma_E) > 0\}, \\
&= 1 - P_{\text{sec}}|_{(R_s=0)}.
\end{aligned}
\tag{4.35}
$$

4.4.3 Simulation Results

Several plots illustrate the ASC, SOP, and SPSC of the UAV-to-ground channel with shadowing in this section. To verify the analytical formulations in subsection 4.4.2, 10^6 realizations of fading channels are created for the Monte Carlo simulation.

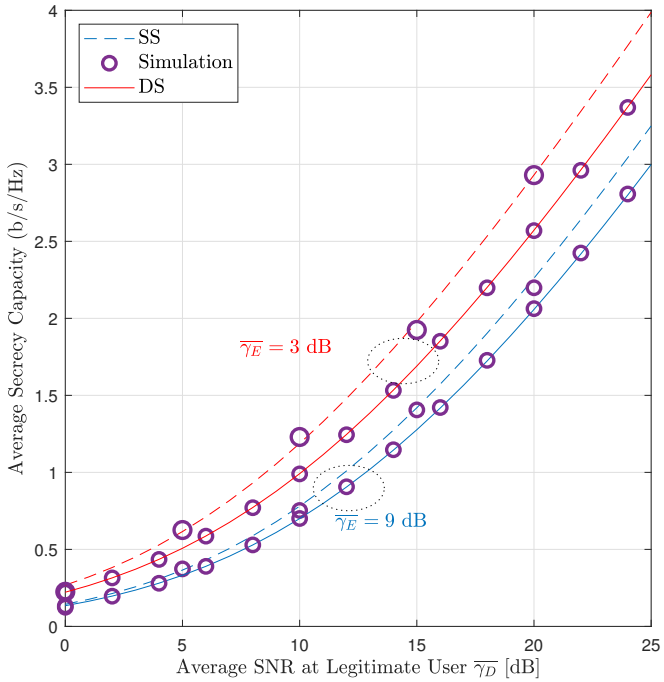

Figure 4.6: ASC over UAV-to-ground channel vs. $\overline{\gamma_D}$ for different values of $\overline{\gamma_E}$.

Figure 4.6 plots the ASC as a function of $\overline{\gamma_D}$, for $\overline{\gamma_E} = 3, 9$ dB. By comparison with the Monte Carlo simulations, the numerical analysis falls well within the confidence interval of the simulations. The channel's parameters are identical for both the intended and eavesdropper users ($m_1 = 1.1$, $m_2 = 1.4$, $\alpha_1 = 1.5$, $\alpha_2 = 2.5$). As anticipated, the performance in terms of ASC improves with increasing $\overline{\gamma_D}$ or decreasing $\overline{\gamma_E}$. Due to the

absence of one of the shadowing zones, it can be seen that a higher average secrecy capacity can be achieved under the SS case when compared to the DS one.

In Figure 4.7, we investigate the impact of varying the main channel's m_1 and α_1 on the ASC. The main channel experiences the following parameters: $\overline{\gamma_D} = 20$ dB, $m_2 = m_1 + 0.2$, $\alpha_2 = \alpha_1 + 0.6$. The channel's parameters for the eavesdropper user are $\overline{\gamma_E} = 2$ dB, $m_1 = 3.2$, $m_2 = 3.6$, $\alpha_1 = 1.8$, $\alpha_2 = 2.2$. It is clear from the graphs that as α_1 increases, the ASC monotonically declines due to increasing the shadowing effect of the channel. In contrast, as m_1 increases, the system performs better in terms of secrecy. This is because as m_1 increases, the channel's amplitude experiences less fluctuation.

In Figure 4.8, the SOP is plotted as a function of the ratio between $\overline{\gamma_D}$ and $\overline{\gamma_E}$ in dB. The main channel's parameters are selected to become ($m_1 = 1.3$, $m_2 = 1.5$, $\alpha_1 = 1.8$, $\alpha_2 = 2.3$). For the eavesdropper, the values are selected as ($m_1 = 1.1$, $m_2 = 1.4$, $\alpha_1 = 1.8$, $\alpha_2 = 2.5$). It is shown that a Monte Carlo simulation produces results that are very similar to the results obtained by the analytical formulae. The performance of SOP improves with increasing the ratio between $\overline{\gamma_D}$ and $\overline{\gamma_E}$. Additionally, it should be noted that the SS is more favorable for secrecy outage probability when compared to the DS scenario. In addition, smaller values of R_s can obtain a smaller SOP.

SPSC is plotted as a function of $\overline{\gamma_D}$ in dB for the DS case in Figure 4.9. It is shown that the results of the Monte Carlo simulation align with the mathematical analyses. The channel parameters are the same for both the intended user and eavesdropper ($m_2 = m_1 + 0.3$, $\alpha_1 = 1.5, \alpha_2 = 2.4$). SPSC is always non-zero, even if $\overline{\gamma_D} < \overline{\gamma_E}$ For fixed $\overline{\gamma_D}$, SPSC decreases as $\overline{\gamma_E}$ increases. Furthermore, as the intended user's channel fluctuation decreases (which is indicated by an increase in the value of m_{1_D}), SPSC increases for the fixed m_{1_E} of the eavesdropper.

In Figure 4.10, SPSC is depicted as a function of the ratio between $\overline{\gamma_D}$ and $\overline{\gamma_E}$ in dB and α_1 of the intended user's SS channel ($m_1 = 2.7$, $m_2 = 3$). The eavesdropper channel's parameters are ($m_1 = 1.7$, $m_2 = 1.9$, $\alpha_1 = 2.2$). SPSC monotonically increases as the ratio between $\overline{\gamma_D}$ and $\overline{\gamma_E}$ increases. As the channel experiences severe shadowing (which is indicated by an increase in α_1), SPSC decreases.

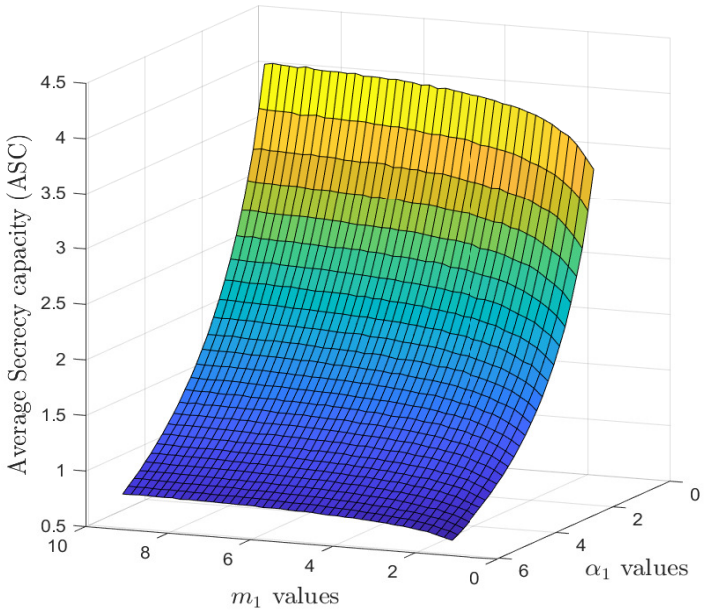

Figure 4.7: Effect of varying m_1 and α_1 of the intended user's channel (DS case) on ASC.

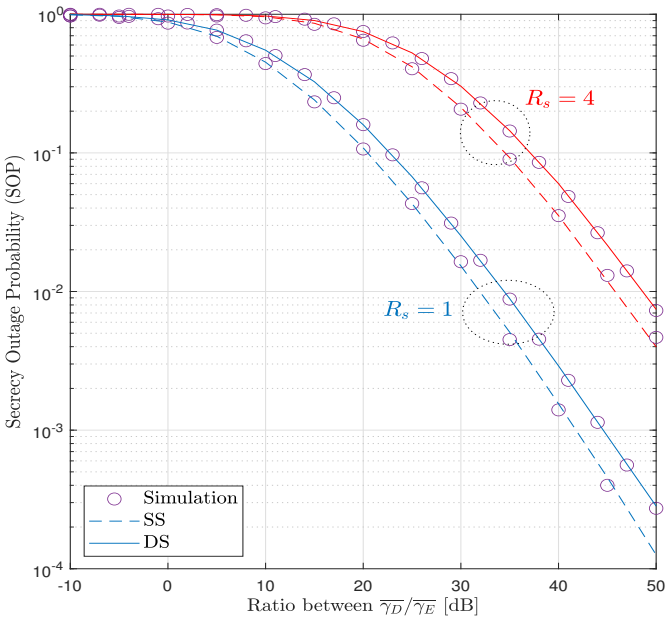

Figure 4.8: SOP over UAV-to-ground channel vs. the ratio between $\overline{\gamma_D}$ and $\overline{\gamma_E}$ in dB.

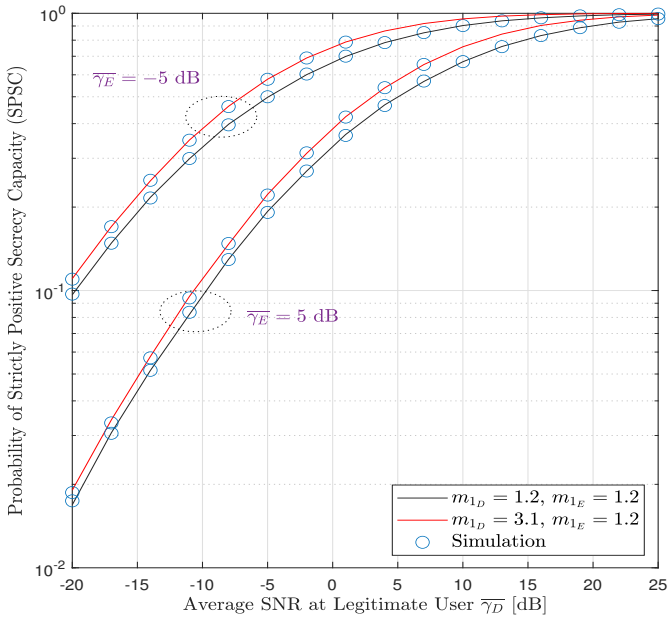

Figure 4.9: SPSC against the $\overline{\gamma_D}$ in dB for different m_1 and $\overline{\gamma_E}$ values (DS case).

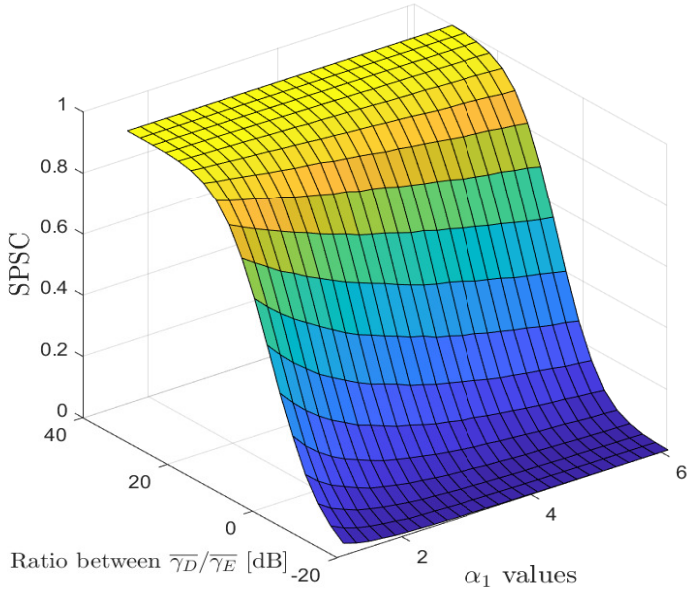

Figure 4.10: SPSC against the ratio between $\overline{\gamma_D}$ and $\overline{\gamma_E}$ in dB and α_1 (SS case).

4.5 Summary

This chapter focuses on a comprehensive analysis of various capacities of UAV-to-ground channels. Particularly, the average ergodic capacity in UAV-to-ground fading channels was assessed under various power adaptation strategies, yielding closed-form expressions. Additionally, the derivation of effective capacity expressions, utilizing the Gamma and Meijer G-functions within MATLAB, was accomplished. The validity of these theoretical results was confirmed through Monte-Carlo simulations.

Moreover, an exploration into the physical layer security of UAV-to-ground fading channels was conducted, emphasizing metrics such as ASC, SOP, and SPSC. From the results obtained, by increasing the average SNR of the main channel or lowering the average SNR of the eavesdropper channel, the security performance of the system under consideration can be enhanced. Additionally, numerical illustrations revealed the impact of channel parameters on ASC and SPSC.

In the next chapters, studies of communication systems incorporating practical features like multi-antenna Rx configurations under shadowed UAV-to-ground channels are presented in order to enhance communication performance and reliability in aerial-to-ground communication systems involving UAVs.

Chapter 5

On The Performance of Receiver Diversity Schemes

5.1 Introduction

Diversity-combining techniques are common techniques to improve system performance in fading channels [85]. In diversity, the same data streams are sent over independent fading paths. The fading of the resulting signal is minimized by combining these independent streams. Diversity can be realized in different domains: frequency, time, polarization, angle, or space diversity. In space diversity, multiple transmit or receive antennas are deployed in order to achieve multiple independent streams between the Tx and Rx. About one-half-wavelength of antenna separation is required between each antenna for independent fading to occur. In addition, receiver space diversity has gained considerable attention in previous research papers because it is realized without an increase in transmit signal power or bandwidth [49]. One of the receiver space diversity techniques is the MRC receiver, which can achieve diversity gain because it maximizes the achievable SNR at the combiner output [86]. Another diversity scheme is SC, which is simple to implement and therefore becomes an important option in complexity-constrained systems. [87].

Previous literature papers focused on the case of single-antenna receivers for the channel between UAV and ground. In [34, 35], the authors analyzed the system performance for the UAV-to-ground channels with a single receive antenna using the PDF and CDF of the received SNR. Moreover, the authors in [36] limited their focus to the ASER only.

Motivated by the performance of UAV communications with neither MRC nor SC schemes over shadowed fading channels that have not yet been investigated in the existing literature, this chapter is dedicated to analyzing the performance of both MRC and SC schemes over UAV-to-ground fading channels. The main contributions of this chapter are as follows:

- Based on MGF expressions of the received SNR, we provide a mathematical analysis to calculate the ABER, ASER, ergodic capacity, and outage probability of the shadowed UAV-to-ground fading channel for single and multiple receive antennas.
- Based on PDF and CDF expressions of the maximum received SNR, we provide a mathematical analysis for UAV-to-ground communications with SC receivers that yields closed-form expressions for the ABER, outage capacity, outage probability, and the average channel capacity.

This chapter is organized as follows: In Section 5.2, we study the performance of MRC receivers, accompanied by their numerical results, to illustrate their performance. In Section 5.3, the performance of SC receivers is analyzed, which is verified by numerical results to illustrate their performance. Finally, the chapter is summarized in Section 5.4.

5.2 Maximal-Ratio Combining Receiver

In this section, we evaluate the performance of the MRC receiver. In sub-section 5.2.1, the MRC system model is presented. In sub-section 5.2.2, the expressions for ABER, ergodic capacity, and outage probability are obtained. Numerical results are discussed in sub-section 5.2.3.

5.2.1 System Model

The system model consists of a single UAV equipped with a single transmit antenna. The Rx is equipped with N_r receive antennas. The received signal, y_l, at each antenna can be written as

$$y_l = h_l x + n_l, \tag{5.1}$$

where h_l is the channel coefficient between the Tx and the l^{th} antenna at Rx; $l \in [1 : N_r]$; and n_l represents the AWGN at the front end of the Rx with $\mathcal{CN}(\mathbf{0}, N_o)$ distribution. The expected value of the received SNR is given by

$$\overline{\gamma_l} = \mathbb{E}\{\gamma_l\} = \frac{E_b}{N_o}\mathbb{E}\{{h_l}^2\}, \tag{5.2}$$

where E_b denotes energy per bit and $\mathbb{E}\{.\}$ denotes expectation. The output of the receiver, denoted as z, can be expressed as

$$z = \sum_{l=1}^{N_r} {h_l}^* \times y_l. \tag{5.3}$$

The total SNR γ_t at the output of the MRC receiver can be expressed as [53]

$$\gamma_t = \sum_{l=1}^{N_r} \gamma_l, \tag{5.4}$$

where γ_l represents the SNR at each branch of the receiver. The MGF $\mathcal{M}_{\gamma_t}(s)\, of \gamma_t$ at the output of the MRC receiver can be evaluated as [53]

$$\mathcal{M}_{\gamma_t}(s) = \prod_{l=1}^{N_r} \mathcal{M}_{\gamma_l}(s). \tag{5.5}$$

1. **DS case:**

   Using (2.12), $\mathcal{M}_{\gamma_t}(s)$ of γ_t for the DS case can be written as

$$\mathcal{M}_{\gamma_t}(s) = \left[\mathbb{S}_{DS} G_{3,2}^{2,3}\left(\frac{-m_1 m_2}{\overline{\gamma} s}\middle| \begin{matrix} 1, 1-\alpha_2, 1-\alpha_1 \\ m_1, m_2 \end{matrix}\right)\right]^{N_r}. \tag{5.6}$$

2. **SS case:**

   Using (2.25), $\mathcal{M}_{\gamma_t}(s)$ of γ_t for the SS case can be expressed as

$$\mathcal{M}_{\gamma_t}(s) = \left[\mathbb{S}_{SS} G_{2,2}^{2,2}\left(\frac{-m_1 m_2}{\overline{\gamma} s}\middle| \begin{matrix} 1, 1-\alpha \\ m_1, m_2 \end{matrix}\right)\right]^{N_r}. \tag{5.7}$$

5.2.2 Performance Evaluation

In this sub-section, we provide a theoretical analysis of the performance of the MRC receiver in terms of ABER, ergodic capacity, outage probability, and ASER based on the MGF expressions.

5.2.2.1 Average Bit Error Rate (ABER)

Using the MGF approach, the ABER, P_{be}, for the MRC receiver using the BPSK modulation scheme can be expressed as [53]

$$P_{\text{be}} = \frac{1}{\pi} \int_0^{\frac{\pi}{2}} \left[\mathcal{M}_{\gamma_l} \left(\frac{-1}{\sin^2 \Phi} \right) \right]^{N_r} d\Phi. \tag{5.8}$$

1. **DS case:**

   For the DS case, P_{be} can be evaluated as

$$P_{\text{be}} = \frac{{\mathbb{S}_{DS}}^{N_r}}{\pi} \int_0^{\frac{\pi}{2}} \left[G_{3,2}^{2,3} \left(\frac{m_1 m_2 \sin^2 \Phi}{\overline{\gamma}} \middle| \begin{matrix} 1, 1-\alpha_2, 1-\alpha_1 \\ m_1, m_2 \end{matrix} \right) \right]^{N_r} d\Phi. \tag{5.9}$$

2. **SS case:**

   Similarly, for the SS case, P_{be} can be evaluated as

$$P_{\text{be}} = \frac{{\mathbb{S}_{SS}}^{N_r}}{\pi} \int_0^{\frac{\pi}{2}} \left[G_{2,2}^{2,2} \left(\frac{m_1 m_2 \sin^2 \Phi}{\overline{\gamma}} \middle| \begin{matrix} 1, 1-\alpha \\ m_1, m_2 \end{matrix} \right) \right]^{N_r} d\Phi. \tag{5.10}$$

5.2.2.2 Ergodic Capacity

Using the MGF approach, the ergodic capacity, C_{ER}, can be expressed as [88, 89]

$$C_{\text{ER}} = \frac{\mathbb{B}}{\log(2)} \int_0^{\infty} \text{Ei}(-s) \frac{\partial}{\partial s} \left[\mathcal{M}_{\gamma_t}(s) \right] ds, \tag{5.11}$$

where Ei(.) is the exponential integral function defined in [90,eq. (5.1.2)].

1. **DS case:**

   With the help of (A.10), $\frac{\partial}{\partial s}\left[\mathcal{M}_{\gamma_t}(s)\right]$ can be evaluated for the DS scenario as

$$\begin{aligned}\frac{\partial}{\partial s}\left[\mathcal{M}_{\gamma_t}(s)\right] = \frac{-N_r {\mathbb{S}_{DS}}^{N_r}}{s} G_{4,4}^{2,4}\left(\frac{-m_1 m_2}{\overline{\gamma} s}\middle| \begin{matrix} 0,1,1-\alpha_2,1-\alpha_1 \\ m_1,m_2,1 \end{matrix}\right) \\ \times\left[G_{3,2}^{2,3}\left(\frac{-m_1 m_2}{\overline{\gamma} s}\middle| \begin{matrix} 1,1-\alpha_2,1-\alpha_1 \\ m_1,m_2 \end{matrix}\right)\right]^{N_r-1}.\end{aligned} \tag{5.12}$$

2. **SS case:**

   Similarly, for the SS case, , $\frac{\partial}{\partial s}\left[\mathcal{M}_{\gamma_t}(s)\right]$ can be evaluated as

$$\begin{aligned}\frac{\partial}{\partial s}\left[\mathcal{M}_{\gamma_t}(s)\right] = \frac{-N_r {\mathbb{S}_{SS}}^{N_r}}{s} G_{3,3}^{2,3}\left(\frac{-m_1 m_2}{\overline{\gamma} s}\middle| \begin{matrix} 0,1,1-\alpha \\ m_1,m_2,1 \end{matrix}\right) \\ \times\left[G_{2,2}^{2,2}\left(\frac{-m_1 m_2}{\overline{\gamma} s}\middle| \begin{matrix} 1,1-\alpha \\ m_1,m_2 \end{matrix}\right)\right]^{N_r-1}.\end{aligned} \tag{5.13}$$

5.2.2.3 Outage Probability

The outage probability, P_{out}, which indicates that γ_t falls below a certain threshold value γ_{th}, can be evaluated using the MGF approach as [53]

$$\begin{aligned}P_{\text{out}} &= P(\gamma_t < \gamma_{th}) \\ &= \frac{1}{2\pi i}\int_{\sigma-i\infty}^{\sigma+i\infty} \frac{\mathcal{M}_{\gamma_t}(-s)}{s} e^{\gamma_{th} s} ds,\end{aligned} \tag{5.14}$$

where σ is chosen in the region of convergence of the integral in the complex s plane and $i = \sqrt{-1}$.

1. **DS case:**

   P_{out} can be evaluated for the DS case as

$$P_{\text{out}} = \frac{\mathbb{S}_{DS}{}^{N_r}}{2\pi i} \int_{1-i\infty}^{1+i\infty} \left[G_{3,2}^{2,3} \left(\frac{m_1 m_2}{\overline{\gamma} s} \middle| \begin{matrix} 1, 1-\alpha_2, 1-\alpha_1 \\ m_1, m_2 \end{matrix} \right) \right]^{N_r} \frac{e^{\gamma_{th} s}}{s} ds, \tag{5.15}$$

where $\sigma = 1$ based on the region of convergence of the MGF.

2. **SS case:**

Similarly, for the SS case, P_{out} can be expressed as

$$P_{\text{out}} = \frac{\mathbb{S}_{SS}{}^{N_r}}{2\pi i} \int_{1-i\infty}^{1+i\infty} \left[G_{2,2}^{2,2} \left(\frac{m_1 m_2}{\overline{\gamma} s} \middle| \begin{matrix} 1, 1-\alpha \\ m_1, m_2 \end{matrix} \right) \right]^{N_r} \frac{e^{\gamma_{th} s}}{s} ds. \tag{5.16}$$

5.2.2.4 Average Symbol Error Rate (ASER)

1. **MPSK:**

Using the MGF approach, the ASER, P_{se}, for the MRC receiver using MPSK modulation schemes can be expressed as [53]

$$P_{\text{se}} = \frac{1}{\pi} \int_0^{\frac{(M-1)\pi}{M}} \left[\mathcal{M}_{\gamma_l} \left(\frac{-\sin^2(\pi/M)}{\sin^2 \Phi} \right) \right]^{N_r} d\Phi, \tag{5.17}$$

where M is the modulation order.

(a) **DS case:**

For the DS case, P_{se} can be evaluated as

$$P_{\text{se}} = \frac{\mathbb{S}_{DS}{}^{N_r}}{\pi} \int_0^{\frac{(M-1)\pi}{M}} \left[G_{3,2}^{2,3} \left(\frac{m_1 m_2 \sin^2 \Phi}{\overline{\gamma} \sin^2(\pi/M)} \middle| \begin{matrix} 1, 1-\alpha_2, 1-\alpha_1 \\ m_1, m_2 \end{matrix} \right) \right]^{N_r} d\Phi. \tag{5.18}$$

(b) **SS case:**

Similarly, for the SS case, P_{se} can be computed as

$$P_{\text{se}} = \frac{\mathbb{S}_{SS}{}^{N_r}}{\pi} \int_0^{\frac{(M-1)\pi}{M}} \left[G_{2,2}^{2,2} \left(\frac{m_1 m_2 \sin^2 \Phi}{\overline{\gamma} \sin^2(\pi/M)} \middle| \begin{matrix} 1, 1-\alpha \\ m_1, m_2 \end{matrix} \right) \right]^{N_r} d\Phi. \tag{5.19}$$

2. *M*-QAM:

Using the MGF approach, the ASER, P_{se}, for the MRC receiver using M-QAM schemes can be expressed as [53]

$$\begin{aligned} P_{\text{se}} =& \frac{4}{\pi}\left(1-\frac{1}{\sqrt{M}}\right)\int_0^{\frac{\pi}{2}}\left[\mathcal{M}_{\gamma_l}\left(\frac{-3}{2(M-1)\sin^2\Phi}\right)\right]^{N_r} d\Phi \\ & -\frac{4}{\pi}\left(1-\frac{1}{\sqrt{M}}\right)^2\int_0^{\frac{\pi}{4}}\left[\mathcal{M}_{\gamma_l}\left(\frac{-3}{2(M-1)\sin^2\Phi}\right)\right]^{N_r} d\Phi, \end{aligned} \tag{5.20}$$

where M is the modulation order.

5.2.3 Numerical Results

In this section, we present some plots to illustrate the ABER, channel capacity, and outage probability of MRC receivers operating in the UAV-to-ground channel.

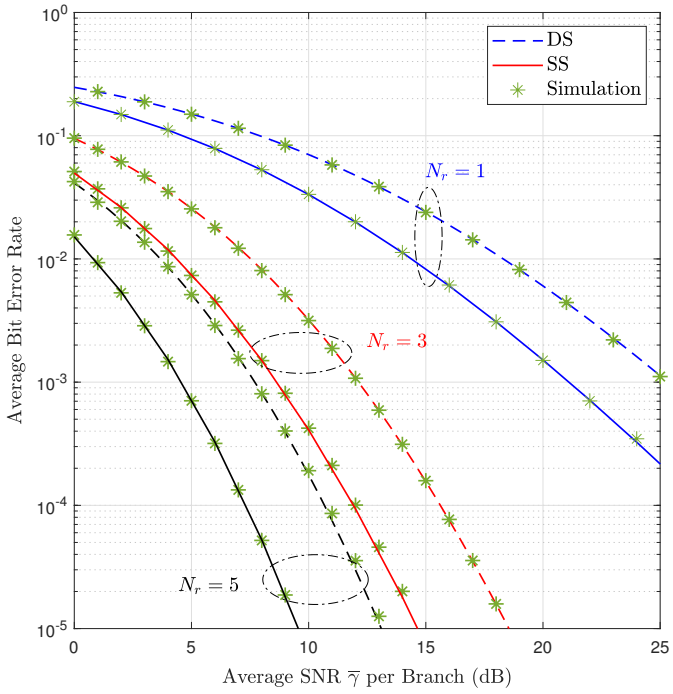

Figure 5.1: ABER performance for MRC receiver using BPSK modulation.

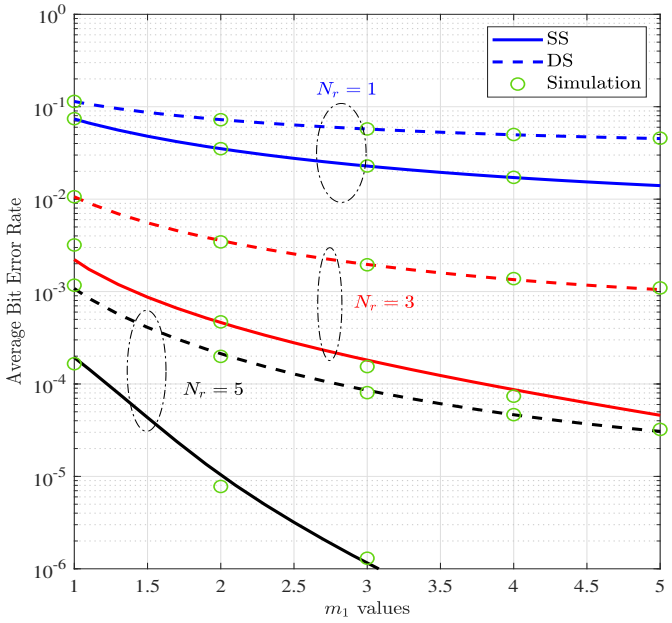

Figure 5.2: ABER performance for MRC receiver under the effect of varying m_1.

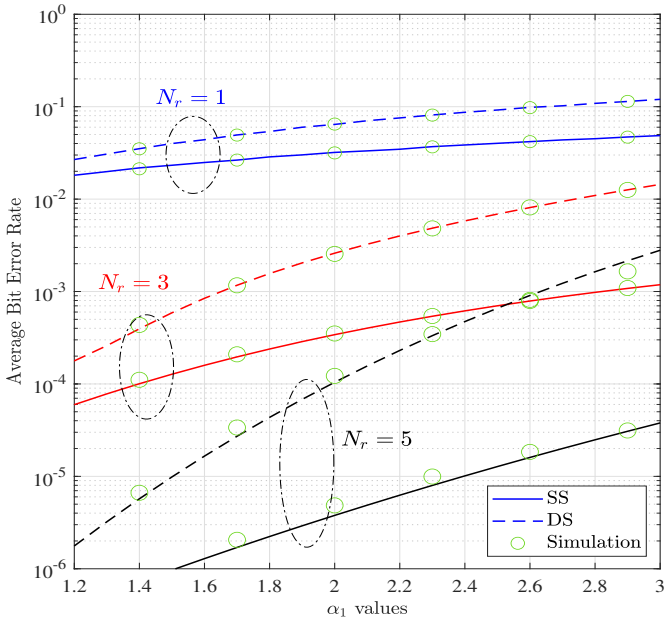

Figure 5.3: ABER performance for MRC receiver under the effect of varying α_1.

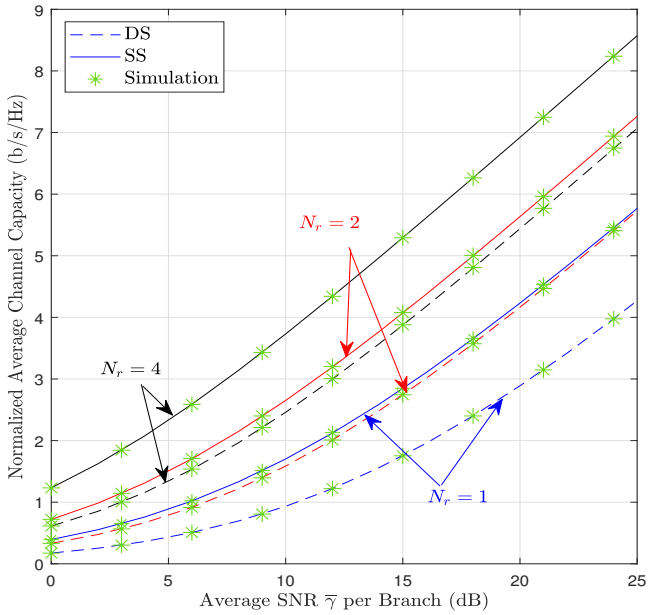

Figure 5.4: Normalized capacity versus average SNR per link for different N_r.

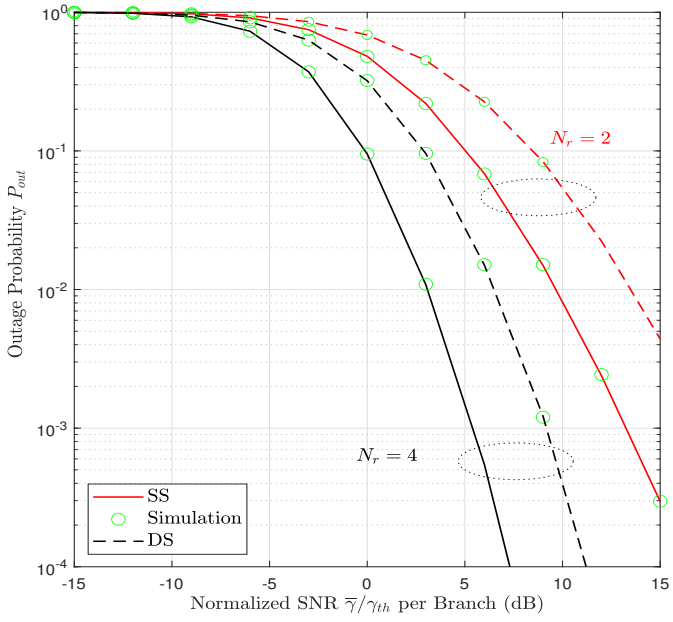

Figure 5.5: Outage probability versus normalized SNR per link $\overline{\gamma}/\gamma_{th}$ for different N_r.

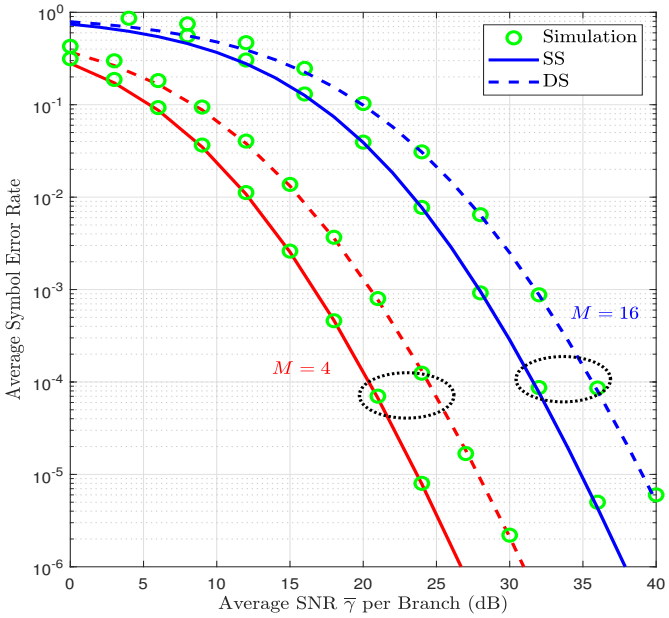

Figure 5.6: ASER for different MPSK schemes ($N_r = 2$).

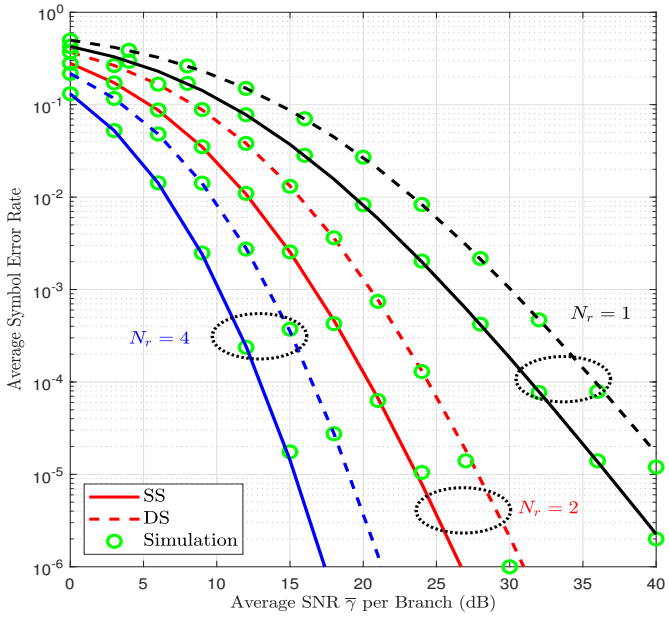

Figure 5.7: ASER performance for MRC receiver using 4-QAM modulation different N_r.

In Figure 5.1, we show the ABER as a function of SNR per link for the BPSK scheme while varying the number of the receive antennas N_r. The channel parameters ($m_1 = \alpha_1 = 2.1$, $m_2 = m_1 + 0.3$, and $\alpha_2 = \alpha_1 + 0.3$) were selected to match those presented in [34]. The theoretical curves were evaluated using numerical integration of (5.9) for the DS case and (5.10) for the SS one. For N_r= 1, the ABER curves that we obtain both analytically and via Monte Carlo simulation match those curves produced in [34], which provides a benchmark for the rest of our analysis. For N_r= 3 and N_r= 5, the ABER curves produced through our analysis fall within the confidence intervals of those produced via Monte Carlo simulation, which in turn validates our analysis.

Figure 5.2 shows the ABER performance of the BPSK scheme as a function of m_1 values, ($1 \leq m_1 \leq 5$), while varying the number of the receive antennas, N_r. $\alpha_1 = 1.8$, $m_2 = m_1 + 0.5$, and $\alpha_2 = \alpha_1 + 0.2$ with $\overline{\gamma} = 10$ dB. It is clear that as m_1 increases, the performance improves due to decreasing the multipath effect of the channel. Figure 5.3 plots the ABER performance of the BPSK scheme as a function of α_1 values, ($1.2 \leq \alpha_1 \leq 3$), with varying the number of the receive antennas, N_r. $m_1 = 2.3$, $m_2 = m_1 + 0.2$, and $\alpha_2 = \alpha_1 + 0.2$ with $\overline{\gamma} = 10$ dB. It is clear that as α_1 increases, the performance degrades due to increasing the shadowing effect of the channel. From both Figure 5.2 and Figure 5.3, we can see that as N_r increases, the gap in performance between SS and DS becomes more noticeable. For example, in Fig. 5.2, when $m_1 = 3$, the ABER of SS is 10^2 times better than the ABER of DS for N_r= 5. Whereas for N_r= 1, the ABER of SS is roughly half the ABER of the DS case. This is because DS increases the probability that multiple links encounter deep fading simultaneously. Thus reducing the effective diversity of the channel.

Figure 5.4 displays the normalized capacity, $C_{\text{ER}}/\mathbb{B}$, of the MRC receiver as a function of the average SNR value in dB for different values of the receive antennas N_r with $m_1 = 1.5, m_2 = 1.8, \alpha_1 = 3.5$, and $\alpha_2 = 3.6$. The parameters were selected to match those for the SISO channel in [34]. By applying numerical integration of (5.11), the theoretical curves were developed, which aligned with Monte Carlo simulation results. As expected, it is noted from the above results that the performance in the DS case is worse than in the SS one. This is because shadowing exists in two scattering regions around the Tx and Rx in the DS scenario. Whereas in the SS one, shadowing is present in only one of the two regions.

In Figure 5.5, the outage probability is plotted as a function of the normalized SNR

value $\overline{\gamma}/\gamma_{th}$ in dB for different values of the receive antenna N_r with $m_1 = \alpha_1 = 2.1$, $m_2 = m_1 + 0.3$, and $\alpha_2 = \alpha_1 + 0.3$. By numerically integrating (5.15) for the DS case and (5.16) for the SS one, the theoretical curves of the outage probability were evaluated and validated by Monte Carlo simulation. All of these numerical integrations were performed using MATLAB's built-in Meijer G-function.

In Figure 5.6, the ASER is plotted as a function of SNR per link for different M values of the MPSK schemes with N_r= 2. The channel parameters are $m_1 = \alpha_1 = 2.1$ and $m_2 = \alpha_2 = 2.4$. The numerical integrations of (5.18) for the DS case and (5.19) for the SS one were used to evaluate the theoretical curves. As we can see, the curves generated by our analysis are consistent with those generated by Monte Carlo simulation, which supports the validity of our study.

In Figure 5.7, the ASER is plotted as a function of SNR per link for 4-QAM for different N_r. The channel parameters are $m_1 = \alpha_1 = 2.1$ and $m_2 = \alpha_2 = 2.4$. By plugging the MGF expressions into (5.20), we can obtain theoretical curves for the 4-QAM scheme. As we can see, our analysis's curves are validated by the curves obtained through Monte Carlo simulation.

5.3 Selection Combining Receiver

This section is dedicated to analyzing the performance of the SC receiver. In sub-section 5.3.1, statistics of the maximum SNR of the UAV-to-ground channel are presented. In sub-section 5.3.2, the theoretical expressions for ABER, ergodic capacity, outage capacity, and outage probability are obtained. Numerical results are discussed in sub-section 5.3.3.

5.3.1 Statistics of The Maximum SNR of UAV-To-Ground Channel

In SC, the Rx is equipped with N_r antennas, and it selects the branch with the highest SNR of all antenna outputs. Assuming that the fading on each link is independent and identically distributed, the CDF of the maximum SNR, $\gamma_m = \max(\gamma_1, \gamma_2, \ldots, \gamma_{N_r})$, can be expressed as [53]

$$F_{\gamma_m}(\gamma) = \prod_{l=1}^{N_r} F_{\gamma_l}(\gamma). \tag{5.21}$$

1. **DS case:**

   For the DS case, the CDF of the maximum can be written as

$$F_{\gamma_m}(\gamma) = \left[\mathbb{S}_{DS} G_{3,3}^{2,3}\left(\frac{m_1 m_2}{\overline{\gamma}}\gamma \middle| \begin{matrix} 1-\alpha_2, 1-\alpha_1, 1 \\ m_1, m_2, 0 \end{matrix}\right)\right]^{N_r}. \tag{5.22}$$

   The PDF of the maximum SNR γ_m in the DS case can be evaluated as

$$\begin{aligned} f_{\gamma_m}(\gamma) &= \frac{d}{d\gamma}\left(F_{\gamma_m}(\gamma)\right), \\ &= \frac{[\mathbb{S}_{DS}]^{N_r}}{\gamma}\left[G_{3,3}^{2,3}\left(\frac{m_1 m_2}{\overline{\gamma}}\gamma \middle| \begin{matrix} 1-\alpha_2, 1-\alpha_1, 1 \\ m_1, m_2, 0 \end{matrix}\right)\right]^{N_r-1} \\ &\times G_{2,2}^{2,2}\left(\frac{m_1 m_2}{\overline{\gamma}}\gamma \middle| \begin{matrix} 1-\alpha_2, 1-\alpha_1 \\ m_1, m_2 \end{matrix}\right). \end{aligned} \tag{5.23}$$

2. **SS case:**

   Similarly, For the SS case, the CDF of the maximum SNR γ_m can be written as

$$F_{\gamma_m}(\gamma) = \left[\mathbb{S}_{SS} G_{2,3}^{2,2}\left(\frac{m_1 m_2}{\overline{\gamma}}\gamma \middle| \begin{matrix} 1-\alpha_1, 1 \\ m_1, m_2, 0 \end{matrix}\right)\right]^{N_r}. \tag{5.24}$$

   The PDF of the maximum SNR γ_m in the SS case can be evaluated as

$$\begin{aligned} f_{\gamma_m}(\gamma) &= \frac{d}{d\gamma}\left(F_{\gamma_m}(\gamma)\right), \\ &= \frac{[\mathbb{S}_{SS}]^{N_r}}{\gamma}\left[G_{2,3}^{2,2}\left(\frac{m_1 m_2}{\overline{\gamma}}\gamma \middle| \begin{matrix} 1-\alpha, 1 \\ m_1, m_2, 0 \end{matrix}\right)\right]^{N_r-1} \\ &\times G_{1,2}^{2,1}\left(\frac{m_1 m_2}{\overline{\gamma}}\gamma \middle| \begin{matrix} 1-\alpha \\ m_1, m_2 \end{matrix}\right). \end{aligned} \tag{5.25}$$

5.3.2 Performance Analysis of the SC Scheme

In this section, we provide a theoretical analysis of the performance of the SC receiver in terms of ABER, ergodic capacity, outage probability, and outage capacity based on the PDF and CDF of the maximum SNR expressions.

5.3.2.1 Outage Probability

The outage probability, P_{out}, indicates that the probability of the instantaneous SNR at the output of the combiner falls below the predetermined threshold, γ_{th}, which can be expressed as [91]

$$\begin{aligned} P_{\text{out}} &= \mathbb{P}(\gamma_m < \gamma_{th}), \\ &= F_{\gamma_m}(\gamma_{th}). \end{aligned} \tag{5.26}$$

5.3.2.2 Ergodic Capacity

The ergodic capacity, C_{ER}, of the SC Rx can be evaluated as

$$C_{\text{ER}} = \frac{\mathbb{B}}{\ln(2)} \int_0^{\infty} \ln(1+\gamma) f_{\gamma_m}(\gamma)\, d\gamma. \tag{5.27}$$

1. **DS case:**

   For the dual-branch case, if we write $\ln(1+\gamma) = G_{2,2}^{1,2}\left(\gamma \middle| \begin{matrix} 1,1 \\ 1,0 \end{matrix}\right)$ as shown in (A.4), the integration in (5.27) involves three Meijer G-functions, and with the help of (A.15), that integration can be expressed in terms of the bivariate Meijer G-function as

$$\begin{aligned} C_{\text{ER}} &= \frac{\mathbb{B}[\mathbb{S}_{DS}]^2}{\ln(2)} \\ &\times G_{2,2:3,3:2,2}^{2,1:2,3:2,2}\left(\frac{m_1 m_2}{\overline{\gamma}}, \frac{m_1 m_2}{\overline{\gamma}} \middle| \begin{matrix} 0,1 \\ 0,0 \end{matrix} \middle| \begin{matrix} 1-\alpha_2, 1-\alpha_1, 1 \\ m_1, m_2, 0 \end{matrix} \middle| \begin{matrix} 1-\alpha_2, 1-\alpha_1 \\ m_1, m_2 \end{matrix}\right). \end{aligned} \tag{5.28}$$

2. **SS case:**

   Similarly, C_{ER} for the SS case can be expressed as

$$C_{\text{ER}} = \frac{\mathbb{B}[\mathbb{S}_{SS}]^2}{\ln(2)} G_{2,2:2,3:1,2}^{2,1:2,2:2,1}\left(\frac{m_1 m_2}{\overline{\gamma}}, \frac{m_1 m_2}{\overline{\gamma}} \middle| \begin{matrix} 0,1 \\ 0,0 \end{matrix} \middle| \begin{matrix} 1-\alpha, 1 \\ m_1, m_2, 0 \end{matrix} \middle| \begin{matrix} 1-\alpha \\ m_1, m_2 \end{matrix}\right). \tag{5.29}$$

5.3.2.3 Outage Capacity

The outage capacity, C_{out}, which is defined as the probability that the instantaneous capacity C_{ER}; is less than a certain threshold value, Φ, can be expressed as [92]

$$\begin{aligned} C_{out} &= \mathbb{P}(0 < C_{\mathrm{ER}} < \Phi) \\ &= F_{\gamma_m}\left(2^{\frac{\Phi}{B}} - 1\right) \end{aligned} \tag{5.30}$$

5.3.2.4 Average Bit Error Rate

Using the CDF-based approach, the ABER can be expressed as [56]

$$P_{\mathrm{be}} = \frac{\kappa^{\beta}}{2\Gamma(\beta)} \int_0^{\infty} \gamma^{\beta-1} e^{-\kappa\gamma} F_{\gamma_m}(\gamma)\, d\gamma, \tag{5.31}$$

where $(\kappa, \beta) = (1, 0.5)$ for BPSK and $(\kappa, \beta) = (0.5, 0.5)$ coherent BFSK, respectively. Using the Taylor expansion of the exponential function [93], (5.31) can be rewritten as

$$P_{\mathrm{be}} = \frac{\kappa^{\beta}}{2\Gamma(\beta)} \sum_{n=0}^{\infty} \frac{(-\kappa)^n}{n!} \int_0^{\infty} \gamma^{\beta+n-1} F_{\gamma_m}(\gamma)\, d\gamma. \tag{5.32}$$

1. **DS case:**

   For the dual-branch case, with the help of (A.12), (5.32) for the DS case can be evaluated as

$$\begin{aligned} P_{\mathrm{be}} =& \frac{[\mathbb{S}_{DS}]^2 \kappa^{\beta}}{2\Gamma(\beta)} \sum_{n=0}^{\infty} \frac{(-\kappa)^n}{n!} \left(\frac{m_1 m_2}{\overline{\gamma}}\right)^{-(\beta+n)} \times \\ & G_{6,6}^{5,5}\left(1 \middle| \begin{matrix} 1-\alpha_2, 1-\alpha_1, 1, 1-(\beta+n)-m_1, 1-(\beta+n)-m_2, 1-(\beta+n) \\ m_1, m_2, -(\beta+n)+\alpha_1, -(\beta+n)+\alpha_2, -(\beta+n), 0 \end{matrix}\right). \end{aligned} \tag{5.33}$$

2. **SS case:**

Similarly, the ABER for the SS case can be expressed as:

$$P_{\text{be}} = \frac{[\mathbb{S}_{SS}]^2 \kappa^{\beta}}{2\Gamma(\beta)} \sum_{n=0}^{\infty} \frac{(-\kappa)^n}{n!} \left(\frac{m_1 m_2}{\overline{\gamma}}\right)^{-(\beta+n)} \times G_{5,5}^{4,4}\left(1 \middle| \begin{matrix} 1-\alpha, 1, 1-(\beta+n)-m_1, 1-(\beta+n)-m_2, 1-(\beta+n) \\ m_1, m_2, -(\beta+n)+\alpha, -(\beta+n), 0 \end{matrix}\right). \tag{5.34}$$

5.3.3 Simulation Results

In this section, we present some plots that illustrate the performance of the SC receiver in UAV-to-ground channels with shadowing. For the Monte Carlo simulation, 10^6 realizations of fading channels are generated to validate the analytical expressions in the previous subsection.

In Figure 5.8, the outage probability is plotted vs. the average SNR per branch for different values of m_1, and α_1. γ_{th} is selected to become 0 dB. $\alpha_2 = \alpha_1 + 0.3$, and $m_2 = m_1 + 0.3$. The outage probability declines by employing the SC receiver due to the diversity gain by increasing the number of receive antennas N_r. Moreover, the outage probability degrades as m_1 increases or α_1 decreases. This is because increasing m_1 corresponds to less fluctuation in the received signal. Whereas decreasing α_1 corresponds to a degraded effect of the shadowing effect in the UAV channel.

In Figure 5.9, the probability of outage capacity is plotted vs. the normalized threshold value ($\frac{\Phi}{\mathbb{B}}$) in dB. The fading channel parameters were selected to become ($m_1 = 1.1$, $m_2 = 1.4$, $\alpha_1 = 1.5$ and $\alpha_2 = 2.5$). Increasing N_r degrades the probability of outage capacity.

In Figure 5.10, the normalized average channel capacity, $C_{\text{ER}}/\mathbb{B}$, is plotted vs. the average SNR per branch for different values of N_r. The fading channel parameters were selected to become ($m_1 = 1.5$, $m_2 = 1.8$, $\alpha_1 = 3.5$, and $\alpha_2 = 3.6$). The parameters were selected to match those for the SISO channel in [34]. The normalized average channel capacity curves for $N_r = 1$ precisely match those curves produced in [34], which validates our simulation results. The normalized average ergodic capacity increases as N_r increases. It can be noticed that the SS case achieves better performance than the DS one.

In Figures 5.11 and 5.12, the ABER is plotted vs. the average SNR per branch for different values of N_r using BPSK and BFSK modulations, respectively. The fading channel

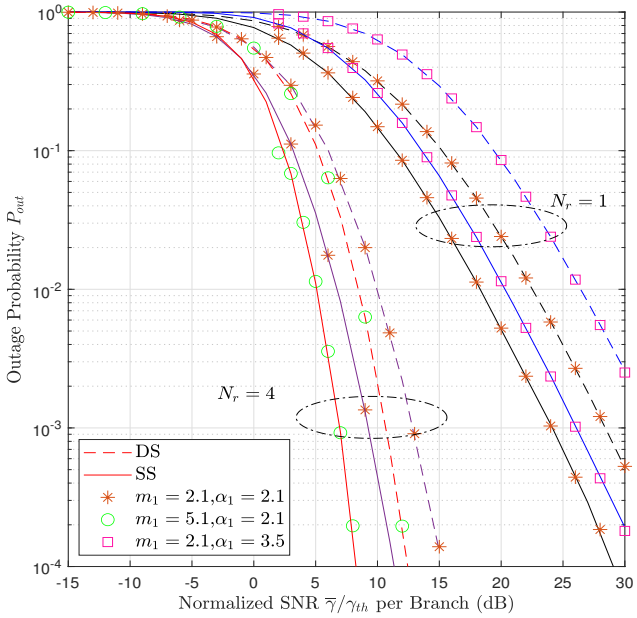

Figure 5.8: Outage probability vs. Normalized SNR for different m_1, α_1, N_r and $\gamma_{th} = 0$ dB

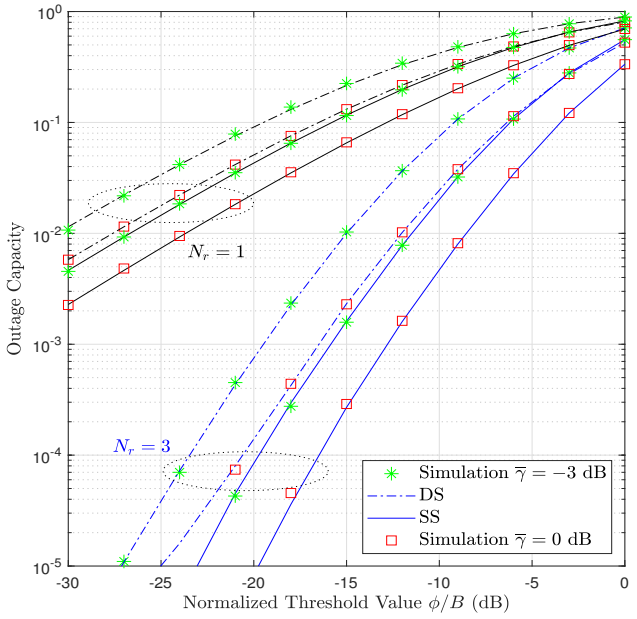

Figure 5.9: Outage capacity vs. normalized threshold value for different N_r and $\overline{\gamma}$.

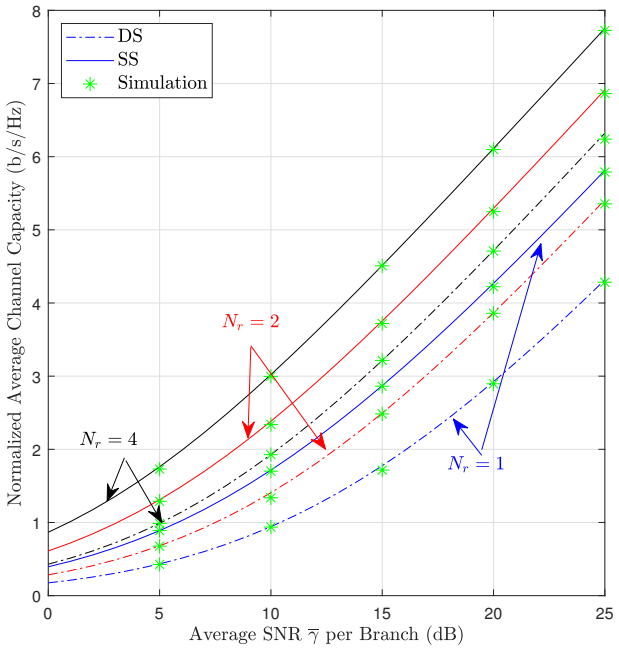

Figure 5.10: Normalized average channel capacity vs. average SNR $\overline{\gamma}$ for different N_r.

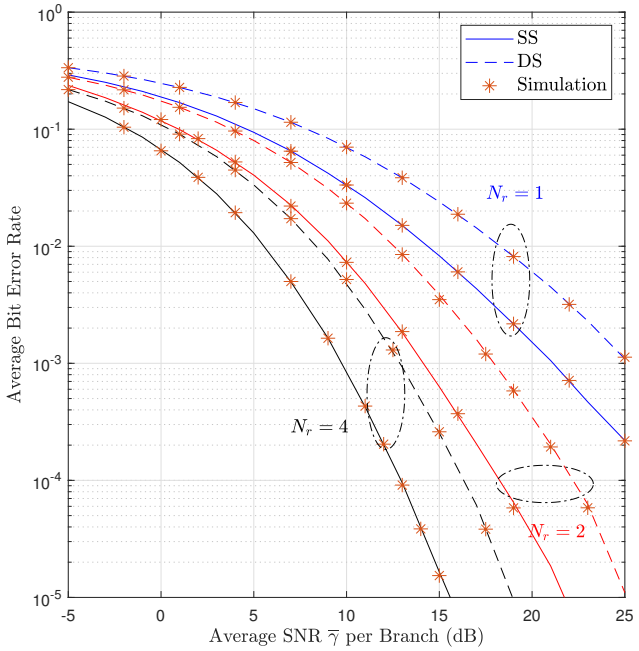

Figure 5.11: ABER vs. average SNR $\overline{\gamma}$ for different N_r (BPSK case).

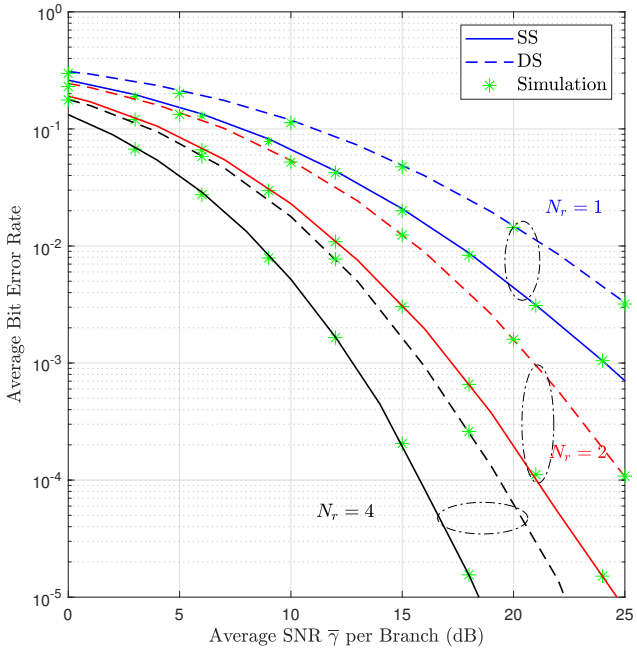

Figure 5.12: ABER vs. average SNR $\overline{\gamma}$ for different N_r (BFSK case).

parameters were selected to become ($m_1 = \alpha_1 = 2.1$ and $m_2 = \alpha_2 = 2.4$). The reason behind this selection of parameters is to match those presented in [34] for the SISO channel using BPSK. The ABER curves for N_r= 1 precisely match those curves produced in [34], which validates our simulation results. We can see from our results that the performance in the DS case is worse than in the SS one, which is to be expected. This is because shadowing exists in two scattering regions around the Tx and Rx in the DS scenario. Whereas in the SS one, shadowing is present in only one of the two regions.

5.4 Summary

In this chapter, we derived open-form expressions for the ABER, channel capacity, outage probability, and ASER of UAV-to-ground communication systems employing MRC receivers. These expressions were obtained using the MGF of the PDF of the SNR. Since closed-form expressions are mathematically intractable, we used numeral integration to obtain our theoretical plots. Through Monte Carlo simulations, we verified our theoretical findings, which can be easily evaluated numerically. After that, the performance of

the SC receiver over UAV-to-ground channel models with shadowing was studied. Based on the PDF and CDF expressions, mathematical expressions for the outage probability, outage capacity, average channel capacity, and ABER expressions are developed. The results demonstrated that both MRC and SC diversity reception can enhance system performance.

Chapter 6

Interference-Limited Systems over UAV-to-Ground Channels

In numerous wireless communication systems, co-channel interference often proves more impactful on performance than front-end Gaussian noise [94]. Consequently, the SIR stands out as a pivotal performance metric for evaluations in such scenarios. The outage probability in the presence of co-channel interference for Rayleigh channels was presented in [95]. The impact of co-channel interference on the outage probability as well as average error rates within Nakagami-m fading channels has been studied in [96] and [94], respectively. In exploring outage probability within interference-limited systems, research works such as [97] and [98] have considered extended generalized-K fading channels and a range of generalized fading channels, respectively.

In novel wireless systems involving UAVs, interference can occur both with terrestrial communications and among the UAVs themselves [99]. While several prior studies have examined UAV communications' performance amidst interference [100], such as the investigation into interference between UAVs and terrestrial networks and the focus on coverage area maximization, throughput maximization, and resource allocation in multi-UAV networks as explored in [101–103], these works predominantly assumed line-of-sight signals between ground users and UAVs, which may not be reliable, particularly in urban settings.

To the best of our knowledge, the outage probability of shadowed UAV-to-ground communications in the presence of co-channel interference under realistic channel models, as validated by empirical measurements in [34], remains unexplored in the existing literature.

Addressing this gap, this chapter delves into an interference-limited wireless communication system operating over UAV-to-ground links with shadowing fading channels, where outage probability serves as a crucial metric for characterizing such systems. The main contributions of this chapter can be summarized as follows:

- Novel closed-form expressions for the PDF, CDF, and MGF of the SIR are derived, enabling the evaluation of the outage probability in interference-limited systems.
- Moreover, we derive the asymptotic expressions for the outage probability obtained earlier into simpler elementary functions using Meijer G-function expansion, at high SIR values.
- Additionally, these expressions are then verified by numerical simulations, showcasing how the outage probability is affected by the shadowing and multipath parameters, in order to validate our analytical findings.

This chapter is structured as follows: In Section 6.1, a performance evaluation analysis of SIR is derived. Section 6.2 provides the asymptotic expressions for the outage probability. Section 6.3 discusses simulation results. Lastly, Section 6.4 provides the concluding remarks for this chapter.

6.1 Performance Evaluation

6.1.1 DS-DS Case

In the system under consideration, as shown in Figure 6.1, both the desired signal and the interfering one undergo fading characterized by the DS scenario. The instantaneous received signal power at the desired destination can be expressed as [36]

$$P = P_t d^{-\eta} |h|^2, \tag{6.1}$$

where P_t denotes the transmission power, d is the overall propagation distance, and η is the path-loss exponent. In this case, the average received signal power, ω, can be computed as [36]

$$\omega = P_t d^{-\eta} \mathbb{E}\{|h|^2\}. \tag{6.2}$$

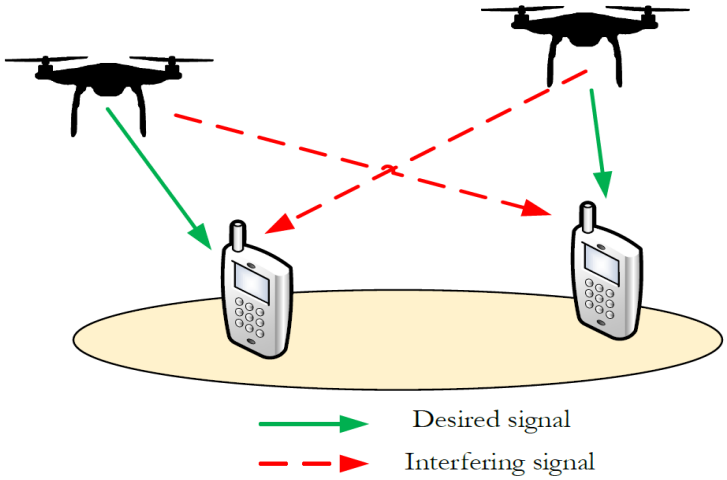

Figure 6.1: Cellular-connected UAV communications subjected to co-channel interference.

$|h|^2$ follows the same distribution as given in (2.6) by replacing $\overline{\gamma}$ with ω. Hence, the PDFs of the desired signal power, denoted as P_D, and interfering signal one, represented as P_F, can be expressed as

$$f_{P_D}(P_D) = \frac{m_{1_D} m_{2_D}}{\omega_D} \mathbb{S}_{DS_D} G_{2,2}^{2,2}\left(\frac{m_{1_D} m_{2_D}}{\omega_D} P_D \middle| \begin{matrix} -\alpha_{2_D}, -\alpha_{1_D} \\ m_{2_D} - 1, m_{1_D} - 1 \end{matrix} \right), \tag{6.3}$$

and

$$f_{P_F}(P_F) = \frac{m_{1_F} m_{2_F}}{\omega_F} \mathbb{S}_{DS_F} G_{2,2}^{2,2}\left(\frac{m_{1_F} m_{2_F}}{\omega_F} P_F \middle| \begin{matrix} -\alpha_{2_F}, -\alpha_{1_F} \\ m_{2_F} - 1, m_{1_F} - 1 \end{matrix} \right). \tag{6.4}$$

The parameters in (6.3) are indexed by D for the desired signal and in (6.4) by F for the interfering one, respectively.

The SIR can be defined as [97]

$$z = \frac{P_D}{P_F}. \tag{6.5}$$

Its PDF can be computed as [104]

$$f_z(z) = \int_0^\infty P_F f_{P_D}(z P_F) f_{P_F}(P_F) \, dP_F. \tag{6.6}$$

By inserting (6.3) and (6.4) into (6.6) and utilizing the integration property of two Meijer G-functions (A.12), the integration in (6.6) can be expressed in a closed-form expression

as

$$f_z(z) = \mathbb{O}_{DD} G_{4,4}^{4,4}\left(\mathbb{V}z \middle| \begin{matrix}\mathbf{a}_1 \\ \mathbf{b}_1\end{matrix}\right), \tag{6.7}$$

where

$$\mathbb{V} = \frac{m_{1_D} m_{2_D}}{m_{1_F} m_{2_F} R}, \tag{6.8}$$

$$\mathbf{a}_1 = \begin{bmatrix} -\alpha_{2_D} & -\alpha_{1_D} & -m_{2_F} & -m_{1_F} \end{bmatrix}, \tag{6.9}$$

$$\mathbf{b}_1 = \begin{bmatrix} m_{2_D} - 1 & m_{1_D} - 1 & \alpha_{2_F} - 1 & \alpha_{1_F} - 1 \end{bmatrix}, \tag{6.10}$$

and $R = \omega_D/\omega_F$ denotes the average SIR value, which can be written as [97]

$$R = \frac{P_{t_D} d_D^{-\eta} \mathbb{E}\{|h_D|^2\}}{P_{t_F} d_F^{-\eta} \mathbb{E}\{|h_F|^2\}}. \tag{6.11}$$

The value of the constant $\mathbb{O}_{DD}$ can be computed as

$$\mathbb{O}_{DD} = \mathbb{S}_{DS_D} \mathbb{S}_{DS_F} \mathbb{V}. \tag{6.12}$$

The outage probability, denoted as P_{out}, represents the likelihood of the SIR dropping below a set threshold, λ. This probability can be calculated as [53]

$$\begin{aligned} P_{out}(\lambda) = F_z(\lambda) &= \int_0^{\lambda} f_z(z)\, dz, \\ &= \lambda \mathbb{O}_{DD} G_{5,5}^{4,5}\left(\mathbb{V}\lambda \middle| \begin{matrix}\mathbf{a}_1, 0 \\ \mathbf{b}_1, -1\end{matrix}\right). \end{aligned} \tag{6.13}$$

The MGF of z can be evaluated as [53]

$$\mathcal{M}_z(s) = \int_0^{\infty} e^{sz} f_z(z) dz. \tag{6.14}$$

Utilizing the integration property in (A.11), (6.14) can be expressed as

$$\mathcal{M}_z(s) = \frac{-\mathbb{O}_{DD}}{s} G_{5,4}^{4,5}\left(\frac{-\mathbb{V}}{s}\middle|\begin{matrix}0, \mathbf{a}_1\\ \mathbf{b}_1\end{matrix}\right). \tag{6.15}$$

6.1.2 SS-SS Case

In this scenario, both the desired and interfering fading channels are characterized by the SS scenario. Employing a methodology akin to that used in sub-section 6.1.1, the PDF of the SIR for this particular scenario can be formulated as

$$f_z(z) = \mathbb{O}_{SS} G_{3,3}^{3,3}\left(\mathbb{V}z\middle|\begin{matrix}\mathbf{a}_2\\ \mathbf{b}_2\end{matrix}\right), \tag{6.16}$$

where

$$\mathbb{O}_{SS} = \mathbb{S}_{SS_D}\mathbb{S}_{SS_F}\mathbb{V}, \tag{6.17}$$

$$\mathbf{a}_2 = \begin{bmatrix}-\alpha_D & -m_{2_F} & -m_{1_F}\end{bmatrix}, \tag{6.18}$$

and

$$\mathbf{b}_2 = \begin{bmatrix}m_{2_D} - 1 & m_{1_D} - 1 & \alpha_F - 1\end{bmatrix}. \tag{6.19}$$

The outage probability can be expressed as

$$P_{out}(\lambda) = F_z(\lambda) = \lambda \mathbb{O}_{SS} G_{4,4}^{3,4}\left(\mathbb{V}\lambda\middle|\begin{matrix}\mathbf{a}_2, 0\\ \mathbf{b}_2, -1\end{matrix}\right). \tag{6.20}$$

The MGF of z can be written as

$$\mathcal{M}_z(s) = \frac{-\mathbb{O}_{SS}}{s} G_{4,3}^{3,4}\left(\frac{-\mathbb{V}}{s}\middle|\begin{matrix}0, \mathbf{a}_2\\ \mathbf{b}_2\end{matrix}\right). \tag{6.21}$$

6.1.3 DS-SS Case

In this case, the desired fading channel is defined by the DS scenario, while the interfering fading channel is characterized by the SS scenario. Applying a similar approach to sub-

section 6.1.1, the PDF of the SIR for this case can be expressed as

$$f_z(z) = \mathbb{O}_{DS} G_{4,3}^{3,4}\left(\mathbb{V}z \middle| \begin{matrix}\mathbf{a}_1 \\ \mathbf{b}_2\end{matrix}\right), \tag{6.22}$$

where

$$\mathbb{O}_{DS} = \mathbb{S}_{DS_D}\mathbb{S}_{SS_F}\mathbb{V}. \tag{6.23}$$

The outage probability can be computed as

$$P_{out}(\lambda) = F_z(\lambda) = \lambda \mathbb{O}_{DS} G_{5,4}^{3,5}\left(\mathbb{V}\lambda \middle| \begin{matrix}\mathbf{a}_1, 0 \\ \mathbf{b}_2, -1\end{matrix}\right). \tag{6.24}$$

The MGF of z can be represented as

$$\mathcal{M}_z(s) = \frac{-\mathbb{O}_{DS}}{s} G_{5,3}^{3,5}\left(\frac{-\mathbb{V}}{s} \middle| \begin{matrix}0, \mathbf{a}_1 \\ \mathbf{b}_2\end{matrix}\right). \tag{6.25}$$

6.1.4 SS-DS Case

In this case, the desired signal is subjected to a SS fading channel while the interfering signal arrives at the receiver via a DS channel. By employing a similar methodology to the one utilized in sub-section 6.1.1, the PDF of the SIR for this case can be written as

$$f_z(z) = \mathbb{O}_{SD} G_{3,4}^{4,3}\left(\mathbb{V}z \middle| \begin{matrix}\mathbf{a}_2 \\ \mathbf{b}_1\end{matrix}\right), \tag{6.26}$$

where

$$\mathbb{O}_{SD} = \mathbb{S}_{SS_D}\mathbb{S}_{DS_F}\mathbb{V}. \tag{6.27}$$

The outage probability can be calculated as

$$P_{out}(\lambda) = F_z(\lambda) = \lambda \mathbb{O}_{SD} G_{4,5}^{4,4}\left(\mathbb{V}\lambda \middle| \begin{matrix}\mathbf{a}_2, 0 \\ \mathbf{b}_1, -1\end{matrix}\right). \tag{6.28}$$

The MGF of z can be written as

$$\mathcal{M}_z(s) = \frac{-\mathbb{O}_{SD}}{s} G_{4,4}^{4,4}\left(\frac{-\mathbb{V}}{s} \middle| \begin{matrix}0, \mathbf{a}_2 \\ \mathbf{b}_1\end{matrix}\right). \tag{6.29}$$

6.2 Asymptotic Analysis

6.2.1 DS-DS Case

By inverting the argument within the Meijer G-function presented in (6.13), utilizing (A.8) and subsequently applying (A.16), the outage probability in (6.13) can be written asymptotically in a simplified form, at a high average SIR value, R, as

$$\begin{aligned} P_{out}\left(\lambda\right) \cong \lambda \mathbb{O}_{DD} \sum_{k=1}^{4} \left(\mathbb{V}\lambda\right)^{b_{1_k}} \\ \times \frac{\prod_{l=1,l\neq k}^{4} \Gamma\left(b_{1_l} - b_{1_k}\right) \prod_{l=1}^{4} \Gamma\left(1 - a_{1_l} + b_{1_k}\right)}{1 + b_{1_k}}, \end{aligned} \tag{6.30}$$

where a_{1_l} is the l^{th} element of the vector $\mathbf{a}_1$ and b_{1_k} is the k^{th} element of the vector $\mathbf{b}_1$.

6.2.2 SS-SS Case

For the SS-SS case, (6.20) can be expressed asymptotically, at high SIR, as

$$\begin{aligned} P_{out}\left(\lambda\right) \cong \lambda \mathbb{O}_{SS} \sum_{k=1}^{3} \left(\mathbb{V}\lambda\right)^{b_{2_k}} \\ \times \frac{\prod_{l=1,l\neq k}^{3} \Gamma\left(b_{2_l} - b_{2_k}\right) \prod_{l=1}^{3} \Gamma\left(1 - a_{2_l} + b_{2_k}\right)}{1 + b_{2_k}}. \end{aligned} \tag{6.31}$$

6.2.3 DS-SS Case

For the DS-SS case, (6.24) can be asymptotically represented, especially under high average SIR, as

$$\begin{aligned} P_{out}\left(\lambda\right) \cong \lambda \mathbb{O}_{DS} \sum_{k=1}^{3} \left(\mathbb{V}\lambda\right)^{b_{2_k}} \\ \times \frac{\prod_{l=1,l\neq k}^{3} \Gamma\left(b_{2_l} - b_{2_k}\right) \prod_{l=1}^{4} \Gamma\left(1 - a_{1_l} + b_{2_k}\right)}{1 + b_{2_k}}. \end{aligned} \tag{6.32}$$

6.2.4 SS-DS Case

For the SS-DS scenario, (6.28) can be asymptotically simplified, particularly at a high average SIR value, as

$$P_{out}(\lambda) \cong \lambda \mathbb{O}_{SD} \sum_{k=1}^{4} (\mathbb{V}\lambda)^{b_{1_k}} \times \frac{\prod_{l=1,l\neq k}^{4} \Gamma(b_{1_l} - b_{1_k}) \prod_{l=1}^{3} \Gamma(1 - a_{2_l} + b_{1_k})}{1 + b_{1_k}}. \tag{6.33}$$

6.3 Simulation Results

This section discusses numerical results that illustrate the performance of the outage probability of an interference-limited system operating over shadowed UAV-to-ground channels. To validate the theoretical expressions discussed in the previous section, a Monte Carlo simulation is generated with 10^7 realizations of fading channels.

The channel parameters employed for Figure 6.2 are $\alpha_1 = m_1 = 2.7$ and $\alpha_2 = m_2 = 3$, with these parameters being identical for both the desired and interfering channels. Figure 6.2 demonstrates that shadowing significantly impacts the value of P_{out}. The minimum value of P_{out} occurs when the desired channel follows SS fading while the interference channel experiences DS fading. Conversely, the highest P_{out} occurs when the desired channel faces DS fading and the interference channel undergoes SS fading. As expected, the DS-DS case achieves a higher outage probability than the SS-SS one. In all cases, the simulation results align perfectly with the analytical expressions, thereby confirming the validity of our analysis.

In Figure 6.3, the outage probability is plotted as a function of the average SIR value, R, in dB for $\lambda = 1$ and various values of α_D for the SS-SS case. The parameters for the desired channels were deliberately set to $m_{1_D} = 1.4$ and $m_{2_D} = 1.6$. Conversely, the interfering channels were configured with parameters $m_{1_F} = 2.1$, $m_{2_F} = 2.2$, and $\alpha_F = 1.8$. It is evident that an increase in α_D leads to performance degradation, primarily attributed to the increasing shadowing effect within the desired channel. At high SIR values, it becomes evident that the asymptotic expression derived in (6.31), utilizing all terms in the summation, rapidly converges to the exact result, thereby demonstrating its tightness.

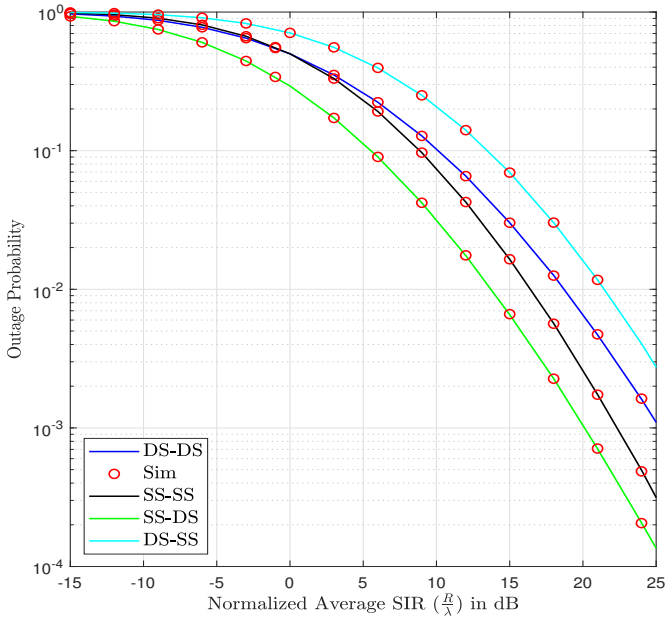

Figure 6.2: Outage probability vs. average SIR in dB.

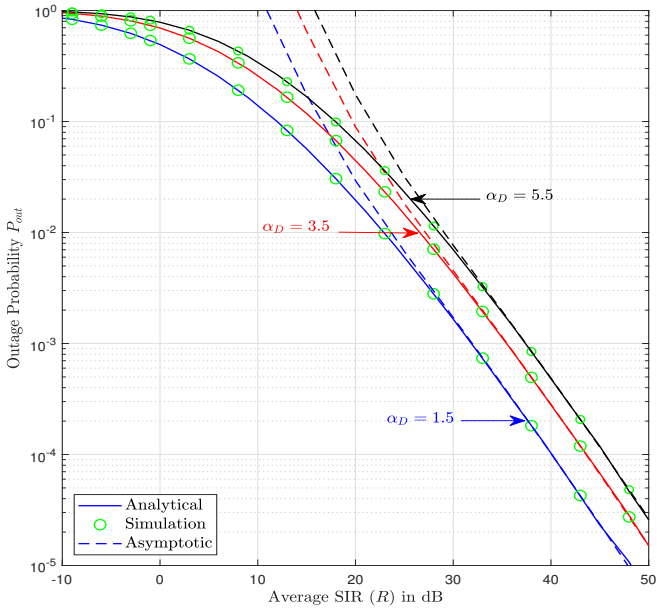

Figure 6.3: Outage probability vs. average SIR in dB for different values of α_D (SS-SS Case).

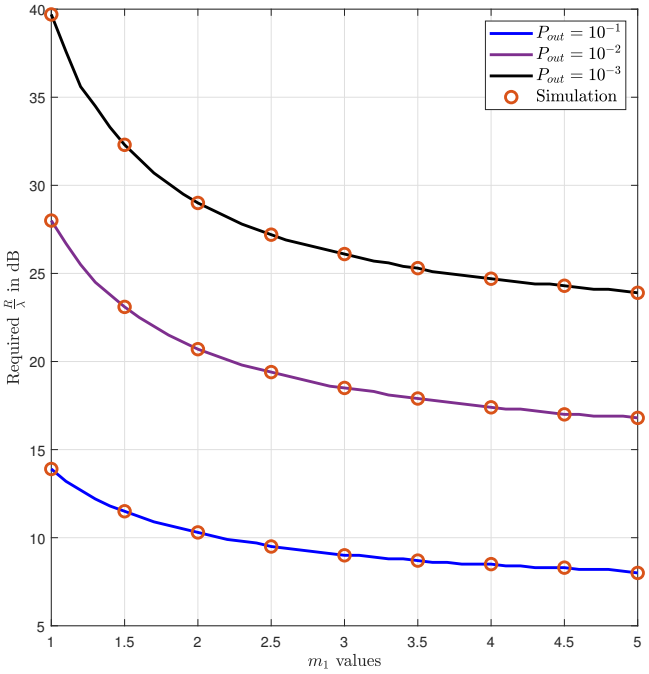

Figure 6.4: Required normalized SIR values in dB for different outage probability values and multipath fading parameter (SS-DS Case).

The analytical expressions derived earlier can be utilized to estimate the required values of $\frac{R}{\lambda}$ to achieve the designated P_{out} across various values of multipath parameter m_1, as plotted in Figure 6.4 for the SS-DS case. The channel parameters were consistent for both the desired and interference channels and were selected to be $m_2 = m_1 + 0.2$, $\alpha_1 = 1.8$, and $\alpha_2 = 1.9$. As P_{out} decreases, the required value of $\frac{R}{\lambda}$ experiences a more pronounced decline with increasing m_1, owing to the reduction in the multipath effect of the channel. Specifically, when m_1 rises from 1 to 4, the required normalized SIR values experience reductions of 15 dB and 5.5 dB at P_{out} levels of 10^{-3} and 10^{-1}, respectively.

6.4 Conclusion

This chapter introduces closed-form and asymptotic expressions that calculate the outage probability of an interference-limited system operating across UAV-to-ground channels afflicted by shadowing. These derived expressions, validated via Monte Carlo simulations,

are in terms of the Meijer G-function, MATLAB's built-in function. The findings emphasize how channel characteristics significantly influence outage probability. Moving forward, forthcoming research might explore innovative methods to address interference mitigation in UAV-to-ground communication systems.

Chapter 7

Cascaded Shadowed UAV-to-Ground Channels

The use of cascaded fading channels has proven to be adaptable to diverse scenarios. These scenarios encompass multi-hop cooperative communications [105], channels for mobile-to-mobile transmissions [106], dual-hop fading channels [107], pinhole channels in radio-frequency identification [108], and communication systems employing MIMO keyhole technology [109].

The performance of multi-hop UAV-enabled communications has been examined in prior studies [110–112]. Notably, the work presented in [110] delves into the analysis of RIS-assisted UAV communications under Nakagami-m fading conditions. Research efforts in [111] have focused on optimizing the placement of UAVs, while [112] considers the crucial objective of maximizing the average end-to-end throughput. Table 7.1 illustrates the types of fading channels used in previous work on multi-hop systems involving UAVs. However, it is noteworthy that the aforementioned papers do not consider the effects of shadowing on a UAV-enabled communication system. A realistic representation of the UAV-to-ground channel, incorporating the effects of shadowing, becomes imperative due to the motion of the Tx, Rx, or significant scatterers in their vicinity. Consequently, shadowed UAV-to-ground channel models emerge as a prudent approach to capture the random variations in the received signal power.

In this chapter, we present a comprehensive reliability analysis of communication systems operating across cascaded UAV-to-ground fading channels that were supported by

Table 7.1: Fading distributions for previous work on multi-hop systems involving UAVs.

Ref.	Objective	Fading Distribution
[110]	Performance analysis	Nakagami–m
[111]	use of multiple UAVs in relaying	Nakagami–m
[112]	Throughput improvement	Ricean
[113]	Energy-efficient data collection	Ricean (A2A links)
[114]	training optimization	Ricean
[115]	Wireless backhaul	Ricean

empirical measurements [34]. The main contributions of this study can be succinctly outlined as follows:

- Introduction of the cascaded shadowed UAV-to-ground distribution through a comprehensive analysis of its PDF and CDF expressions.
- Using the derived statistical expressions, the performance of cascaded UAV-to-ground fading channels can be evaluated through metrics such as outage probability, average channel capacity, and ABER, all of which are articulated in closed-form expressions.
- Conducting numerical simulations to validate our analytical findings.

The remainder of this chapter is structured as follows. In Section 7.1, a statistical characterization of the cascaded shadowed UAV-to-ground fading channel is derived. Section 7.2 showcases the application of cascaded shadowed UAV-to-ground fading channels in analyzing the performance of wireless communication systems. Section 7.3 provides asymptotic expressions for the performance metrics at high SNR values. In Section 7.4, we present illustrative numerical results accompanied by insightful discussions. Lastly, Section 7.5 encapsulates concluding remarks and outlines potential directions for future work.

7.1 Cascaded Channels

Suppose a UAV in the air acts as an intermediate node, shown in Fig. 7.1, over cascaded UAV-to-ground channels. The instantaneous received SNR at the desired destination can

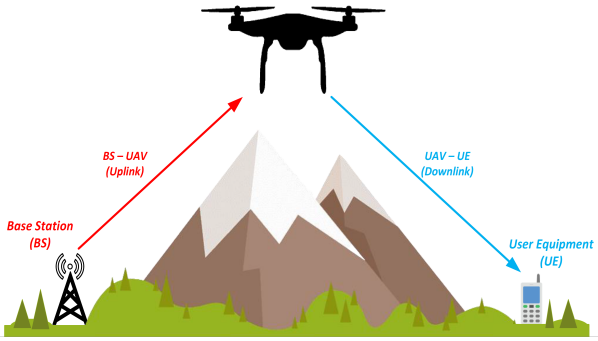

Figure 7.1: System model for communication with UAV cascaded channels.

be expressed as

$$\gamma_{eq} = \overline{\gamma_{eq}} \prod_{i=1}^{2} |h_i|^2. \tag{7.1}$$

In this case, $\overline{\gamma_{eq}}$ represents the average SNR value at the Rx, whose value can be computed as

$$\overline{\gamma_{eq}} = \frac{P_t}{\sigma_N^2} d^{-\eta} \mathbb{E}\{\prod_{i=1}^{2} |h_i|^2\}, \tag{7.2}$$

P_t denotes the transmission power, d is the overall propagation distance, σ_N^2 is the noise variance, and η is the path-loss exponent. h_i is the channel fading coefficient. It is assumed that all h_i are statistically independent, but not necessarily identically distributed. $|h_i|^2$ follows the same distribution as γ by putting $\overline{\gamma} = 1$ in (2.8) for the DS case and (2.23) for the SS one, respectively.

7.1.1 DS-DS case

In the DS-DS case, shadowing exists around the UAV in the air, the base station, and user equipment on the ground. Thus, we consider that this communication link follows a cascaded DS fading channel model. As illustrated in (2.8), the DS distribution is considered a special case of Fox H-function distribution. Through rigorous mathematical manipulations, based on the transformation property of Fox H-function [116, eq. (3.12)], the PDF of the received SNR, as defined in (7.1) for the DS-DS case, can be expressed as

$$f_{\gamma_{eq}}(\gamma_{eq}) = {\gamma_{eq}}^{-1}\mathbb{L}_{DD}G_{4,4}^{4,4}\left(\frac{\mathbb{K}}{\overline{\gamma_{eq}}}\gamma_{eq}\middle|\begin{matrix}\mathbf{a}_{DD}\\ \mathbf{b}\end{matrix}\right), \tag{7.3}$$

where

$$\mathbb{K} = m_{2_N} m_{1_N} m_{2_U} m_{1_U}, \tag{7.4}$$

$$\mathbf{b} = \begin{bmatrix} m_{2_N} & m_{1_N} & m_{2_U} & m_{1_U} \end{bmatrix}, \tag{7.5}$$

$$\mathbb{L}_{DD} = \frac{1}{\Gamma(m_{2_N})\Gamma(m_{1_N})\Gamma(\alpha_{1_N})\Gamma(\alpha_{2_N})} \times \frac{1}{\Gamma(m_{2_U})\Gamma(m_{1_U})\Gamma(\alpha_{1_U})\Gamma(\alpha_{2_U})}, \tag{7.6}$$

and

$$\mathbf{a}_{DD} = \begin{bmatrix} 1-\alpha_{2_N} & 1-\alpha_{1_N} & 1-\alpha_{2_U} & 1-\alpha_{1_U} \end{bmatrix}. \tag{7.7}$$

The subscripts N and U denote the downlink and uplink channels, respectively. The CDF of the received SNR can be evaluated as

$$\begin{aligned} F_{\gamma_{eq}}(\gamma_{eq}) &= \int_0^{\gamma_{eq}} f_{\gamma_{eq}}(\gamma_{eq})\, d\gamma_{eq}, \\ &= \mathbb{L}_{DD}G_{5,5}^{4,5}\left(\frac{\mathbb{K}}{\overline{\gamma_{eq}}}\gamma_{eq}\middle|\begin{matrix}\mathbf{a}_{DD}, 1\\ \mathbf{b}, 0\end{matrix}\right). \end{aligned} \tag{7.8}$$

7.1.2 SS-SS case

In that case, shadowing exists around the base station and the ground-based user equipment. Thus, we consider the communication link to follow a cascaded SS fading channel model. The PDF of the instantaneous SNR, defined in (7.1) for the SS-SS case, can be expressed as

$$f_{\gamma_{eq}}(\gamma_{eq}) = \gamma_{eq}^{-1}\mathbb{L}_{SS}G_{2,4}^{4,2}\left(\frac{\mathbb{K}}{\overline{\gamma_{eq}}}\gamma_{eq}\middle|\begin{matrix}\mathbf{a}_{SS}\\ \mathbf{b}\end{matrix}\right). \tag{7.9}$$

In this case, the CDF can be computed as

$$F_{\gamma_{eq}}\left(\gamma_{eq}\right) = \mathbb{L}_{SS} G_{3,5}^{4,3}\left(\frac{\mathbb{K}}{\overline{\gamma_{eq}}}\gamma_{eq}\middle|\begin{matrix}\mathbf{a}_{SS}, 1\\ \mathbf{b}, 0\end{matrix}\right), \tag{7.10}$$

where

$$\mathbf{a}_{SS} = \begin{bmatrix}1-\alpha_N & 1-\alpha_U\end{bmatrix}, \tag{7.11}$$

and

$$\mathbb{L}_{SS} = \frac{1}{\Gamma\left(m_{2_N}\right)\Gamma\left(m_{1_N}\right)\Gamma\left(\alpha_N\right)\Gamma\left(m_{2_U}\right)\Gamma\left(m_{1_U}\right)\Gamma\left(\alpha_U\right)}. \tag{7.12}$$

7.1.3 DS-SS case

In that case, shadowing exists around the UAV in the sky and the base station, but not around user equipment on the ground. Thus, we consider the communication link to follow a cascaded DS-SS fading channel model. The PDF and CDF of the instantaneous SNR defined in (7.1) can be expressed as

$$f_{\gamma_{eq}}(\gamma_{eq}) = \gamma_{eq}^{-1}\mathbb{L}_{DS} G_{3,4}^{4,3}\left(\frac{\mathbb{K}}{\overline{\gamma_{eq}}}\gamma_{eq}\middle|\begin{matrix}\mathbf{a}_{DS}\\ \mathbf{b}\end{matrix}\right). \tag{7.13}$$

In this scenario, the CDF can be evaluated as

$$F_{\gamma_{eq}}\left(\gamma_{eq}\right) = \mathbb{L}_{DS} G_{4,5}^{4,4}\left(\frac{\mathbb{K}}{\overline{\gamma_{eq}}}\gamma_{eq}\middle|\begin{matrix}\mathbf{a}_{DS}, 1\\ \mathbf{b}, 0\end{matrix}\right), \tag{7.14}$$

where

$$\mathbf{a}_{DS} = \begin{bmatrix}1-\alpha_N & 1-\alpha_{1_U} & 1-\alpha_{2_U}\end{bmatrix}, \tag{7.15}$$

and

$$\mathbb{L}_{DS} = \frac{1}{\Gamma\left(m_{2_N}\right)\Gamma\left(m_{1_N}\right)\Gamma\left(\alpha_N\right)} \times \frac{1}{\Gamma\left(m_{2_U}\right)\Gamma\left(m_{1_U}\right)\Gamma\left(\alpha_{1_U}\right)\left(\alpha_{2_U}\right)}. \tag{7.16}$$

7.1.4 SS-DS case

In that case, shadowing exists around the UAV in the sky and the user equipment, but not around the base station on the ground. Thus, we consider the communication link to follow a cascaded SS-DS fading channel model, which follows the same analysis as the previous case by swapping N with U in (7.13), (7.14) and (7.16).

7.2 Performance Analysis

In this section, we evaluate the system performance in terms of outage probability, ergodic capacity, and ABER.

7.2.1 Outage Probability

The outage probability, denoted as P_{out}, signifies the likelihood that the output SNR falls below a predefined threshold, γ_{th} [91]. The expression for P_{out} can be expressed as

$$\begin{aligned} P_{\text{out}} &= \mathbb{P}(\gamma_{eq} < \gamma_{th}), \\ &= F_{\gamma_{eq}}(\gamma_{th}), \end{aligned} \tag{7.17}$$

which can be evaluated through (7.8), (7.10), and (7.14) for the DS-DS, SS-SS, and DS-SS, respectively.

7.2.2 Ergodic Capacity

The ergodic capacity can be evaluated as

$$C_{\text{ER}} = \frac{\mathbb{B}}{\ln(2)} \int_0^\infty \ln(1+\gamma_{eq}) f_{\gamma_{eq}}(\gamma_{eq})\, d\gamma_{eq}. \tag{7.18}$$

7.2.2.1 DS-DS case

Using (A.4), the natural logarithm function can be expressed in terms of the Meijer G-function. Then, the integration in (7.18) involves the multiplication of two Meijer G-

functions, which can be expressed in a closed-form expression as

$$C_{\mathrm{ER}} = \frac{\mathbb{B}\mathbb{L}_{DD}}{\ln(2)} G_{6,6}^{6,5}\left(\frac{\mathbb{K}}{\overline{\gamma_{eq}}}\middle|\begin{matrix}\mathbf{a}_{DD}, 0, 1\\ \mathbf{b}, 0, 0\end{matrix}\right). \tag{7.19}$$

7.2.2.2 SS-SS case

Similarly for the SS-SS case, C_{ER} can be evaluated as

$$C_{\mathrm{ER}} = \frac{\mathbb{B}\mathbb{L}_{SS}}{\ln(2)} G_{4,6}^{6,3}\left(\frac{\mathbb{K}}{\overline{\gamma_{eq}}}\middle|\begin{matrix}\mathbf{a}_{SS}, 0, 1\\ \mathbf{b}, 0, 0\end{matrix}\right). \tag{7.20}$$

7.2.2.3 DS-SS case

Using a similar manner for the DS-SS scenario, C can be computed as

$$C_{\mathrm{ER}} = \frac{\mathbb{B}\mathbb{L}_{DS}}{\ln(2)} G_{5,6}^{6,4}\left(\frac{\mathbb{K}}{\overline{\gamma_{eq}}}\middle|\begin{matrix}\mathbf{a}_{DS}, 0, 1\\ \mathbf{b}, 0, 0\end{matrix}\right). \tag{7.21}$$

7.2.3 ABER

Using the CDF-based approach [56], the ABER can be expressed as

$$P_{be} = \frac{\kappa^{\theta}}{2\Gamma(\theta)} \int_0^{\infty} {\gamma_{eq}}^{\theta-1} e^{-\kappa\gamma_{eq}} F_{\gamma_{eq}}(\gamma_{eq})\, d\gamma_{eq}, \tag{7.22}$$

where $(\kappa, \theta) = (1, 0.5)$ for BPSK and $(\kappa, \theta) = (0.5, 0.5)$ coherent BFSK modulations.

7.2.3.1 DS-DS case

Utilizing (A.3), the exponential function can be represented in terms of a Meijer G-function. Then, the integration in (7.22) entails the product of two Meijer G-functions, which can be resolved in a closed-form expression for the DS-DS case as

$$P_{be} = \frac{\mathbb{L}_{DD}}{2\Gamma(\theta)} G_{6,5}^{4,6}\left(\frac{\mathbb{K}}{\overline{\gamma_{eq}}\kappa}\middle|\begin{matrix}\mathbf{a}_{DD}, 1, 0.5\\ \mathbf{b}, 0\end{matrix}\right). \tag{7.23}$$

7.2.3.2 SS-SS case

Similarly for the SS-SS case, ABER can be evaluated as

$$P_{be} = \frac{\mathbb{L}_{SS}}{2\Gamma(\theta)} G_{4,5}^{4,4}\left(\frac{\mathbb{K}}{\overline{\gamma_{eq}}\kappa}\middle|\begin{matrix}\mathbf{a}_{SS}, 1, 0.5\\ \mathbf{b}, 0\end{matrix}\right). \tag{7.24}$$

7.2.3.3 DS-SS case

Applying a similar approach for the DS-SS case, ABER can be computed as

$$P_{be} = \frac{\mathbb{L}_{DS}}{2\Gamma(\theta)} G_{5,5}^{4,5}\left(\frac{\mathbb{K}}{\overline{\gamma_{eq}}\kappa}\middle|\begin{matrix}\mathbf{a}_{DS}, 1, 0.5\\ \mathbf{b}, 0\end{matrix}\right). \tag{7.25}$$

7.3 Asymptotic Analysis

In this section, we present asymptotic expressions for the previously discussed performance metrics at high SNR values. These expressions are derived following the methodology outlined in section 6.2.

7.3.1 Outage Probability

7.3.1.1 DS-DS case

At a high average SNR value, (7.8) can be asymptotically written as

$$\begin{aligned} P_{out}\left(\gamma_{th}\right) \approxeq \mathbb{L}_{DD} \sum_{k=1}^{4} \left(\frac{\mathbb{K}\gamma_{th}}{\overline{\gamma_{eq}}}\right)^{b_k} \\ \times \frac{\prod_{l=1, l\neq k}^{4} \Gamma\left(b_l - b_k\right) \prod_{l=1}^{4} \Gamma\left(1 - a_{DD_l} + b_k\right)}{b_k}. \end{aligned} \tag{7.26}$$

7.3.1.2 SS-SS case

Similarly for the SS-SS case, (7.10) can be asymptotically represented at high average SNR values as

$$P_{out}\left(\gamma_{th}\right) \approxeq \mathbb{L}_{SS} \sum_{k=1}^{4} \left(\frac{\mathbb{K}\gamma_{th}}{\overline{\gamma_{eq}}}\right)^{b_k} \times \frac{\prod_{l=1,l\neq k}^{4} \Gamma\left(b_l - b_k\right) \prod_{l=1}^{2} \Gamma\left(1 - a_{SS_l} + b_k\right)}{b_k}. \tag{7.27}$$

7.3.1.3 DS-SS case

Similarly, in the DS-SS scenario, (7.14) can be asymptotically expressed for high average SNR values as

$$P_{out}\left(\gamma_{th}\right) \approxeq \mathbb{L}_{DS} \sum_{k=1}^{4} \left(\frac{\mathbb{K}\gamma_{th}}{\overline{\gamma_{eq}}}\right)^{b_k} \times \frac{\prod_{l=1,l\neq k}^{4} \Gamma\left(b_l - b_k\right) \prod_{l=1}^{3} \Gamma\left(1 - a_{DS_l} + b_k\right)}{b_k}. \tag{7.28}$$

7.3.2 Ergodic Capacity

7.3.2.1 DS-DS case

At a high average SNR value, (7.19) can be asymptotically written as

$$C_{\text{ER}} \approxeq \frac{\mathbb{B}\mathbb{L}_{DD}}{\ln\left(2\right)} \sum_{k=1}^{6} \left(\frac{\mathbb{K}}{\overline{\gamma_{eq}}}\right)^{f_k} \times \frac{\prod_{l=1,l\neq k}^{6} \Gamma\left(f_l - f_k\right) \prod_{l=1}^{4} \Gamma\left(1 - a_{DD_l} + f_k\right)}{f_k^{-1}}, \tag{7.29}$$

where f_k is the k^{th} element of the vector $\mathbf{f}$, $\mathbf{f} = [\mathbf{b}, 0, 0]$.

7.3.2.2 SS-SS case

Similarly for the SS-SS case, (7.20) can be asymptotically represented at high average SNR values as

$$C_{\mathrm{ER}} \approxeq \frac{\mathbb{B}\mathbb{L}_{SS}}{\ln(2)} \sum_{k=1}^{6} \left(\frac{\mathbb{K}}{\overline{\gamma_{eq}}} \right)^{f_k} \times \frac{\prod_{l=1,l\neq k}^{6} \Gamma(f_l - f_k) \prod_{l=1}^{2} \Gamma(1 - a_{SS_l} + f_k)}{f_k^{-1}}. \tag{7.30}$$

7.3.2.3 DS-SS case

Similarly, in the DS-SS scenario, (7.21) can be asymptotically expressed for high average SNR values as

$$C_{\mathrm{ER}} \approxeq \frac{\mathbb{B}\mathbb{L}_{DS}}{\ln(2)} \sum_{k=1}^{6} \left(\frac{\mathbb{K}}{\overline{\gamma_{eq}}} \right)^{f_k} \times \frac{\prod_{l=1,l\neq k}^{6} \Gamma(f_l - f_k) \prod_{l=1}^{3} \Gamma(1 - a_{DS_l} + f_k)}{f_k^{-1}}. \tag{7.31}$$

7.3.3 ABER

7.3.3.1 DS-DS case

At a high average SNR value, (7.23) can be asymptotically written as

$$P_{be} \approxeq \frac{\mathbb{L}_{DD}}{2\Gamma(\theta)} \sum_{k=1}^{4} \left(\frac{\mathbb{K}}{\overline{\gamma_{eq}}\kappa} \right)^{b_k} \times \frac{\prod_{l=1,l\neq k}^{4} \Gamma(b_l - b_k) \prod_{l=1}^{4} \Gamma(1 - a_{DD_l} + b_k) \Gamma(0.5 + b_k)}{b_k}. \tag{7.32}$$

7.3.3.2 SS-SS case

Similarly for the SS-SS case, (7.24) can be asymptotically represented at high average SNR values as

$$P_{be} \approx \frac{\mathbb{L}_{SS}}{2\Gamma(\theta)} \sum_{k=1}^{4} \left(\frac{\mathbb{K}}{\overline{\gamma_{eq}}\kappa} \right)^{b_k} \times \frac{\prod_{l=1,l\neq k}^{4} \Gamma\left(b_l - b_k\right) \prod_{l=1}^{2} \Gamma\left(1 - a_{SS_l} + b_k\right) \Gamma\left(0.5 + b_k\right)}{b_k}. \tag{7.33}$$

7.3.3.3 DS-SS case

Similarly, in the DS-SS scenario, (7.25) can be asymptotically expressed for high average SNR values as

$$P_{be} \approx \frac{\mathbb{L}_{DS}}{2\Gamma(\theta)} \sum_{k=1}^{4} \left(\frac{\mathbb{K}}{\overline{\gamma_{eq}}\kappa} \right)^{b_k} \times \frac{\prod_{l=1,l\neq k}^{4} \Gamma\left(b_l - b_k\right) \prod_{l=1}^{3} \Gamma\left(1 - a_{DS_l} + b_k\right) \Gamma\left(0.5 + b_k\right)}{b_k}. \tag{7.34}$$

7.4 Numerical Results

In this section, we validate the accuracy of our analytical expressions in the preceding section by conducting a Monte Carlo simulation with 10^6 realizations of fading channels.

In Figure 7.2, the plot illustrates the normalized average channel capacity, $C_{\mathrm{ER}}/\mathbb{B}$, as a function of the average received SNR, $\overline{\gamma_{eq}}$ in dB. The fading channel parameters were identical for both the uplink and downlink channels, with $m_1 = 1.5$, $m_2 = 1.8$ and $\alpha_2 = \alpha_1 + 0.1$. As anticipated, the SS-SS scenario outperforms the DS-DS or DS-SS cases, showcasing superior performance attributed to its minimal occurrence of shadowing zones. This superiority aligns with expectations, given the reduced impact of shadowing in the SS-SS configuration. Additionally, it is noteworthy that the system's performance exhibits a decline with increasing values of α_1, signifying a higher degree of shadowing severity. The difference in rate performance between the SS-SS and DS-DS cases becomes more pronounced as α_1 increases.

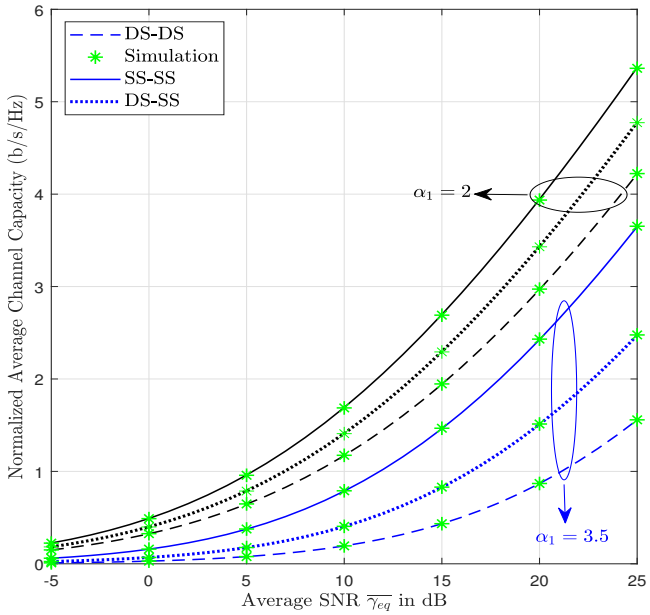

Figure 7.2: Normalized average channel capacity vs. the average SNR $\overline{\gamma_{eq}}$ in dB.

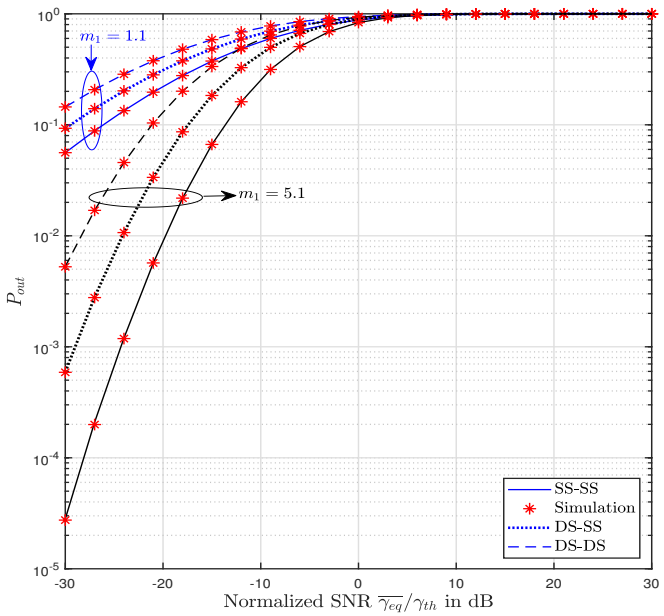

Figure 7.3: Outage Probability vs. normalized SNR in dB.

In Figure 7.3, the outage probability is illustrated as a function of the normalized SNR, $\overline{\gamma_{eq}}/\gamma_{th}$, in dB. The fading channel parameters were the same for both the uplink and downlink channels, where $\alpha_1 = 2.1$, $\alpha_2 = 2.4$ and $m_2 = m_1 + 0.3$ Interestingly, the DS-DS scenario stands out with the highest outage probability when compared to other cases. It is worth noting that as the value of m_1 increases, indicating a lower fluctuation in the received SNR, there is a noticeable decline in the outage probability, P_{out}. When the normalized SNR is -30 dB, the outage probability of DS-DS surpasses that of SS-SS by a factor of 3, given $m_1 = 1.1$. However, with $m_1 = 5.1$, the outage probability of DS-DS escalates to almost 200 times that of SS-SS.

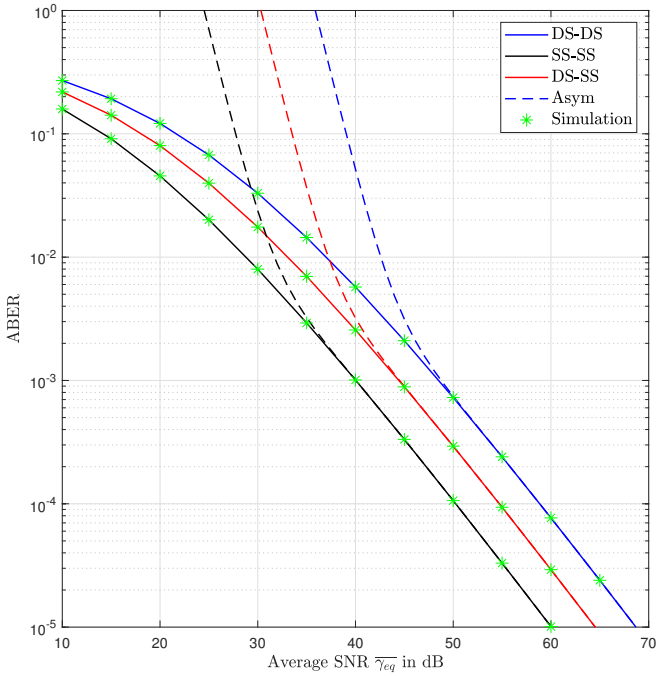

Figure 7.4: Error Probability versus Average SNR in dB.

In Figure 7.4, the ABER is plotted against the average SNR value $\overline{\gamma_{eq}}$ in dB for the BPSK modulation scheme. The fading channel parameters the uplink channel were selected to be $m_1 = 1.1$, $m_2 = 1.2$, $\alpha_1 = 2.5$ and $\alpha_2 = 2.6$. Whereas for the downlink one, the parameters are $m_1 = 3.3$, $m_2 = 3.4$, $\alpha_1 = 2.7$ and $\alpha_2 = 2.8$. The lowest error rate is observed in the SS-SS case. Notably, all theoretical curves depicted in this section were implemented using MATLAB's built-in Meijer G-function and were validated through Monte Carlo simulations. At high SNR values, it becomes evident that the asymptotic expression

derived in subsection 7.3.3, utilizing all terms in the summation, rapidly converges to the exact result, thereby demonstrating its tightness.

7.5 Conclusion

In this chapter, we introduced the cascaded UAV-to-ground fading channel along with a comprehensive analysis of its statistical characteristics, which were utilized to evaluate key performance metrics such as outage probability, average channel capacity, and ABER. To quantify these metrics, closed-form expressions were derived employing the Meijer G-function. The validity of these analytical results was further confirmed through Monte-Carlo simulations. One of the possible future research directions is to extend our analysis to the case of correlated cascaded UAV-to-ground fading channels.

Chapter 8

Energy Detection-based Spectrum Sensing

Due to the extensive radio frequency transmission footprint from UAVs to ground nodes, UAV communications can significantly degrade the performance of co-channel ground communication links [117]. With limited dedicated spectrum available, researchers are tasked with designing efficient spectrum-sharing policies for UAV communications to boost spectral efficiency and mitigate interference to ground communications. One such technique for spectrum sharing is energy detection (ED), a noncoherent detection method that gauges the energy level of an unknown received signal and compares it with a predefined threshold to determine its presence or absence within a given bandwidth [118]. Due to its simplicity and independence from prior knowledge of the received signal, ED stands out as the most practical spectrum sensing method for cognitive radio (CR) [119].

The detection performance of ED-based spectrum sensing is greatly impacted by the characteristics of the fading channel it operates in. Consequently, researchers have extensively investigated the performance of ED-based spectrum sensing across various fading channel models, including Rayleigh, Rician, and Nakagami channels [120]. Moreover, recent studies have delved into more complex fading scenarios such as κ-μ [121], fading two-wave with diffuse power fading channels [122], and Fisher-Snedecor $\mathcal{F}$ channels [123].

This chapter presents an analysis of ED-based spectrum sensing over shadowed UAV-to-ground fading channels, a scenario that has not been previously explored in existing literature. Our contributions can be outlined as follows:

- We provide a computationally tractable analytic expression for the average detection probability in energy detection-based spectrum sensing over shadowed UAV-to-ground fading channels.
- We further extend our analysis to encompass collaborative spectrum sensing techniques aimed at enhancing detection performance.
- Additionally, we evaluate the performance of ED-based spectrum sensing over UAV-to-ground fading channels by employing complementary receiver operating characteristic (ROC) curves for a comprehensive performance assessment.

The structure of the remaining sections in this chapter is as follows: Section 8.1 analyzes the average detection probabilities of the energy detector over UAV-to-ground channel models. Following this, Section 8.2 presents numerical results and discussions. Finally, Section 8.3 contains our concluding remarks.

8.1 Energy Detection Analysis

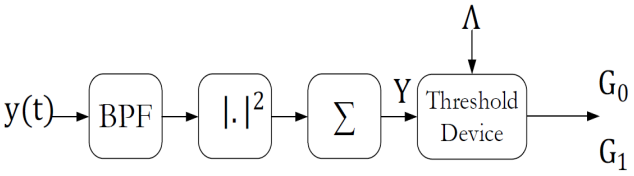

Figure 8.1: System modeling for ED receiver.

The UAV is equipped with an ED receiver and acts as a sensing node (SN) that employs spectrum sensing techniques to identify spectrum holes, ensuring UAV transmission occurs solely when the primary transmission between the terrestrial base station and a ground node is inactive. The fading channel between the UAV and the ground node could be characterized by DS or SS communication scenarios. At the output of the ED, the received signal $y(t)$ is expressed as follows [120]:

$$y(t) = \begin{cases} n(t) & G_0 \\ h(t)\,x(t) + n(t) & G_1 \end{cases}, \tag{8.1}$$

where $x(t)$ represents the transmitted signal, $h(t)$ denotes the channel gain, and $n(t)$ signifies the noise, which is assumed to follow an AWGN model. Additionally, in (8.1), it is apparent that two binary hypotheses are considered, specifically G_0 and G_1. G_0 indicates the absence of $s(t)$, while G_1 represents the presence of $x(t)$.

In a typical ED receiver, as illustrated in Figure 8.1, the configuration includes a band-pass filter (BPF), followed by a squaring device, an integrator, and a threshold unit. Initially, the received signal undergoes filtration through an ideal BPF within a predetermined bandwidth $\mathbb{B}$. Subsequently, the filtered signal is squared and integrated over an observation interval $\mathbb{T}$ to yield the test statistic Y, which is then compared by a predefined energy threshold represented by Λ. This threshold plays a critical role in the decision-making process and is closely associated with three key metrics that collectively assess the detector's performance [124]:

1. The probability of false alarm, denoted as $\mathcal{P}_f$, which refers to the rate of incorrectly identifying a signal when it is not present, can be computed as

$$\mathcal{P}_f = \mathbb{P}\left(Y > \Lambda | G_0\right) = \frac{\Gamma\left(u, \Lambda/2\right)}{\Gamma\left(u\right)}, \tag{8.2}$$

   where $u = \mathbb{B}\mathbb{T}$ represents the time-bandwidth product and $\Gamma(.,.)$ is upper incomplete gamma function.

2. The probability of detection, denoted as $\mathcal{P}_d$, which is the rate of accurately detecting a signal when it is present, can be calculated as

$$\mathcal{P}_d = \mathbb{P}\left(Y > \Lambda | G_1\right) = Q_u\left(\sqrt{2\gamma}, \sqrt{\Lambda}\right), \tag{8.3}$$

   where $Q_u(.,.)$ is the Generalized Marcum Q-function [125, eq. (1)].

3. The probability of missed detection denoted as $\mathcal{P}_m$, which is the rate of failing to detect a signal when it is present, can be evaluated as

$$\mathcal{P}_m = 1 - \mathcal{P}_d. \tag{8.4}$$

8.1.1 Single User Spectrum Sensing

To evaluate the average detection probability, denoted as $\overline{\mathcal{P}_d}$, (8.3) requires averaging across all potential values of γ. This entails computing the following integration:

$$\overline{\mathcal{P}_d} = \int_{-\infty}^{\infty} Q_u\left(\sqrt{2\gamma}, \sqrt{\Lambda}\right) f_\gamma(\gamma)\, d\gamma. \tag{8.5}$$

With the help of [126], the generalized Marcum Q-function in (8.5) can be represented as an infinite series as

$$Q_u(\sqrt{2\gamma}, \sqrt{\Lambda}) = \exp(-\gamma) \sum_{n=0}^{\infty} \frac{\gamma^n \Gamma(n+2, \Lambda/2)}{\Gamma(n+1)\,\Gamma(n+u)}. \tag{8.6}$$

Thus, (8.5) can be re-written as

$$\overline{\mathcal{P}_d} = \sum_{n=0}^{\infty} \frac{\Gamma(n+2, \Lambda/2)}{\Gamma(n+1)\,\Gamma(n+u)} \int_{-\infty}^{\infty} \exp(-\gamma)\gamma^n f_\gamma(\gamma)\, d\gamma. \tag{8.7}$$

8.1.1.1 DS Case

For the DS case, by substituting (2.6) into (8.7) and applying (A.11), (8.7) can be expressed in a closed-form expression as

$$\overline{\mathcal{P}_d} = \sum_{n=0}^{\infty} \frac{\Gamma(n+2, \Lambda/2)}{\Gamma(n+1)\,\Gamma(n+u)} \mathbb{S}_{DS} G_{2,3}^{3,2}\left(\frac{m_1 m_2}{\overline{\gamma}} \middle| \begin{matrix} 1-n, 1-\alpha_2, 1-\alpha_1 \\ m_1, m_2 \end{matrix}\right). \tag{8.8}$$

8.1.1.2 SS Case

Similarly for the SS case, if (2.21) is substituted into (8.7) and applying (A.11), (8.7) can be evaluated as

$$\overline{\mathcal{P}_d} = \sum_{n=0}^{\infty} \frac{\Gamma(n+2, \Lambda/2)}{\Gamma(n+1)\,\Gamma(n+u)} \mathbb{S}_{SS} G_{2,2}^{2,2}\left(\frac{m_1 m_2}{\overline{\gamma}} \middle| \begin{matrix} 1-n, 1-\alpha \\ m_1, m_2 \end{matrix}\right). \tag{8.9}$$

8.1.2 Collaborative Spectrum Sensing

In [127], it has been demonstrated that the performance of ED-based spectrum sensing can be notably enhanced through collaborative efforts among SNs when they share their information. It is assumed that all L SNs experience independent and identically distributed fading and utilize the same threshold value, Λ. In such scenarios involving collaboration among L SNs, the probability of false alarm can be expressed as follows

$$\mathcal{C}_f = 1 - [1 - \mathcal{P}_f]^L, = 1 - \left[1 - \frac{\Gamma(u, \Lambda/2)}{\Gamma(u)}\right]^L. \tag{8.10}$$

In this case, the probability of detection can be given as

$$\mathcal{C}_d = 1 - [1 - \mathcal{P}_d]^L. \tag{8.11}$$

8.1.2.1 DS Case

In the case of the DS scenario, by substituting (8.8) into (8.11), The average value of detection probability for a collaborative spectrum sensing with L collaborative SNs can be articulated as

$$\overline{\mathcal{C}_d} = 1 - \left[1 - \sum_{n=0}^{\infty} \frac{\Gamma(n+2, \Lambda/2)}{\Gamma(n+1)\Gamma(n+u)} \mathbb{S}_{DS} G_{2,3}^{3,2}\left(\frac{m_1 m_2}{\overline{\gamma}} \middle| \begin{matrix} 1-n, 1-\alpha_2, 1-\alpha_1 \\ m_1, m_2 \end{matrix}\right)\right]^L. \tag{8.12}$$

8.1.2.2 SS Case

Similarly for the SS case, if (8.9) is substituted into (8.11), (8.11) can be evaluated as

$$\overline{\mathcal{C}_d} = 1 - \left[1 - \sum_{n=0}^{\infty} \frac{\Gamma(n+2, \Lambda/2)}{\Gamma(n+1)\Gamma(n+u)} \mathbb{S}_{SS} G_{2,2}^{2,2}\left(\frac{m_1 m_2}{\overline{\gamma}} \middle| \begin{matrix} 1-n, 1-\alpha \\ m_1, m_2 \end{matrix}\right)\right]^L. \tag{8.13}$$

8.2 Numerical Results

In this section, we validate the accuracy of our analytical expressions in the preceding section by conducting a Monte Carlo simulation with 10^6 realizations of fading channels.

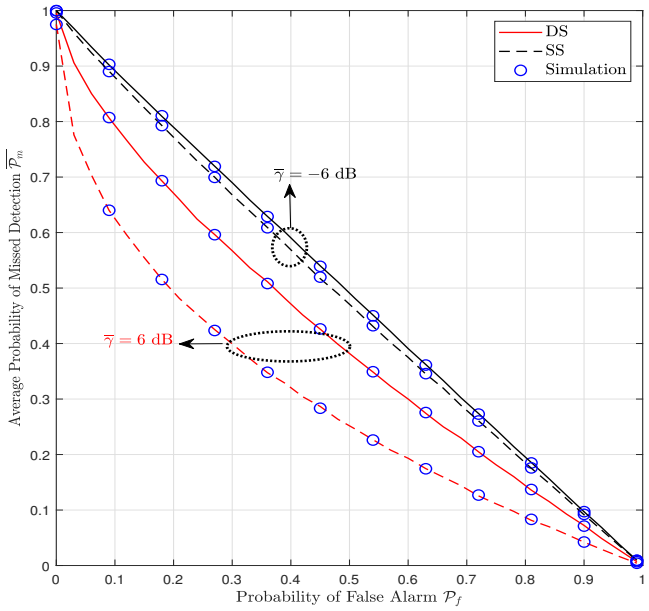

Figure 8.2: Complementary ROC curves for shadowed UAV-to-ground fading channels considering different $\overline{\gamma}$ values.

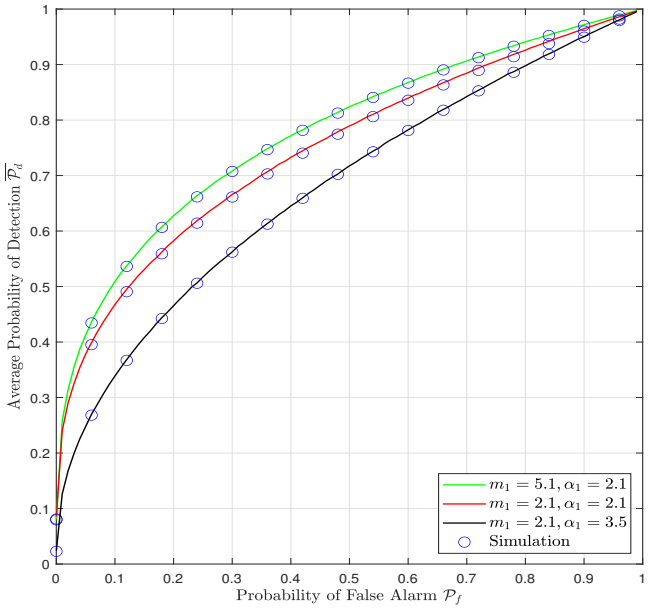

Figure 8.3: ROC curves for SS case considering different fading parameters.

In Figure 8.2, complementary ROC curves are plotted for various average SNR, $\overline{\gamma}$, values, with $u = 1$. The channel parameters were specifically chosen as follows: $m_1 = 3.4$, $m_2 = 3.5$, $= \alpha_1 = 3.8$, and $= \alpha_2 = 3.9$. Our analysis reveals that the DS case exhibits inferior performance compared to the SS case. This is due to the presence of shadowing around both the UAV and the base station in the former, while only one shadowing region exists in the latter. A notable trend observed is the enhancement in the performance of ED-based spectrum sensing with increasing average SNR, $\overline{\gamma}$, values.

In Figure 8.3, ROC curves illustrate the performance under various fading parameters for the SS case. An average SNR, $\overline{\gamma}$, of 5 dB is chosen, with $u = 1$ and $m_2 = m_1 + 0.4$. As α increases, shadowing intensifies, leading to a decrease in the average detection probability. Conversely, increasing m_1 implies a reduction in the multipath effect, consequently yielding a higher average detection probability. Importantly, all theoretical curves in this section utilize MATLAB's Meijer G-function and were verified and validated by Monte Carlo simulations.

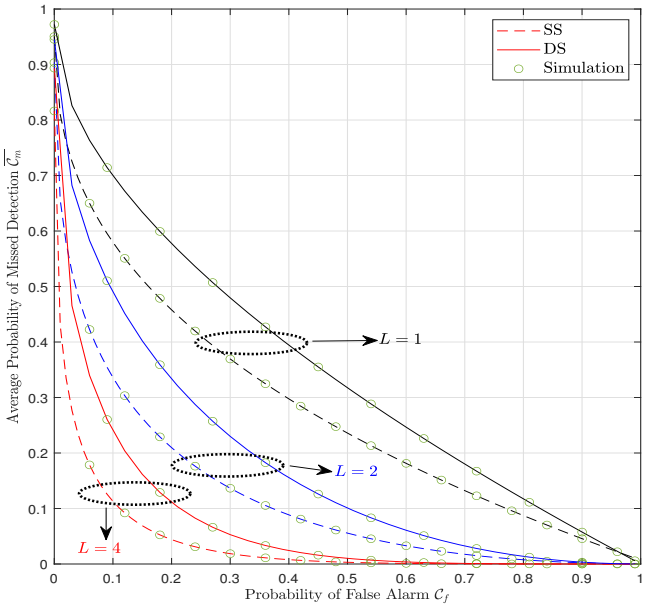

Figure 8.4: Complementary ROC curves for shadowed UAV-to-ground fading channels with different L SN.

Figure 8.4 illustrates the complementary ROC for ED performance, incorporating up to four collaborating SNs. The channel fading parameters were selected as ($m_1 = 2.5$,

$m_2 = 2.7$, $\alpha_1 = 2.5$, $\alpha_2 = 2.7$) with an average SNR of 5 dB and $u = 2$. As anticipated, the performance of the ED demonstrates significant enhancement with an increase in the number of SNs. Importantly, all theoretical curves in this section utilize MATLAB's Meijer G-function and were verified and validated by Monte Carlo simulations.

8.3 Conclusion

This chapter presents a thorough performance analysis of ED-based spectrum sensing over shadowed UAV-to-ground fading channels. Novel analytical expressions for the average detection probability were derived, which were further extended to incorporate collaborative spectrum sensing. To validate the analytical expressions proposed in this study, corresponding simulation results were also provided. Consequently, these derived expressions offer valuable insights into quantifying the impact of UAV-to-ground fading in ED spectrum sensing, thereby contributing to the enhancement of energy-efficient CR-based UAV communication systems.

Chapter 9

Conclusions and Future Work

9.1 Conclusions

In this thesis, we have explored some of the physical layer aspects of the shadowed UAV-to-ground channels as well as their performance across various system configurations. We have discussed the performance of these channels under different system configurations. Firstly, we analyzed the performance of a SISO communication system under these novel channels under the presence of AWGN and assuming perfect phase recovery at the Rx.

Then, we expanded our understanding by formulating closed-form expressions for the ABER of BPSK and QPSK as well as ASER of MPSK for digital communication systems operating in shadowed UAV-to-ground channels in the presence of imperfect phase recovery at the Rx. The results illustrated how the phase error led to a degraded error probability performance.

Furthermore, we have formulated closed-form expressions for the effective capacity and average channel capacity under various power adaptation strategies for UAV-to-ground fading channels. Then, the physical layer security parameters of these novel fading channels were examined in terms of ASC, SOP, and SPSC. This comprehensive analysis provides valuable insights into the reliability and security aspects of communication systems operating in aerial-to-ground environments.

Employing Rx diversity stands as a formidable technique to counteract the adverse impacts of fading in wireless communication systems. Therefore, we focused our studies on two distinct types of Rx diversity, MRC and SC. by utilizing the MGF of the PDF

of the received SNR, we have formulated open-form expressions for the ABER, channel capacity, outage probability, and ASER in the context of UAV-to-ground communication setups using MRC receivers. Utilizing the PDF and CDF expressions of the maximum received SNR, we established mathematical expressions for the outage probability, outage capacity, average channel capacity, and ABER expressions. Our results showed that MRC and SC diversity reception mechanisms hold the potential to enhance the performance of the communication system.

To enhance our understanding of system reliability and provide practical methods for evaluating and predicting performance in realistic environments, we derived closed-form and asymptotic expressions for calculating the outage probability of an interference-limited system operating over UAV-to-ground channels affected by shadowing. Additionally, we introduced the cascaded UAV-to-ground fading channel and conducted a detailed analysis of its statistical characteristics. This comprehensive examination allowed us to evaluate crucial performance metrics, including outage probability, average channel capacity, and ABER.

Furthermore, a performance analysis of ED-based spectrum sensing in shadowed UAV-to-ground fading channels. The derivation of new analytical expressions for the average detection probability, and their extension to collaborative spectrum sensing scenarios, provides a robust framework for improving the efficiency and reliability of spectrum sensing in UAV communications.

Overall, this thesis navigated through various physical layer aspects of UAV-to-ground communications. The findings presented in this thesis advance the theoretical understanding and practical implementation of UAV-to-ground communication systems. The novel expressions and performance analyses developed herein serve as valuable tools for researchers and engineers working to optimize UAV communication networks, ensuring enhanced performance and reliability in various applications.

9.2 Suggestions for Further Research

Communication involving UAVs continues to be a significant area of research. Advances in communication technology and the expanding use of UAVs in diverse applications are creating new opportunities for future studies in UAV communication. In this section, we

propose several possible directions for future research related to these novel UAV-to-ground channels.

1. **UAV relay-assisted communications**

   An essential application of UAVs in the telecommunications domain involves their role as mobile relay nodes, significantly enhancing network coverage. Acting as intermediaries, these relay nodes facilitate data transmission from source to destination. There are several types of relaying systems [128], among them are

   (a) *Amplify-and-forward (AF)* relaying technique, often referred to as regenerative relaying, entails a straightforward process where the relay amplifies the signal received from the source and subsequently transmits the amplified signal towards the destination. This approach offers a simplified form of relaying with minimal computational overhead and minimal delay. However, a key drawback is its inherent amplification of not only the signal but also the underlying intrinsic noise.

   (b) *Decode-and-Forward (DF)* relaying technique, often referred to as regenerative relaying, involves a specific sequence of operations at the relay node. Initially, the relay node decodes the information signal received from the source node. Subsequently, it undergoes a re-encoding process, where the decoded signal is re-modulated or re-encapsulated. Finally, the relay node forwards this processed signal to the intended destination node. This approach aims to achieve a lower error rate.

   While previous studies [129] have explored this scenario, they have not considered these novel channel models that validate empirical measurements. To ensure system reliability, it becomes imperative to characterize the statistical behavior of cascaded channels specifically, the ground-to-UAV and UAV-to-ground links. This characterization enables the evaluation of performance metrics such as fading severity, outage probability, average channel capacity, and ABER. We aim to provide a more comprehensive understanding of how these relay techniques perform within real-world scenarios by utilizing the novel shadowed fading models.

2. **RIS-assisted UAV communications**

   The concept of RIS involves a flat structure deliberately engineered to dynamically manipulate electromagnetic waves. Typically composed of an extensive array of

nearly passive deflecting components, an RIS can modify its response to electromagnetic waves using simple and cost-effective electronic circuits, such as PIN diodes or varactors. Conceptually, an RIS consists of numerous sub-wavelength antenna dipoles or segments of patch antennas, controllable via adaptable concentrated loads, allowing fine-tuning of the scattered electromagnetic field. When interacting with a plane wave, an RIS can redirect the wave towards a reflection direction different from the point of incidence. This capability enables steering the electromagnetic energy to specific locations, such as intended user positions. RIS holds the potential to enhance channel capacity, expand coverage, and reduce power consumption within upcoming 6G networks.

Mounting an RIS onto a UAV holds promise for extending coverage and enhancing communication capabilities. While the performance of RIS-aided UAV communications within shadowed fading channels has been investigated in [130], there are several open issues related to the physical layer security of RIS-aided UAV communications, such as cooperative jammer and resource optimization [67].

3. **Physical layer security of multi antenna-assisted UAV communications**

   In chapter 4, the analysis of physical layer security parameters focused on SISO transmission. One promising trends for future research involves exploring practical system configurations, such as employing multi-antenna Rxs within shadowed UAV networks. In such scenarios, the statistical expressions developed in Chapter 5 could prove invaluable for conducting thorough analyses.

APPENDICES

Appendix A

Meijer G-function

A.1 Definition

The Meijer G-function, named after its developer, Simon Meijer in 1936, is a special function in mathematics that generalizes many other special functions, such as the exponential, trigonometric, and hypergeometric functions. It's a complex-valued function defined by an integral representation involving gamma functions. The Meijer G-function is represented by the symbol

$$G_{p,q}^{m,n}\left(z\middle|\begin{matrix}\mathbf{a_p}\\ \mathbf{b_q}\end{matrix}\right) = G_{p,q}^{m,n}\left(z\middle|\begin{matrix}a_1,\ldots,a_n,a_{n+1},\ldots,a_p\\ b_1,\ldots,b_m,b_{m+1},\ldots,b_q\end{matrix}\right). \tag{A.1}$$

Details of the Meijer G-function can be found in [52], [131], [132], [133]. A general definition of the Meijer G-function is given by the line integral in the complex plane as

$$G_{p,q}^{m,n}\left(z\middle|\begin{matrix}\mathbf{a_p}\\ \mathbf{b_q}\end{matrix}\right) = \frac{1}{2\pi i}\int_L z^s \frac{\prod_{k=1}^{m}\Gamma(b_k-s)\prod_{k=1}^{n}\Gamma(1-a_k+s)}{\prod_{k=n+1}^{p}\Gamma(a_k-s)\prod_{k=m+1}^{q}\Gamma(1-b_k+s)}ds, \tag{A.2}$$

where

- $0 \le m \le q$ and $0 \le n \le p$, where m, n, p and q are integer numbers.
- L is the path from $-i\infty$ to $+i\infty$ where all the poles of $\Gamma(b_k-s)$ are to the right of the path and the poles of $\Gamma(1-a_k+s)$ are to the left.

Currently, it is a built-in function in several software packages such as MATLAB, Maple, and Mathematica.

A.2 Representation of other functions in terms of the Meijer G-function

$$e^x = G_{0,1}^{1,0}\left(-x\middle|\begin{matrix}-\\0\end{matrix}\right). \tag{A.3}$$

$$\ln(1+z) = G_{2,2}^{1,2}\left(z\middle|\begin{matrix}1,1\\1,0\end{matrix}\right). \tag{A.4}$$

$$(1+\gamma)^{-A} = \frac{1}{\Gamma(A)} G_{1,1}^{1,1}\left(\gamma\middle|\begin{matrix}1-A\\0\end{matrix}\right), \tag{A.5}$$

$${}_1F_1\left(a;b;-z\right) = \frac{\Gamma(b)}{\Gamma(a)} \times G_{1,2}^{1,1}\left(z\middle|\begin{matrix}1-a\\0,1-b\end{matrix}\right). \tag{A.6}$$

$$H_{p,q}^{m,n}\left(z\middle|\begin{matrix}(\mathbf{a_p},C)\\(\mathbf{b_q},C)\end{matrix}\right) = \frac{1}{C} G_{p,q}^{m,n}\left(z^{\frac{1}{C}}\middle|\begin{matrix}\mathbf{a_p}\\\mathbf{b_q}\end{matrix}\right). \tag{A.7}$$

$H_{p,q}^{m,n}\left(.\middle|.\right)$ is the Fox H-function whose MATLAB implementation can be found in [134].

A.3 Basic properties of the Meijer G-function

$$G_{p,q}^{m,n}\left(z\middle|\begin{matrix}\mathbf{a_p}\\\mathbf{b_q}\end{matrix}\right) = G_{q,p}^{n,m}\left(z^{-1}\middle|\begin{matrix}1-\mathbf{b_q}\\1-\mathbf{a_p}\end{matrix}\right). \tag{A.8}$$

$$z^{\kappa} G_{p,q}^{m,n}\left(z\middle|\begin{matrix}\mathbf{a_p}\\\mathbf{b_q}\end{matrix}\right) = G_{p,q}^{m,n}\left(z\middle|\begin{matrix}\mathbf{a_p}+\kappa\\\mathbf{b_q}+\kappa\end{matrix}\right). \tag{A.9}$$

A.4 Differentiation

$$\frac{\partial^u}{\partial z^u}[G_{p,q}^{m,n}\left(\frac{1}{z}\middle|\begin{matrix}\mathbf{a_p}\\\mathbf{b_q}\end{matrix}\right)] = (-1)^u z^{-u} G_{p+1,q+1}^{m,n+1}\left(\frac{1}{z}\middle|\begin{matrix}1-u,a_1,\ldots,a_n,a_{n+1},\ldots,a_p\\b_1,\ldots,b_m,1,b_{m+1},\ldots,b_q\end{matrix}\right). \tag{A.10}$$

A.5 Integration

$$\int_0^\infty z^{-\kappa} e^{-\beta x} G_{p,q}^{m,n}\left(\theta z \middle| \begin{matrix}\mathbf{a_p}\\ \mathbf{b_q}\end{matrix}\right) dz = \beta^{\kappa-1} G_{p+1,q}^{m,n+1}\left(\frac{\theta}{\beta}\middle| \begin{matrix}\kappa, \mathbf{a_p}\\ \mathbf{b_q}\end{matrix}\right). \tag{A.11}$$

$$\begin{aligned}\int_0^\infty \tau^{\zeta-1} G_{\sigma,\lambda}^{\mu,\nu}\left(\tau\omega \middle| \begin{matrix}\mathbf{c}_\sigma\\ \mathbf{d}_\lambda\end{matrix}\right) G_{p,q}^{m,n}\left(\tau z \middle| \begin{matrix}\mathbf{a_p}\\ \mathbf{b_q}\end{matrix}\right) d\tau = \omega^{-\zeta}\times \\ G_{p+\lambda,q+\sigma}^{m+\nu,n+\mu}\left(\frac{z}{\omega}\middle| \begin{matrix}a_1,\ldots,a_n,1-\zeta-\mathbf{d}_\lambda,a_{n+1},\ldots,a_p\\ b_1,\ldots,b_m,1-\zeta-\mathbf{c}_\sigma,b_{m+1},\ldots,b_q\end{matrix}\right).\end{aligned} \tag{A.12}$$

$$\int_0^y x^{\zeta-1} G_{p,q}^{m,n}\left(\omega x \middle| \begin{matrix}\mathbf{a_p}\\ \mathbf{b_q}\end{matrix}\right) dx = \omega^{-\zeta} \times G_{p+1,q+1}^{m+,n+1}\left(\omega y \middle| \begin{matrix}a_1,\ldots,a_n,1-\zeta,a_{n+1},\ldots,a_p\\ b_1,\ldots,b_m,-\zeta,b_{m+1},\ldots,b_q\end{matrix}\right). \tag{A.13}$$

$$\int_0^\infty x^{\zeta-1} G_{p,q}^{m,n}\left(\omega x \middle| \begin{matrix}\mathbf{a_p}\\ \mathbf{b_q}\end{matrix}\right) dx = \omega^{-\zeta} \times \frac{\prod_{k=1}^m \Gamma(\zeta+b_k)\prod_{k=1}^n \Gamma(1-\zeta-a_k)}{\prod_{k=n+1}^p \Gamma(\zeta+a_k)\prod_{k=m+1}^q \Gamma(1-\zeta-b_k)}. \tag{A.14}$$

$$\begin{aligned}\int_0^\infty \tau^{\zeta-1} G_{\delta,\eta}^{\alpha,\beta}\left(\tau z \middle| \begin{matrix}\mathbf{E}_\delta\\ \mathbf{F}_\eta\end{matrix}\right) G_{\sigma,\lambda}^{\mu,\nu}\left(\tau x \middle| \begin{matrix}\mathbf{c}_\sigma\\ \mathbf{d}_\lambda\end{matrix}\right) G_{p,q}^{m,n}\left(\tau y \middle| \begin{matrix}\mathbf{a_p}\\ \mathbf{b_q}\end{matrix}\right) d\tau = z^{-\zeta}\times \\ G_{\eta,\delta:\sigma,\lambda:p,q}^{\beta,\alpha:\mu,\nu:m,n}\left(\frac{x}{z},\frac{y}{z}\middle| \begin{matrix}1-\zeta-\mathbf{F}_\eta\\ 1-\zeta-\mathbf{E}_\delta\end{matrix}\middle| \begin{matrix}\mathbf{c}_\sigma\\ \mathbf{d}_\lambda\end{matrix}\middle| \begin{matrix}\mathbf{a_p}\\ \mathbf{b_q}\end{matrix}\right).\end{aligned} \tag{A.15}$$

$G(.,.|.|.|.)$ is the Bivariate Meijer G-function whose MATLAB implementation of can be found in [109].

A.6 Asymptotic Expansion

At sufficiently large values of its argument, the Meijer's G function can be expressed using elementary functions as [135, Eq. (17)]

$$\lim_{x\to\infty+} G_{p,q}^{m,n}\left(z\middle| \begin{matrix}\mathbf{a_p}\\ \mathbf{b_q}\end{matrix}\right) = \sum_{k=1}^n z^{a_k-1} \frac{\prod_{l=1,l\neq k}^n \Gamma(a_k-a_l)\prod_{l=1}^m \Gamma(1+b_l-a_k)}{\prod_{l=n+1}^p \Gamma(1+a_l-a_k)\prod_{l=m+1}^q \Gamma(a_k-b_l)}, \tag{A.16}$$

where $a_k - a_l \neq 0, \pm1, \pm2, \cdots$ and $a_k - b_l \neq, 1, 2, \cdots$.

Appendix B

Proof of DS PDF

In this appendix, we provide the mathematical proof of the DS PDF provided in (2.6). As mentioned before, the received SNR can be modeled as

$$\gamma = N_1^2 I_1 N_2^2 I_2, \tag{B.1}$$

where

- $N_j - j \in \{1, 2\}-$ represents the multipath fading coefficient which follows the Nakagami-m distribution [48]. The PDF of ${N_j}^2$ can be written as

$$f_{{N_j}^2}(x) = \frac{{m_j}^{m_j} x^{m_j - 1}}{{\Omega_j}^{m_j} \Gamma(m_j)} e^{-\frac{m_j x}{\Omega_j}}, \tag{B.2}$$

  where the distribution's shaping parameter m_j is the fading severity parameter, $\Omega_j = 1/m_j$ is the scale parameter, and $\Gamma(.)$ is the gamma function. A plot of the PDF of ${N_j}^2$ can be found in Figure B.1.

- I_j represents the shadowing effect of the channel, modeled by the inverse-gamma distribution [50], whose PDF can be written as

$$f_{I_j}(x) = \frac{{\overline{\gamma}_j}^{\alpha_j}}{x^{\alpha_j + 1} \Gamma(\alpha_j)} e^{-\frac{\overline{\gamma}_j}{x}}, \tag{B.3}$$

  where the shaping parameter of the distribution $\alpha_j > 1$ represents the severity of the shadowing and $\overline{\gamma}$ denotes the scaling parameter. A plot of the inverse-gamma PDF can be found in Figure B.2.

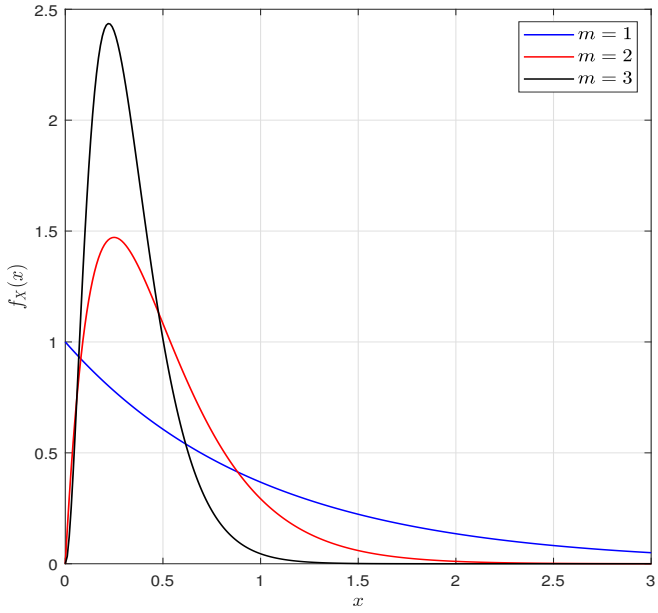

Figure B.1: PDF of ${N_j}^2$ distribution.

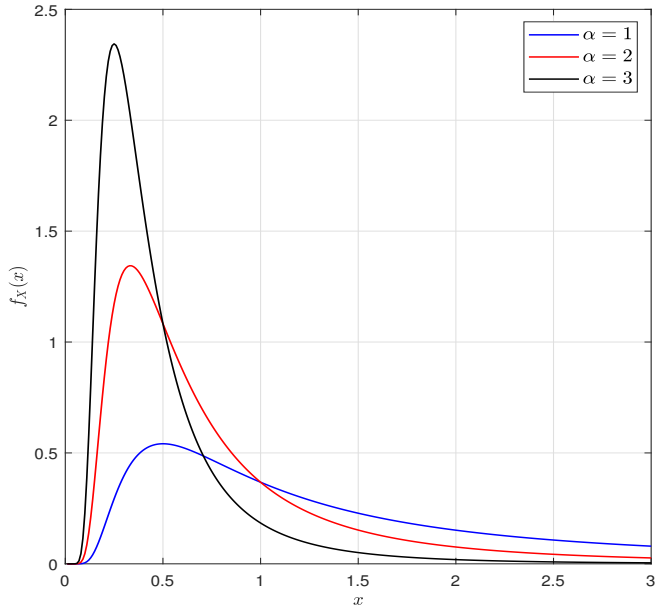

Figure B.2: PDF of inverse gamma distribution ($\overline{\gamma} = 1$).

If we select $\overline{\gamma}_1 = \overline{\gamma}_2 = 1$, (B.1) and (B.3) can be re-written as

$$\gamma_u = N_1^2 I_1 N_2^2 I_2, \tag{B.4}$$

where

$$f_{I_j}(x) = \frac{1}{x^{\alpha_j+1}\Gamma(\alpha_j)} e^{-\frac{1}{x}}. \tag{B.5}$$

Now, we can convert the exponential function into the Meijer G-function using (A.3) as

$$f_{I_j}(x) = \frac{1}{x^{\alpha_j+1}\Gamma(\alpha_j)} G_{0,1}^{1,0}\left(\frac{1}{x}\middle|\begin{matrix}-\\0\end{matrix}\right). \tag{B.6}$$

With the help of (A.9), (B.6) can be written as

$$f_{I_j}(x) = \frac{1}{\Gamma(\alpha_j)} G_{0,1}^{1,0}\left(\frac{1}{x}\middle|\begin{matrix}-\\1+\alpha_j\end{matrix}\right). \tag{B.7}$$

With the help of (A.8), (B.7) can be written as

$$f_{I_j}(x) = \frac{1}{\Gamma(\alpha_j)} G_{1,0}^{0,1}\left(x\middle|\begin{matrix}-\alpha_j\\-\end{matrix}\right). \tag{B.8}$$

Thus, (B.8) can be converted into the Fox-H-function as

$$f_{I_j}(x) = \frac{1}{\Gamma(\alpha_j)} H_{1,0}^{0,1}\left(x\middle|\begin{matrix}(-\alpha_j,1)\\-\end{matrix}\right). \tag{B.9}$$

Thus, $I = I_1 I_2$ is a random variable that is the product of 2 Fox H random variables. The PDF of I can be expressed as [116]

$$f_{I_j}(x) = \frac{1}{\Gamma(\alpha_1)\Gamma(\alpha_2)} H_{2,0}^{0,2}\left(x\middle|\begin{matrix}(-\alpha_1,1),(-\alpha_2,1)\\-\end{matrix}\right). \tag{B.10}$$

Now, $N = {N_1}^2 {N_2}^2$ is a random variable that is the product of 2 gamma-distributed random variables. The PDF of N can be expressed as [136]

$$f_N(y) = \frac{y^{-1}}{\Gamma(m_1)\Gamma(m_2)} G_{0,2}^{2,0}\left(m_1 m_2 y\middle|\begin{matrix}-\\m_1, m_2\end{matrix}\right). \tag{B.11}$$

With the help of (A.9), (B.11) can be written as

$$f_N(y) = \frac{m_1 m_2}{\Gamma(m_1)\Gamma(m_2)} G_{0,2}^{2,0}\left(m_1 m_2 y \middle| \begin{matrix} - \\ m_1 - 1, m_2 - 1 \end{matrix} \right). \tag{B.12}$$

Thus, (B.12) can be converted into the Fox H-function as

$$f_N(y) = \frac{m_1 m_2}{\Gamma(m_1)\Gamma(m_2)} H_{0,2}^{2,0}\left(m_1 m_2 y \middle| \begin{matrix} - \\ (m_1 - 1, 1), (m_2 - 1, 1) \end{matrix} \right). \tag{B.13}$$

Thus, $\gamma_u = I \times N$ is a random variable that is the product of 2 Fox-H random variables. The PDF of γ_u can be expressed as [116]

$$f_{\gamma_u}(\gamma_u) = \frac{m_1 m_2}{\Gamma(m_1)\Gamma(m_2)\Gamma(\alpha_1)\Gamma(\alpha_2)} H_{0,2}^{2,0}\left(m_1 m_2 \gamma_u \middle| \begin{matrix} (-\alpha_1, 1), (-\alpha_2, 1) \\ (m_1 - 1, 1), (m_2 - 1, 1) \end{matrix} \right). \tag{B.14}$$

Thus, (B.14) can be converted to Meijer-G function as

$$f_{\gamma_u}(\gamma_u) = \frac{m_1 m_2}{\Gamma(m_1)\Gamma(m_2)\Gamma(\alpha_1)\Gamma(\alpha_2)} G_{0,2}^{2,0}\left(m_1 m_2 \gamma_u \middle| \begin{matrix} -\alpha_1, -\alpha_2 \\ m_1 - 1, m_2 - 1 \end{matrix} \right). \tag{B.15}$$

For a general SNR value, $\gamma = \overline{\gamma}\gamma_u$, its PDF can be evaluated as

$$f_\gamma(\gamma) = \frac{m_1 m_2}{\overline{\gamma}\Gamma(m_1)\Gamma(m_2)\Gamma(\alpha_1)\Gamma(\alpha_2)} G_{2,2}^{2,2}\left(\frac{m_1 m_2}{\overline{\gamma}} \gamma \middle| \begin{matrix} -\alpha_2, -\alpha_1 \\ m_1 - 1, m_2 - 1 \end{matrix} \right) \tag{B.16}$$

With the help of (A.9), the PDF of the received SNR, γ, can be expressed as [34]

$$f_\gamma(\gamma) = \gamma^{-1} \mathbb{S}_{DS} G_{2,2}^{2,2}\left(\frac{m_1 m_2}{\overline{\gamma}} \gamma \middle| \begin{matrix} 1 - \alpha_2, 1 - \alpha_1 \\ m_1, m_2 \end{matrix} \right), \tag{B.17}$$

where $\mathbb{S}_{DS} = \frac{1}{\Gamma(m_1)\Gamma(m_2)\Gamma(\alpha_1)\Gamma(\alpha_2)}$.

A similar approach can be employed in order to derive the PDF of the SS case as expressed in (2.17).

Appendix C

Proof of CDF Approach

In this appendix, we provide the mathematical proof of the CDF approach provided in (2.33). The Q-function, $Q(.)$, can be expressed in terms of the complementary error function erfc(.) as

$$Q(x) = \frac{1}{2}\text{erfc}\left(\frac{x}{\sqrt{2}}\right). \tag{C.1}$$

Thus, the conditional probability of error for BPSK can be expressed as

$$P_b(x) = Q(\sqrt{2x}) = \frac{1}{2}\text{erfc}\left(\sqrt{x}\right). \tag{C.2}$$

Similarly, the conditional probability of error for BFSK can be expressed as

$$P_b(x) = Q(\sqrt{x}) = \frac{1}{2}\text{erfc}\left(\sqrt{\frac{x}{2}}\right). \tag{C.3}$$

Thus, it can be generalized as

$$P_b(x) = \frac{1}{2}\text{erfc}\left(\sqrt{\kappa x}\right), \tag{C.4}$$

where $\kappa = 1$ for BPSK and $\kappa = 0.5$ for BFSK. The erfc(.) can be expressed in terms of the lower incomplete gamma function, $\gamma(.,.)$, as

$$\gamma\left(\frac{1}{2}, x\right) = \sqrt{\pi}\text{erfc}\left(\sqrt{x}\right), \tag{C.5}$$

where the lower incomplete gamma function [137] is defined as

$$\gamma\left(s,x\right)=\int_{0}^{x}t^{s-1}e^{-t}dt. \tag{C.6}$$

Thus, the conditional probability of error can be expressed as

$$P_b(x)=\frac{1}{2}\text{erfc}\left(\sqrt{\kappa x}\right)=\frac{1}{2\sqrt{\pi}}\gamma\left(\frac{1}{2},\kappa x\right)=\frac{1}{2\Gamma(\beta)}\gamma\left(\beta,\kappa x\right), \tag{C.7}$$

where $\beta=0.5$. In this case, the integration in (C.6) can be evaluated as

$$\gamma\left(\beta,\kappa x\right)=\int_{0}^{\kappa x}t^{\beta-1}e^{-t}dt.=\kappa\int_{0}^{y}(\kappa y)^{\beta-1}e^{-\kappa y}dy. \tag{C.8}$$

The unconditional probability of error can be evaluated as

$$\begin{aligned}P_{\text{BER}}&=\int_{0}^{\infty}P_b(x)f_\gamma(\gamma)d\gamma.\\&=\frac{\kappa^\beta}{2\Gamma(\beta)}\int_{0}^{\infty}\int_{0}^{\gamma}(\gamma)^{\beta-1}e^{-\kappa\gamma}f_\gamma(\gamma)d\gamma d\gamma\\&=\frac{\kappa^\beta}{2\Gamma(\beta)}\int_{0}^{\infty}(\gamma)^{\beta-1}e^{-\kappa\gamma}F_\gamma(\gamma)d\gamma.\end{aligned} \tag{C.9}$$

Appendix D

Publications

Below is a list of publications that have been published or submitted that are relevant to this thesis:

D.1 Journal Publications

1. **R. Polus** and C. D'Amours. "Error Probability of Shadowed UAV-to-Ground Channels with Imperfect Carrier Phase Recovery," *IEEE Commun. Lett.*, vol. 28, no. 3, pp. 692 - 696, 2024..

2. **R. Polus** and C. D'Amours, "Capacity Analysis of UAV-to-Ground Channels with Shadowing: Power Adaptation Schemes and Effective Capacity," *IEEE Open J. Veh. Technol.*, vol. 5, pp. 71 - 77, 2024.

3. **R. Polus** and C. D'Amours, "On the Performance of MRC Receivers in UAV-to-Ground Channels with Shadowing," *IEEE Wireless Commun. Lett.*, vol. 12, no. 7, pp. 1249 - 1253, 2023.

D.2 Conference Publications

4. **R. Polus** and C. D'Amours, "Cascaded Shadowed UAV-to-Ground Channels," accepted in *Proc. IEEE 10th World Forum Internet Things (WF-IoT)*, Nov 2024, pp. 1–6.

5. **R. Polus** and C. D'Amours, "On the Reliability of Interference-Limited Systems over UAV-to-Ground Channels with Shadowing," accepted in *Proc. IEEE 10th World Forum Internet Things (WF-IoT)*, Nov 2024, pp. 1–6.

6. **R. Polus** and C. D'Amours, "Energy Detection-based Spectrum Sensing over Shadowed UAV-to-Ground Channels," *Proc. IEEE 100th Veh. Technol. Conf. (VTC-Fall)*, Oct. 2024, pp. 1–5.

7. **R. Polus**, C. D'Amours, and B. Kantarci, "Physical Layer Security over UAV-to-Ground Channels with Shadowing," in *Proc. IEEE 97th Veh. Technol. Conf. (VTC-Spring)*, June 2023, pp. 1–5.

8. **R. Polus** and C. D'amours, "Performance Analysis of Selection Combining over UAV-to-Ground Channels with Shadowing," in *Proc. IEEE 97th Veh. Technol. Conf. (VTC-Spring)*, June 2023, pp. 1–5.

References

[1] A. Gupta and R. K. Jha, "A survey of 5G network: Architecture and Emerging Technologies," *IEEE Access*, vol. 3, pp. 1206–1232, 2015.

[2] K. David and H. Berndt, "6G Vision and Requirements: Is There Any Need for Beyond 5G?" *IEEE Veh. Technol. Mag.*, vol. 13, no. 3, pp. 72–80, 2018.

[3] I. F. Akyildiz, D. M. Gutierrez-Estevez, and E. C. Reyes, "The Evolution to 4G Cellular Systems: LTE-Advanced," *Phys. Commun.*, vol. 3, no. 4, pp. 217–244, 2010.

[4] P. Popovski, K. F. Trillingsgaard, O. Simeone, and G. Durisi, "5G Wireless Network Slicing for eMBB, URLLC, and mMTC: A Communication-Theoretic View," *IEEE Access*, vol. 6, pp. 55 765–55 779, 2018.

[5] C. Bockelmann, N. Pratas, H. Nikopour, K. Au, T. Svensson, C. Stefanovic, P. Popovski, and A. Dekorsy, "Massive Machine-Type Communications in 5G: Physical and MAC-Layer Solutions," *IEEE Commun. Mag.*, vol. 54, no. 9, pp. 59–65, 2016.

[6] A. Yadav and O. A. Dobre, "All Technologies Work Together for Good: A Glance at Future Mobile Networks," *IEEE Wirel. Commun.*, vol. 25, no. 4, pp. 10–16, 2018.

[7] X. Lin, J. Li, R. Baldemair, J.-F. T. Cheng, S. Parkvall, D. C. Larsson, H. Koorapaty, M. Frenne, S. Falahati, A. Grovlen *et al.*, "5G New Radio: Unveiling the Essentials of the Next Generation Wireless Access Technology," *IEEE Commun. Stand. Mag.*, vol. 3, no. 3, pp. 30–37, 2019.

[8] W. Chen, J. Montojo, J. Lee, M. Shafi, and Y. Kim, "The Standardization of 5G-Advanced in 3GPP," *IEEE Commun. Mag.*, vol. 60, no. 11, pp. 98–104, 2022.

[9] X. Lin, "An Overview of 5G Advanced Evolution in 3GPP Release 18," *IEEE Commun. Stand. Mag.*, vol. 6, no. 3, pp. 77–83, 2022.

[10] H. Tataria, M. Shafi, A. F. Molisch, M. Dohler, H. Sjöland, and F. Tufvesson, "6G Wireless Systems: Vision, Requirements, Challenges, Insights, and Opportunities," *Proc. IEEE*, vol. 109, no. 7, pp. 1166–1199, 2021.

[11] R. Liu, H. Lin, H. Lee, F. Chaves, H. Lim, and J. Sköld, "Beginning of the journey toward 6G: Vision and framework," *IEEE Commun. Mag.*, vol. 61, no. 10, pp. 8–9, 2023.

[12] F. Tariq, M. R. Khandaker, K.-K. Wong, M. A. Imran, M. Bennis, and M. Debbah, "A Speculative Study on 6G," *IEEE Wirel. Commun.*, vol. 27, no. 4, pp. 118–125, 2020.

[13] Z. Zhang, Y. Xiao, Z. Ma, M. Xiao, Z. Ding, X. Lei, G. K. Karagiannidis, and P. Fan, "6G Wireless Networks: Vision, Requirements, Architecture, and Key Technologies," *IEEE Veh. Technol. Mag.*, vol. 14, no. 3, pp. 28–41, 2019.

[14] I. F. Akyildiz, A. Kak, and S. Nie, "6G and Beyond: The Future of Wireless Communications Systems," *IEEE Access*, vol. 8, pp. 133 995–134 030, 2020.

[15] W. Saad, M. Bennis, and M. Chen, "A Vision of 6G Wireless Systems: Applications, Trends, Technologies, and Open Research Problems," *IEEE Netw.*, vol. 34, no. 3, pp. 134–142, 2019.

[16] G. T. 38.821, "Solutions for NR to support non-terrestrial networks (NTN)," 2019.

[17] O. B. Osoro and E. J. Oughton, "A Techno-Economic Framework for Satellite Networks Applied to Low Earth Orbit Constellations: Assessing Starlink, OneWeb and Kuiper," *IEEE Access*, vol. 9, pp. 141 611–141 625, 2021.

[18] M. Mozaffari, W. Saad, M. Bennis, Y.-H. Nam, and M. Debbah, "A Tutorial on UAVs for Wireless Networks: Applications, Challenges, and Open Problems," *IEEE Commun. Surv. Tutor.*, vol. 21, no. 3, pp. 2334–2360, 2019.

[19] N. Parvaresh, M. Kulhandjian, H. Kulhandjian, C. D'Amours, and B. Kantarci, "A Tutorial on AI-powered 3D Deployment of Drone Base Stations: State of the Art, Applications and Challenges," *Veh. Commun.*, vol. 36, no. 100474, 2022.

[20] Y. Zeng, Q. Wu, and R. Zhang, "Accessing From the Sky: A Tutorial on UAV Communications for 5G and Beyond," *Proc. IEEE*, vol. 107, no. 12, pp. 2327–2375, 2019.

[21] X. Jiang, M. Sheng, Z. Nan, X. Chengwen, L. Weidang, and W. Xianbin, "Green UAV Communications for 6G: A Survey," *Chin. J. Aeronaut.*, vol. 35, no. 9, pp. 19–34, 2022.

[22] S. Hafeez, A. R. Khan, M. Al-Quraan, L. Mohjazi, A. Zoha, M. A. Imran, and Y. Sun, "Blockchain-Assisted UAV Communication Systems: A Comprehensive Survey," *IEEE Open J. Veh. Technol.*, 2023.

[23] J. Mu, R. Zhang, Y. Cui, N. Gao, and X. Jing, "UAV Meets Integrated Sensing and Communication: Challenges and Future Directions," *IEEE Commun. Mag.*, vol. 61, no. 5, pp. 62–67, 2023.

[24] B. Yang, T. L. Hawthorne, M. Hessing-Lewis, E. J. Duffy, L. Y. Reshitnyk, M. Feinman, and H. Searson, "Developing an Introductory UAV/Drone Mapping Training Program for Seagrass Monitoring and Research," *Drones*, vol. 4, no. 70, 2020.

[25] N. H. Motlagh, P. Kortoçi, X. Su, L. Lovén, H. K. Hoel, S. B. Haugsvær, V. Srivastava, C. F. Gulbrandsen, P. Nurmi, and S. Tarkoma, "Unmanned Aerial Vehicles for Air Pollution Monitoring: A survey," *IEEE Internet Things J.*, 2023.

[26] A. S. Abdalla and V. Marojevic, "Communications Standards for Unmanned Aircraft Systems: The 3GPP Perspective and Research Drivers," *IEEE Commun. Stand. Mag.*, vol. 5, no. 1, pp. 70–77, 2021.

[27] " 3GPP TR 33.677. 3rd Generation Partnership Project; Enhancement for Unmanned Aerial Vehicles (UAVs)," 2017.

[28] "3GPP TS 22.125. 3rd Generation Partnership Project; Unmanned Aerial System (UAS) support in 3GPP," 2021.

[29] "3GPP TR 22.825. 3rd Generation Partnership Project; Study on Remote Identification of Unmanned Aerial Systems (UAS) ," 2018.

[30] "3GPP TR 22.829. 3rd Generation Partnership Project; Enhancement for Unmanned Aerial Vehicles (UAVs)," 2019.

[31] "3GPP TR 23.754. 3rd Generation Partnership Project; Study on supporting Unmanned Aerial Systems (UAS) connectivity, Identification and tracking," 2021.

[32] "3GPP TR 23.755. 3rd Generation Partnership Project; Study on application layer support for Unmanned Aerial Systems (UAS)," 2021.

[33] C. You and R. Zhang, "3D Trajectory Optimization in Rician Fading for UAV-Enabled Data Harvesting," *IEEE Trans. Wirel. Commun.*, vol. 18, no. 6, pp. 3192–3207, 2019.

[34] P. S. Bithas, V. Nikolaidis, A. G. Kanatas, and G. K. Karagiannidis, "UAV-to-Ground Communications: Channel Modeling and UAV Selection," *IEEE Trans. Commun.*, vol. 68, no. 8, pp. 5135–5144, 2020.

[35] P. S. Bithas, V. Nikolaidis, and A. G. Kanatas, "A new shadowed double-scattering model with application to UAV-to-ground communications," in *Proc. IEEE Wireless Commun. Netw. Conf. (WCNC)*, Apr. 2019, pp. 1–6.

[36] D. Dixit, N. Kumar, S. Sharma, V. Bhatia, S. Panic, and C. Stefanovic, "On the ASER Performance of UAV-Based Communication Systems for QAM Schemes," *IEEE Commun. Lett.*, vol. 25, no. 6, pp. 1835–1838, 2021.

[37] X. Sun, D. W. K. Ng, Z. Ding, Y. Xu, and Z. Zhong, "Physical Layer Security in UAV Systems: Challenges and Opportunities," *IEEE Wirel. Commun.*, vol. 26, no. 5, pp. 40–47, 2019.

[38] B. K. S. Lima, A. S. de Sena, R. Dinis, D. B. Da Costa, M. Beko, R. Oliveira, and M. Debbah, "Aerial Intelligent Reflecting Surfaces in MIMO-NOMA Networks: Fundamentals, Potential Achievements, and Challenges," *IEEE Open J. Commun. Soc.*, vol. 3, pp. 1007–1024, 2022.

[39] Y. Zeng, J. Lyu, and R. Zhang, "Cellular-connected UAV: Potential, challenges, and promising technologies," *IEEE Wirel. Commun.*, vol. 26, no. 1, pp. 120–127, 2018.

[40] W. Khawaja, I. Guvenc, D. W. Matolak, U.-C. Fiebig, and N. Schneckenburger, "A Survey of Air-to-Ground Propagation Channel Modeling for Unmanned Aerial Vehicles," *IEEE Commun. Surv. Tutor.*, vol. 21, no. 3, pp. 2361–2391, 2019.

[41] Y. Zeng, I. Guvenc, R. Zhang, G. Geraci, and D. W. Matolak, *UAV Communications for 5G and Beyond*, 1st ed. John Wiley & Sons, 2020.

[42] B. Kerczewski, "Spectrum for UAS control and Non-Payload Communications," in *Proc. Integr. Commun., Navigat., Surveill. Conf. (ICNS)*, Apr. 2013, pp. 1–21.

[43] A. A. Khuwaja, Y. Chen, N. Zhao, M.-S. Alouini, and P. Dobbins, "A Survey of Channel Modeling for UAV Communications," *IEEE Commun. Surv. Tutor.*, vol. 20, no. 4, pp. 2804–2821, 2018.

[44] C. Yan, L. Fu, J. Zhang, and J. Wang, "A Comprehensive Survey on UAV Communication Channel Modeling," *IEEE Access*, vol. 7, pp. 107 769–107 792, 2019.

[45] H. Ni, Q. Zhu, B. Hua, K. Mao, Y. Pan, F. Ali, W. Zhong, and X. Chen, "Path loss and shadowing for UAV-to-ground UWB channels incorporating the effects of built-up areas and airframe," *IEEE Trans. Intell. Transp. Syst.*, 2024.

[46] V. Nikolaidis, N. Moraitis, and A. G. Kanatas, "Dual-Polarized Narrowband MIMO LMS Channel Measurements in Urban Environments," *IEEE Trans. Antennas Propag.*, vol. 65, no. 2, pp. 763–774, 2016.

[47] P. S. Chauhan, S. Kumar, A. Jain, and L. Hanzo, "An Asymptotic Framework for Fox's H-Fading Channel with Application to Diversity-Combining Receivers," *IEEE Open J. Veh. Technol.*, vol. 4, pp. 404–416, 2023.

[48] M. Nakagami, "The m-distribution—A General Formula of Intensity Distribution of Rapid Fading," in *Statistical Methods in Radio Wave Propagation*, 1960, pp. 3–36.

[49] A. Goldsmith, *Wireless Communications*, 1st ed. New York, NY: Cambridge University Press, 2005.

[50] V. Witkovskỳ, "Computing the Distribution of A Linear Combination of Inverted Gamma Variables," *Kybernetika*, vol. 37, pp. 79–90, 2001.

[51] R. Maurya, S. Srivastava, P. S. Chauhan, S. Singh, and S. K. Soni, "Development of Analytical Model for Energy Detectors with SC and MRC Diversity over Inverse-Gamma Fading," *Int. J. Commun. Syst.*, vol. 33, no. 8, p. e4353, 2020.

[52] I. S. Gradshteyn and I. M. Ryzhik, *Table of Integrals, Series, and Products*, 8th ed. San Diego, CA: Academic Press, 2014.

[53] M. K. Simon and M.-S. Alouini, *Digital Communication over Fading Channels*, 2nd ed. Hoboken, NJ: Wiley, 2001.

[54] J. M. Romero-Jerez, F. J. Lopez-Martinez, J. F. Paris, and A. J. Goldsmith, "The Fluctuating Two-Ray Fading Model: Statistical Characterization and Performance Analysis," *IEEE Trans. Wirel. Commun.*, vol. 16, no. 7, pp. 4420–4432, 2017.

[55] C. E. Shannon, "A Mathematical Theory of Communication," *Bell Labs Tech. J.*, vol. 27, no. 3, pp. 379–423, 1948.

[56] J. Zhang, W. Zeng, X. Li, Q. Sun, and K. P. Peppas, "New Results on the Fluctuating Two-Ray Model With Arbitrary Fading Parameters and Its Applications," *IEEE Trans. Veh. Technol.*, vol. 67, no. 3, pp. 2766–2770, 2017.

[57] A. J. Viterbi, *Principles of Coherent Communication*, 1st ed. New York, NY: McGraw-Hill series in systems science, 1966.

[58] A. Siddig, A. Al-Dweik, A. Al-Rimawi, Y. Iraqi, A. Pandey, and J.-P. Giacalone, "On the Performance of IRS-Assisted IoT-NTN With Joint Imperfect Phase Estimation and Quantization," *IEEE Open J. Commun. Soc.*, 2023.

[59] W. Weber, "Performance of Phase-Locked Loops in the Presence of Fading Communication Channels," *IEEE Trans. Commun.*, vol. 24, no. 5, pp. 487–499, 1976.

[60] C. Lo and W. Lam, "Error Probability of Binary Phase Shift Keying in Nakagami-m Fading Channel with Phase Noise," *Electron. Lett.*, vol. 36, no. 21, pp. 1773–1774, 2000.

[61] P. E. Silva, R. A. de Souza, M. D. Yacoub, D. B. da Costa, and J. M. Moualeu, "Error Probability of α-μ Fading Channels with Imperfect Carrier Phase Recovery," in *Proc. IEEE 90th Veh. Technol. Conf. (VTC-Fall)*, Sept. 2019, pp. 1–5.

[62] A. Chandra, A. Patra, and C. Bose, "Performance Analysis of PSK Systems with Phase Error in Fading Channels: A Survey," *Phys. Commun.*, vol. 4, no. 1, pp. 63–82, 2011.

[63] M. Smadi, M. Ababneh, and S. Al-Jazzar, "Simulation and Numerical Analysis of Wireless PSK Systems with Imperfect Carrier Phase Recovery," *Int. J. Model. Simul.*, vol. 29, no. 4, pp. 405–409, 2009.

[64] P. Jain and N. Blachman, "Detection of a PSK signal transmitted through a hard-limited channel," *IEEE Trans. Inf. Theory*, vol. 19, no. 5, pp. 623–630, 1973.

[65] P. E. Silva, R. A. de Souza, D. B. da Costa, J. M. Moualeu, and M. D. Yacoub, "Error Probability of M-Phase Signaling with Phase Noise over Fading Channels," *IEEE Trans. Veh. Technol.*, vol. 69, no. 6, pp. 6766–6770, 2020.

[66] A. D. Wyner, "The Wire-Tap Channel," *Bell Labs Tech. J.*, vol. 54, no. 8, pp. 1355–1387, 1975.

[67] W. U. Khan, E. Lagunas, Z. Ali, M. A. Javed, M. Ahmed, S. Chatzinotas, B. Ottersten, and P. Popovski, "Opportunities for Physical Layer Security in UAV Communication Enhanced with Intelligent Reflective Surfaces," *IEEE Wirel. Commun.*, vol. 29, no. 6, pp. 22–28, 2022.

[68] A. J. Goldsmith and P. P. Varaiya, "Capacity of Fading Channels with Channel Side Information," *IEEE Trans. Inf. Theory*, vol. 43, no. 6, pp. 1986–1992, 1997.

[69] M.-S. Alouini and A. J. Goldsmith, "Capacity of Rayleigh Fading Channels Under Different Adaptive Transmission and Diversity-Combining Techniques," *IEEE Trans. Veh. Technol.*, vol. 48, no. 4, pp. 1165–1181, 1999.

[70] Y. Abo Rahama, M. H. Ismail, and M. S. Hassan, "Capacity of Fox's H-Function Fading Channel with Adaptive Transmission," *Electron. Lett.*, vol. 52, no. 11, pp. 976–978, 2016.

[71] D. Wu and R. Negi, "Effective Capacity: A Wireless Link Model for Support of Quality of Service," *IEEE Trans. Wirel. Commun.*, vol. 2, no. 4, pp. 630–643, 2003.

[72] S. K. Yoo, S. L. Cotton, P. C. Sofotasios, S. Muhaidat, and G. K. Karagiannidis, "Effective Capacity Analysis over Generalized Composite Fading Channels," *IEEE Access*, vol. 8, pp. 123 756–123 764, 2020.

[73] A. K. Yerrapragada, T. Eisman, and B. Kelley, "Physical Layer Security for Beyond 5G: Ultra Secure Low Latency Communications," *IEEE Open J. Commun. Soc.*, vol. 2, pp. 2232–2242, 2021.

[74] H.-M. Wang, X. Zhang, and J.-C. Jiang, "UAV-Involved Wireless Physical-Layer Secure Communications: Overview and Research Directions," *IEEE Wirel. Commun.*, vol. 26, no. 5, pp. 32–39, 2019.

[75] N. Wang, P. Wang, A. Alipour-Fanid, L. Jiao, and K. Zeng, "Physical-Layer Security of 5G Wireless Networks for IoT: Challenges and Opportunities," *IEEE Internet Things J.*, vol. 6, no. 5, pp. 8169–8181, 2019.

[76] J. M. Hamamreh, H. M. Furqan, and H. Arslan, "Classifications and Applications of Physical Layer Security Techniques for Confidentiality: A Comprehensive Survey," *IEEE Commun. Surv. Tutor.*, vol. 21, no. 2, pp. 1773–1828, 2018.

[77] W. Trappe, "The Challenges Facing Physical Layer Security," *IEEE Commun. Mag.*, vol. 53, no. 6, pp. 16–20, 2015.

[78] A. Omri and M. O. Hasna, "Physical Layer Security Analysis of UAV Based Communication Networks," in *Proc. IEEE 88th Veh. Technol. Conf. (VTC-Fall)*, Aug. 2018, pp. 1–6.

[79] S. J. Maeng, Y. Yapıcı, I. Guvenç, H. Dai, and A. Bhuyan, "Precoder Design for mmWave UAV Communications with Physical Layer Security," in *Proc. IEEE 21st Signal Process. Adv. Wireless Commun. (SPAWC)*, May 2020, pp. 1–5.

[80] S. J. Maeng, Y. Yapıcı, İ. Güvenç, A. Bhuyan, and H. Dai, "Precoder Design for Physical-Layer Security and Authentication in Massive MIMO UAV Communications," *IEEE Trans. Veh. Technol.*, vol. 71, no. 3, pp. 2949–2964, 2022.

[81] Z. Yin, M. Jia, N. Cheng, W. Wang, F. Lyu, Q. Guo, and X. Shen, "UAV-Assisted Physical Layer Security in Multi-Beam Satellite-Enabled Vehicle Communications," *IEEE Trans. Intel. Transp. Syst.*, vol. 23, no. 3, pp. 2739–2751, 2021.

[82] X. Sun, W. Yang, Y. Cai, R. Ma, and L. Tao, "Physical Layer Security in Millimeter Wave SWIPT UAV-Based Relay Networks," *IEEE Access*, vol. 7, pp. 35 851–35 862, 2019.

[83] M. Bloch, J. Barros, M. R. Rodrigues, and S. W. McLaughlin, "Wireless Information-Theoretic Security," *IEEE Trans. Inf. Theory*, vol. 54, no. 6, pp. 2515–2534, 2008.

[84] H. Lei, I. S. Ansari, G. Pan, B. Alomair, and M.-S. Alouini, "Secrecy Capacity Analysis over $\alpha - \mu$ Fading Channels," *IEEE Commun. Lett.*, vol. 21, no. 6, pp. 1445–1448, 2017.

[85] J. H. Winters, J. Salz, and R. D. Gitlin, "The Impact of Antenna Diversity on the Capacity of Wireless Communication Systems," *IEEE Trans. Commun.*, vol. 42, no. 234, pp. 1740–1751, 1994.

[86] G. L. Stüber and G. L. Steuber, *Principles of Mobile Communication*, 1st ed. Springer, 1996.

[87] R. Subadar and A. D. Singh, "Performance of SC Receiver over TWDP Fading Channels," *IEEE Wireless Commun. Lett.*, vol. 2, no. 3, pp. 267–270, 2013.

[88] F. Yilmaz and M.-S. Alouini, "A Unified MGF-Based Capacity Analysis of Diversity Combiners over Generalized Fading Channels," *IEEE Trans. Commun.*, vol. 60, no. 3, pp. 862–875, 2012.

[89] M. Di Renzo, F. Graziosi, and F. Santucci, "Channel Capacity over Generalized Fading Channels: A Novel MGF-Based Approach for Performance Analysis and Design of Wireless Communication Systems," *IEEE Trans. Veh. Technol.*, vol. 59, no. 1, pp. 127–149, 2009.

[90] M. Abramowitz and I. A. Stegun, *Handbook of Mathematical Functions with Formulas, Graphs, and Mathematical Tables*, 1988.

[91] Y. Zhang, J. Zhang, L. Yang, B. Ai, and M.-S. Alouini, "On the Performance of Dual-Hop Systems over Mixed FSO/mmWave Fading Channels," *IEEE Open J. Commun. Soc.*, vol. 1, pp. 477–489, 2020.

[92] H. Al-Hmood and H. S. Al-Raweshidy, "Performance Analysis of mmWave Communications With Selection Combining over Fluctuating-Two Ray Fading Model," *IEEE Commun. Lett.*, vol. 25, no. 8, pp. 2531–2535, 2021.

[93] J. Stewart, D. K. Clegg, and S. Watson, *Calculus: Early Transcendentals*, 9th ed. Cengage Learning, 2020.

[94] V. A. Aalo and J. Zhang, "On the Effect of Cochannel Interference on Average Error Rates in Nakagami-fading Channels," *IEEE Commun. Lett.*, vol. 3, no. 5, pp. 136–138, 1999.

[95] J. H. Winters, "Optimum Combining in Digital Mobile Radio with Cochannel Interference," *IEEE Trans. Veh. Technol.*, vol. 33, no. 3, pp. 144–155, 1984.

[96] A. A. Abu-Dayya and N. C. Beaulieu, "Outage Probabilities of Cellular Mobile Radio Systems with Multiple Nakagami Interferers," *IEEE Trans. Veh. Technol.*, vol. 40, no. 4, pp. 757–768, 1991.

[97] J. A. Anastasov, G. T. Djordjevic, and M. C. Stefanovic, "Analytical Model for Outage Probability of Interference-Limited Systems over Extended Generalized-K Fading Channels," *IEEE Commun. Lett.*, vol. 16, no. 4, pp. 473–475, 2012.

[98] N. Y. Ermolova and O. Tirkkonen, "Outage Probability Analysis in Generalized Fading Channels with Co-Channel Interference and Background Noise: η-μ/η-μ, η-μ/κ-μ, and κ-μ/η-μ Scenarios," *IEEE Trans. Wirel. Commun.*, vol. 13, no. 1, pp. 291–297, 2013.

[99] W. Mei and R. Zhang, "Aerial-Ground Interference Mitigation for Cellular-Connected UAV," *IEEE Wirel. Commun.*, vol. 28, no. 1, pp. 167–173, 2021.

[100] M. Kim and J. Lee, "Outage probability of UAV communications in the presence of interference," in *Proc. IEEE GLOBECOM*. IEEE, 2018, pp. 1–6.

[101] A. A. Khuwaja, G. Zheng, Y. Chen, and W. Feng, "Optimum Deployment of Multiple UAVs for Coverage Area Maximization in the Presence of Co-Channel Interference," *IEEE Access*, vol. 7, pp. 85 203–85 212, 2019.

[102] I. Valiulahi and C. Masouros, "Multi-UAV Deployment for Throughput Maximization in the Presence of Co-Channel Interference," *IEEE Internet Things J.*, vol. 8, no. 5, pp. 3605–3618, 2020.

[103] L. Zhou, X. Chen, M. Hong, S. Jin, and Q. Shi, "Efficient Resource Allocation for Multi-UAV Communication Against Adjacent and Co-Channel Interference," *IEEE Trans. Veh. Technol.*, vol. 70, no. 10, pp. 10 222–10 235, 2021.

[104] J. Curtiss, "On the Distribution of the Quotient of Two Chance Variables," *Ann. Math. Stat.*, vol. 12, no. 4, pp. 409–421, 1941.

[105] H. Ilhan, "Performance Analysis of Two-Way AF Relaying Systems over Cascaded Nakagami-m Fading Channels," *IEEE Signal Process. Lett.*, vol. 19, no. 6, pp. 332–335, 2012.

[106] B. Talha and M. Pätzold, "Channel Models for Mobile-to-Mobile Cooperative Communication Systems: A State of the Art Review," *IEEE Veh. Technol. Mag.*, vol. 6, no. 2, pp. 33–43, 2011.

[107] Q. Sun, Z. Zhang, Y. Zhang, M. Lopez-Benitez, and J. Zhang, "Performance Analysis of Dual-Hop Wireless Systems over Mixed FSO/RF Fading Channel," *IEEE Access*, vol. 9, pp. 85 529–85 542, 2021.

[108] A. Bekkali, S. Zou, A. Kadri, M. Crisp, and R. V. Penty, "Performance Analysis of Passive UHF RFID Systems Under Cascaded Fading Channels and Interference Effects," *IEEE Trans. Wirel. Commun.*, vol. 14, no. 3, pp. 1421–1433, 2014.

[109] H. Chergui, M. Benjillali, and S. Saoudi, "Performance Analysis of Project-and-Forward Relaying in Mixed MIMO-Pinhole and Rayleigh Dual-Hop Channel," *IEEE Commun. Lett.*, vol. 20, no. 3, pp. 610–613, 2016.

[110] M. Abualhayja'a, A. Centeno, L. Mohjazi, M. M. Butt, P. Sehier, and M. A. Imran, "Exploiting Multi-Hop RIS-Assisted UAV Communications: Performance Analysis," *IEEE Commun. Lett.*, 2023.

[111] Y. Chen, N. Zhao, Z. Ding, and M.-S. Alouini, "Multiple UAVs as Relays: Multi-Hop Single Link Versus Multiple Dual-Hop Links," *IEEE Trans. Wirel. Commun.*, vol. 17, no. 9, pp. 6348–6359, 2018.

[112] J. Fan, M. Cui, G. Zhang, and Y. Chen, "Throughput Improvement for Multi-Hop UAV Relaying," *IEEE Access*, vol. 7, pp. 147 732–147 742, 2019.

[113] T. Kim and D. Qiao, "Energy-Efficient Data Collection for IoT Networks via Cooperative Multi-Hop UAV Networks," *IEEE Trans. Veh. Technol.*, vol. 69, no. 11, pp. 13 796–13 811, 2020.

[114] S. Gong, S. Wang, C. Xing, S. Ma, and T. Q. Quek, "Robust Superimposed Training Optimization for UAV Assisted Communication Systems," *IEEE Trans. Wireless Commun.*, vol. 19, no. 3, pp. 1704–1721, 2019.

[115] U. Challita and W. Saad, "Network Formation in the Sky: Unmanned Aerial Vehicles for Multi-Hop Wireless Backhauling," in *Proc. IEEE GLOBECOM*. IEEE, 2017, pp. 1–6.

[116] C. D. Bodenschatz, *Finding an H-Function Distribution for the Sum of Independent H-Function Variates.* The University of Texas at Austin, 1992.

[117] B. Shang, V. Marojevic, Y. Yi, A. S. Abdalla, and L. Liu, "Spectrum Sharing for UAV Communications: Spatial Spectrum Sensing and Open Issues," *IEEE Veh. Technol. Mag.*, vol. 15, no. 2, pp. 104–112, 2020.

[118] R. Umar, A. U. Sheikh, and M. Deriche, "Unveiling the Hidden Assumptions of Energy Detector Based Spectrum Sensing for Cognitive Radios," *IEEE Commun Surv Tutor*, vol. 16, no. 2, pp. 713–728, 2013.

[119] S. Haykin, D. J. Thomson, and J. H. Reed, "Spectrum Sensing for Cognitive Radio," *Proc. IEEE*, vol. 97, no. 5, pp. 849–877, 2009.

[120] F. F. Digham, M.-S. Alouini, and M. K. Simon, "On the Energy Detection of Unknown Signals over Fading Channels," *IEEE Trans. Commun.*, vol. 55, no. 1, pp. 21–24, 2007.

[121] P. C. Sofotasios, E. Rebeiz, L. Zhang, T. A. Tsiftsis, D. Cabric, and S. Freear, "Energy Detection Based Spectrum Sensing over $\kappa - \mu$ and $\kappa - \mu$ Extreme Fading Channels," *IEEE Trans. Veh. Technol.*, vol. 62, no. 3, pp. 1031–1040, 2012.

[122] E. Chatziantoniou, B. Allen, V. Velisavljevic, P. Karadimas, and J. Coon, "Energy Detection Based Spectrum Sensing over Two-Wave With Diffuse Power Fading Channels," *IEEE Trans. Veh. Technol.*, vol. 66, no. 1, pp. 868–874, 2016.

[123] S. K. Yoo, S. L. Cotton, P. C. Sofotasios, S. Muhaidat, O. S. Badarneh, and G. K. Karagiannidis, "Energy Detection-Based Spectrum Sensing over Fisher-Snedecor $\mathcal{F}$ Fading Channels," in *Proc. IEEE GLOBECOM.* IEEE, 2018, pp. 1–6.

[124] F. F. Digham, M.-S. Alouini, and M. K. Simon, "On the Energy Detection of Unknown Signals over Fading Channels," in *Proc. IEEE Int. Conf. Commun.(ICC).* IEEE, 2003, pp. 3575–3579.

[125] P. Cantrell and A. Ojha, "Comparison of Generalized Q-function Algorithms," *IEEE Trans. Inf. Theory*, vol. 33, no. 4, pp. 591–596, 1987.

[126] V. M. Kapinas, S. K. Mihos, and G. K. Karagiannidis, "On the Monotonicity of the Generalized Marcum and Nuttall Q-Functions," *IEEE Trans. Inf. Theory*, vol. 55, no. 8, pp. 3701–3710, 2009.

[127] A. Ghasemi and E. S. Sousa, "Impact of User Collaboration on the Performance of Sensing-Based Opportunistic Spectrum Access," in *Proc. IEEE Veh. Technol. Conf.* IEEE, 2006, pp. 1–6.

[128] M. A. Hossain, R. M. Noor, K.-L. A. Yau, I. Ahmedy, and S. S. Anjum, "A Survey on Simultaneous Wireless Information and Power Transfer With Cooperative Relay and Future Challenges," *IEEE Access*, vol. 7, pp. 19 166–19 198, 2019.

[129] F. Ono, H. Ochiai, and R. Miura, "A Wireless Relay Network Based on Unmanned Aircraft System with Rate Optimization," *IEEE Trans. Wirel. Commun.*, vol. 15, no. 11, pp. 7699–7708, 2016.

[130] P. S. Bithas, G. A. Ropokis, G. K. Karagiannidis, and H. E. Nistazakis, "UAV-Assisted Communications With RIS: A Shadowing-Based Stochastic Analysis," *IEEE Trans. Veh. Technol.*, 2024.

[131] V. Adamchik and O. Marichev, "The Algorithm for Calculating Integrals of Hypergeometric Type Functions and Its Realization in REDUCE System," in *Proc. Int. Symp. Symb. Algebr. Comput. ISSAC*, July 1990, pp. 212–224.

[132] E. Fichard and V. Franco, "Differential Properties of Meijer's G-Function," *J. Phys. A: Mathematical and General*, vol. 13, no. 7, p. 2331, 1980.

[133] A. M. Mathai and R. K. Saxena, *Generalized Hypergeometric Functions with Applications in Statistics and Physical Sciences*, 1st ed. Springer, 1973.

[134] A. Soulimani, M. Benjillali, H. Chergui, and D. B. da Costa, "Multihop Weibull-Fading Communications: Performance Analysis Framework and Applications," *J. Frankl. Inst.*, vol. 358, no. 15, pp. 8012–8044, 2021.

[135] I. S. Ansari, F. Yilmaz, and M.-S. Alouini, "Performance Analysis of FSO Links over Unified Gamma-Gamma Turbulence Channels," in *Proc. IEEE 81st Veh. Technol. Conf. (VTC Spring)*. IEEE, 2015, pp. 1–5.

[136] G. K. Karagiannidis, T. A. Tsiftsis, and R. K. Mallik, "Bounds for Multihop Relayed Communications in Nakagami-m Fading," *IEEE Trans. Commun.*, vol. 54, no. 1, pp. 18–22, 2006.

[137] N. Temme, "A Set of Algorithms for the Incomplete Gamma Functions," *Probab. Eng. Inf. Sci.*, vol. 8, no. 2, pp. 291–307, 1994.